Investigations on the Transport of High-Intensity Beams Using Particle-in-Cell Simulations

Dissertation
zur Erlangung des Doktorgrades
der Naturwissenschaften

vorgelegt beim Fachbereich Physik
der Johann Wolfgang Goethe-Universität
in Frankfurt am Main

von
Daniel Noll
aus Gießen

Frankfurt am Main 2016
(D 30)

vom Fachbereich Physik der
Johann Wolfgang Goethe-Universität als Dissertation angenommen.

Dekan:
Prof. Dr. R. Reifarth

Gutachter:
Prof. Dr. U. Ratzinger
Prof. Dr. J. Maruhn

Datum der Disputation: 22.11.2016

Zusammenfassung

Raumladungseffekte spielen in der Niederenergiestrahltransportsektion von Beschleunigern für intensive Ionenstrahlen eine wichtige Rolle. Diese bedingen nicht nur den Einsatz von Fokussierlinsen mit höherer Brechkraft, sondern können für nicht-homogene Strahlverteilungen zu einem Anwachsen der Emittanz [7] führen. In magnetostatischen Systemen stellt sich jedoch durch die Ansammlung von Elektronen, welche zum Beispiel durch Restgasionisation bereitgestellt werden, im Strahlpotential eine Kompensation, also eine Reduktion der Raumladungskräfte ein. Ist die Verteilung der Elektronen nicht gleich jener der Strahlteilchen, der Strahl also lokal unterschiedlich kompensiert, so kann auch hierdurch eine Erhöhung der Emittanz entstehen [46].

Eine Messung der Verteilung der Kompensationselektronen sowie deren Geschwindigkeiten wie beispielsweise in [45] stellte sich in der Vergangenheit als schwierig heraus. In theoretischen Ansätzen, wie zum Beispiel in [8] müssen weitreichende vereinfachende Annahmen über die Geometrie der Transportlinie und die involvierten Prozesse vorgenommen werden, um ein lösbares System zu erhalten. Als alternativer Ansatz wurde in dieser Arbeit eine Untersuchung der Raumladungskompensation über eine Berücksichtigung der Sekundärpartikel in Particle-in-Cell-Simulationen (PIC) verfolgt. Wie im dritten Kapitel dieser Arbeit vorgestellt, stellt das elektrostatische PIC-Verfahren eine Lösungsmethode des Systems aus Vlasov- und Poisson-Gleichung durch die Einführung von Makroteilchen, Teilchen endlicher Ausdehnung, dar.

Für die Untersuchungen wurde ein neuer PIC-Code *bender* entwickelt. Die verwendeten Algorithmen sowie deren Implementierung wurden im dritten Kapitel vorgestellt. Für die Integration der Bewegung der Makroteilchen wird der Velocity-Verlet-Algorithmus verwendet. Im Vergleich zu Standardintegrationsverfahren für Differentialgleichungen wie dem Runge-Kutta-Verfahren, hat dieser den Vorteil, dass er Energie und Drehimpuls über lange Simulationszeiten innerhalb gewisser Grenzen erhält. Dies wurde anhand einiger Beispielsysteme demonstriert.

Zur Berechnung des elektrischen Eigenfeldes der Teilchenensembles kann die Poisson-Gleichung numerisch gelöst werden. Für eine Lösung in drei Dimensionen wurden zwei unterschiedliche Verfahren implementiert. Die Berechnung der Potentiale mittels schneller Fouriertransformationen (FFT) profitiert von der Verfügbarkeit schneller Implementierungen der FFT, wie der verwendeten FFTW-Bibliothek [32], ist aber auf äquidistante Gitter und boxförmige Randbedingungen begrenzt. Im zweiten Solver, werden Methoden für dünnbesetzte Matrizen – hierfür kommt die Bibliothek PetSc [29] zum Einsatz – verwendet, um das Gleichungssystem resultierend aus einer Finite-Differenzen-Diskretisierung der Poissongleichung zu lösen. Der Code erlaubt hierbei das Setzen der Potentiale auf Objekten beliebiger Geometrie. Mittels der selben Technik wurde auch ein Solver für die Poissongleichung in zylindrischer Geometrie umgesetzt. Alle drei Poissonsolver erlauben

eine Aufteilung des Gitters auf mehrere Prozesse, entweder durch longitudinales Zerlegen des Gitters oder durch eine Aufteilung auf beliebig dimensionierte und frei angeordnete Gitterboxen. Die drei Solver wurden durch den Vergleich des berechneten elektrischen Feldes einer radial-gaussverteilten Ladungswolke mit der analytischen Lösung getestet.

Nach dem Test der Einzelkomponenten des Codes, wurden zwei bekannte selbstkonsistente Lösungen der Vlasov-Gleichung beschrieben und deren Vorhersagen mit Simulationsergebnissen verglichen. Als Vergleichssystem für Strahltransportrechnungen kam ein angepasster KV-Strahl in einem periodischen Quadrupolkanal mit einem Phasenvorschub von 15° (Nullstromphasenvorschub 60°) zum Einsatz. Es konnte gezeigt werden, dass die *bender*-Ergebnisse für den Phasenvorschub mit höherer Teilchenanzahl und Gitterauflösung gegen den theoretischen Wert konvergieren. Mit der höchsten mit vertretbarem Aufwand rechenbaren Auflösung ergab sich ein nur noch geringer Unterschied im Phasenvorschub von 0,06°.

Als zweiter Test kam eine der Boltzmann-Statistik folgende Elektronenwolke in einem externen Potential zum Einsatz. Zu diesem Zwecke wurde ein Algorithmus zur Lösung der Poisson-Boltzmann-Gleichung

$$\nabla^2 \varphi_\mathrm{c}(r) = -\frac{\rho_\mathrm{c}}{\epsilon_0} \exp\left(-\frac{q\left(\varphi_\mathrm{c}(r) + \varphi_\mathrm{ext}(r)\right)}{k_\mathrm{b} T}\right) \tag{1}$$

entwickelt. Hierfür wird die Gleichung durch Skalierung der Koordinaten mit der Debye-Länge und des Potentials durch die Temperatur normiert und Gleichung (1) mit einer Abhängigkeit von einem neuen Parameter versehen. Die resultierende Differentialgleichung lässt sich mittels einer Kombination aus Crank-Nicholson- und Euler-Verfahren lösen. Für eine gaussförmige externe Ladungsverteilung wurde die Elektronendichte berechnet und eine daraus generierte Verteilung in *bender* geladen. Für hohe Teilchenanzahlen bleibt diese über lange Simulationszeiträume stabil. Es wurde jedoch ein zeitlich konstanter Anstieg der Gesamtenergie des Systems beobachtet. Dieser konnte als der bereits bekannte Effekt der stochastischen Heizung in PIC-Simulationen [21, p. 316] identifiziert werden.

Neben *bender* wurde ein zweiter, einfacherer Code *tralitrala* entwickelt. Dieser erlaubt unter dem Einsatz von Strahltransportmatrizen und auf die Feldgeometrie spezialisierten Integrationsalgorithmen – implementiert sind Solenoide sowie externe Potentialverteilungen – eine schnelle Simulation von Niederenergiestrahlführungslinien unter Berücksichtigung der Raumladung in einer (radial) oder zwei (kartesisch, transversal) Dimensionen. Dieser ist sowohl auf gewöhnlichen CPUs als auch auf Graphikkarten des Herstellers NVidia lauffähig, wobei die Graphikkartenversion für hohe Teilchenanzahlen bis zu einem Faktor von 100 schneller als die CPU-Variante ist.

Zur Simulation des Kompensationsprozesses wird die Ionisation des Restgases sowohl durch Protonen als auch durch Elektronen berücksichtigt. Ionisierende Teilchenstöße wurden mittels der Nullkollisionsmethode in *bender* implementiert. Die benötigten Wirkungsquerschnitte werden über zwei atomphysikalische Modelle berechnet: dem semiempirischen Model von Rudd et al. [48] für Protonenstoßionisation und dem Model von Kim et al. für Elektronenstoßionisation [52]. Beide Modelle liefern einfach-differentielle Wirkungsquerschnitte. Die Simulation reproduziert also auch die Sekundärelektronenenergie.

Die verbleibenden, unbestimmten Komponenten wie beispielsweise der Ejektionswinkel und die Energie des verbleibenden Restgasions werden mittels Energie- und Impulserhaltung unter vereinfachenden Annahmen berechnet. Der Einfluss der Produktion von Sekundärelektronen bei Teilchenverlusten an außerhalb des Strahles befindlichen Metalloberflächen, wie dem Strahlrohr, auf den Kompensationsgrad wurde abgeschätzt. Dieser ist vernachlässigbar, sofern nicht bereits eine Kompensation aus anderen Quellen besteht.

Der Einfluss der Kompensation auf die Drift eines 120 keV, 100 mA-Strahls wurde mittels *bender* untersucht. Das simulierte System besitzt eine Länge von 0,5 m und wurde um den longitudinalen Einschluss der Elektronen zu gewährleisten mit zwei Repellerelektroden auf einem Potential von −1,5 keV abgeschlossen. Als Restgas wurde ein homogener Argon-Hintergrund bei 1×10^{-5} mbar angenommen. Der Aufbau der Kompensation zeigt das erwartete Verhalten: ein linearer Anstieg der Elektronenanzahl mit der theoretischen Produktionsrate, gefolgt von ansteigenden Elektronenverlusten bis sich ein Gleichgewicht einstellt, in dem diese der Produktionsrate entsprechen.

Bei den gewählten Parametern wird, außerhalb des Einflusses der Repellerelektroden, ein Kompensationsgrad η_{part} von durchschnittlich 80 % erreicht. In den berechneten Ladungsdichteverteilungen wurden einige Merkmale identifiziert, die sich nicht durch eine gleichmäßige Reduktion des elektrischen Feldes erklären lassen. Diese sind die Formierung eines Hohlstrahles im Strahlfokus, die Bildung eines Bereiches negativer Ladungsdichte jenseits des Strahlrandes, sowie die Akkumulation von Restgasionen im Bereich des Fokus. Die ersten beiden Effekte lassen sich in der Nettoladungsdichte, dargestellt in Abbildung 1a, erkennen. Weiterhin entsprechen die Verteilungen der Geschwindigkeiten der Elektronen an jeder Stelle in der Simulation einer Gaussverteilung. Die Breite (“Temperatur”) dieser Verteilungen unterscheidet sich jedoch zwischen den transversalen und der longitudinalen Ebene. Beide ändern ihren Wert longitudinal.

Setzt man die Präsenz jener Gaussverteilungen voraus, so erlaubt Gleichung (1) eine Bestimmung des Potentials des kompensierten Strahles. Dies wurde beispielhaft für die Drift eines 2 cm breiten Parallelstrahles mit 120 keV und 50 mA Strom über 50 cm untersucht. Für niedrige Elektronentemperaturen kompensieren diese den Strahl vollständig, für Kompensationsgrade unter 100 % aber nur bis zu einem gewissen Radius. Die Nettoladungsdichte entspricht der eines Hohlstrahles, bei dem das elektrische Feld am Rand quadratisch ansteigt. Bei größeren Temperaturen fällt die Elektronendichte radial früher ab und reicht zunehmend über den Strahlrand hinaus, was das Verhalten der PIC-Simulation reproduziert. Bei hohen Elektronentemperaturen wird deren Dichte zunehmend homogen, erreicht also auch auf der Strahlachse nicht mehr die Dichte des Strahles.

Um die Evolution der Verteilung unter dem Einfluss der Elektronen zu untersuchen, wurde der Raumladungssolver in *tralitrala* durch den Poisson-Boltzmann-Solver ersetzt. Für eine homogene Strahlverteilung ergab sich das größte Emittanzwachstum für $T \to 0$ bei Kompensationsgraden um 35 % aufgrund des Einflusses des radial quadratisch ansteigenden elektrischen Feldes am Strahlrand. Bei höheren Temperaturen oder unterschiedlichen Kompensationsgraden ergab sich ein Emittanzwachstum unter 5 %. Dieses verschwindet jedoch nur für $T = 0$, $\eta_{\text{part}} = 100\,\%$ und $\eta_{\text{part}} = 0\,\%$ (keine Kompensation). Für einen rms-äquivalenten, im Phasenraum Gauss'sch verteilten Strahl ergab sich das größte Wachstum

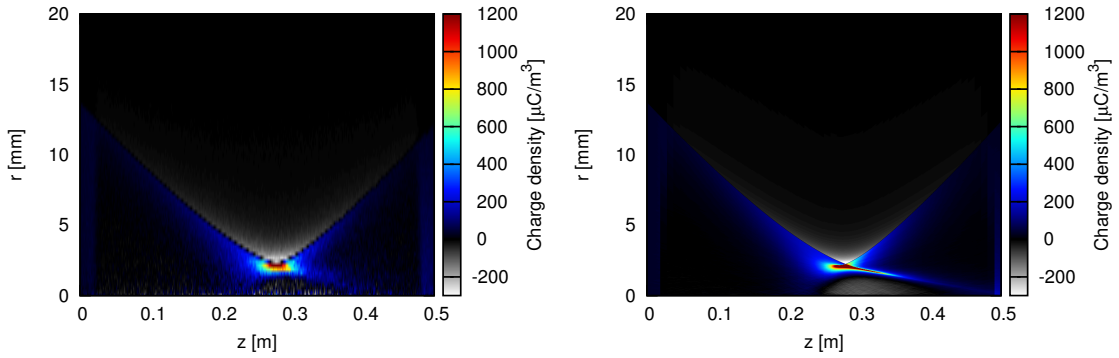

(a) PIC-Simulation mit *bender*.

(b) Berechnung aus der Poisson-Boltzmann-Gleichung.

Abbildung 1.: Netto-Ladungsdichte in einer Strahldrift berechnet mittels PIC-Simulation unter Einbeziehung der Sekundärelektronen und -ionen in (a) und über eine Lösung der Poisson-Boltzmann-Gleichung in (b). Zu erkennen ist die Präsenz einer negativen Ladungsträgerdichte jenseits des Strahlrandes, sowie die Formierung eines Hohlstrahles, der lokal nicht vollständig kompensiert ist. Dies sind beides Effekte, die bei einer Berechnung der Kompensation durch Skalierung der Felder nicht auftreten.

(25 %) in vollständiger Abwesenheit kompensierender Elektronen aufgrund des nichtlinearen Eigenfeldes des Strahles. Hier genügt bereits ein geringer Kompensationsgrad um das Wachstum auf unter 10 % zu senken.

Übernimmt man die transversale Temperaturverteilung $T(z)$ und die Kompensationsgradverteilung $\eta_{\mathrm{part}}(z)$ und führt eine ähnliche Simulation unter Verwendung der Poisson-Boltzmann-Gleichung für das mit *bender* simulierte System aus, so erhält man vergleichbare Ergebnisse. Ein Vergleich ist in Abbildung 1 dargestellt. Der Hohlstrahl entsteht aufgrund der Reduktion der Teilchenwinkel durch das am Strahlrand stark ansteigende elektrische Feld. Durch das Hohlprofil des Strahles in der Gegend des Fokus übersteigt die Elektronendichte an der Achse die Protonendichte. Dies führt in der *bender*-Simulation zum beobachteten Einschluss der Restgasionen.

Die Elektronen verhalten sich somit wie ein im Strahlpotential eingeschlossenes Nicht-Neutrales Plasma. Dadurch wird es wichtig, den Ursprung der gefundenen Geschwindigkeitsverteilung zu verstehen. Es wurde festgestellt, dass die Temperaturen, sowie auch der in der Simulation erreichte Kompensationsgrad, empfindlich von der Anzahl der Makroteilchen abhängt. Je geringer die Masse und Ladung pro Makroteilchen, desto geringer die sich ergebenden Temperaturen und desto höher der Grad der Kompensation. Es kann davon ausgegangen werden, dass Letzteres ein Effekt der geringeren Temperaturen ist, da der gleiche Zusammenhang auch bei der Variation des Restgasdruckes, und somit der Elektronenproduktionsrate, gefunden wurde.

Ein möglicher Erklärungsansatz für das Enstehen der Abhängigkeit zwischen der Temperatur und dem numerischen Teilchen-pro-Makroteilchen-Verhältnis könnte das zuvor in

den Code-Tests gefundene stochastische Heizen sein. Es wurde die Hypothese geformt, dass die zugeführte Energie über erhöhte Teilchenverluste vom System ausgeglichen wird. Dies wurde mittels einiger numerischer Experiment untersucht. Wird zum Beispiel das elektrische Feld des Strahles zeitlich konstant gehalten und somit eine der Quellen für Fluktuationen ausgeschaltet, sinkt die Temperatur auf weniger als die Hälfte. Bevor physikalisch vorhandene Heizprozesse, wie beispielsweise Coulomb-Kollisionen der Strahlteilchen mit dem Kompensationsplasma, in die Simulation übernommen werden können, muss sichergestellt sein, dass diese nicht durch numerische Heizeffekte überdeckt werden. Dies könnte geschehen, in dem die Prozesse berücksichtigt werden und die erhaltenen Unterschiede verglichen werden oder in dem der Ursprung des stochastischen Heizens genauer untersucht wird. Da die Ergebnisse für die Heizraten im abgeschlossenen Testsystem nicht ohne weiteres auf das kompensierte System mit Strahl übertragen werden können, ist hier keine abschließende Antwort möglich.

Die präsentierten Simulationen stellen einen Startpunkt für die Untersuchung weiterer geladener Vielteilchensysteme dar. Das in der Simulation erreichte Gleichgewicht ist von den vorhandenen Teilchenproduktions- und Verlustmechanismen geprägt, wobei letztere stark durch Heiz- sowie potentiell vorhandene Kühlungsprozesse beeinflusst werden. Von ähnlichen Vorgängen dominiert sind Gabor-Linsen [13], in denen eine Elektronenwolke in einer Falle aus magnetischen und elektrischen Feldern gehalten wird und welche für die Fokussierung von Ionenstrahlen zum Einsatz kommen können. Um in Zukunft bessere Vorhersagen über das sich einstellende Gleichgewicht in solchen Systemen machen zu können, ist es wichtig, die beteiligten Prozesse sowohl experimentell als auch in Simulationen genauer zu studieren und deren Zusammenspiel zu verstehen.

Neben grundsätzlichen Untersuchungen können Particle-in-Cell-Simulationen ebenso einen Beitrag zur Auslegung von Beschleunigerkomponenten liefern. In Kapitel 5 werden zwei solche Anwendungen von *bender* beschrieben.

In [11] wurde der Code verwendet, um die Strahlpulsformierung innerhalb eines neuartigen E × B-Choppersystems zu untersuchen, welches im Rahmen des FRANZ-Projektes zum ersten Mal zum Einsatz kommen wird. Hierfür wurde in [81] mittels *tralitrala* und anderen Programmen der Strahltransport der Niederenergiesektion ausgiebig untersucht und eine optimale Solenoideinstellungen ermittelt. Eine diesen Einstellungen entsprechende Strahlverteilung wurde in *bender* geladen und unter den zeitabhängigen elektrischen und statischen magnetischen Feldern transportiert. Damit konnte in [11] gezeigt werden, dass das System selbst unter der Wirkung der vollen Raumladungskräfte den Anforderungen an die Pulslänge und an die Strahlqualität entspricht.

Für eine Elektronenlinse für den Integrable Optics Test Accelerator (IOTA) im Rahmen des Fermilab Accelerator Science and Technology-Projektes (FAST) am Fermi National Accelerator Laboratory wurden ebenfalls Simulationen angefertigt. Als erster Schritt wurde hierfür eine Magnetfeld- und Spulenkonfiguration entworfen, die in der Lage ist, einen 5 keV-Elektronenstrahl von der Kathode auf die Achse des IOTA-Ringes zu führen. Durch Imperfektionen in der Feldgeometrie entstehende Aberrationen wurden untersucht und charakterisiert. Der Einfluss der Krümmungsdrift auf die Teilchenbewegung wurde untersucht und die Simulationsergebnisse mit semianalytischen Abschätzungen verglichen.

Die Grenzen des Strahltransportes in longitudinalen magnetischen Führungsfeldern

wurden analysiert. Das stärkste identifizierte Limit entsteht als Resultat des durch die Kompression vorhandenen longitudinalen elektrischen Eigenfeldes des Strahles, welches diesen abbremst oder gar reflektiert. Hierfür konnte unter Annahme eines stabilen Profils eine Formel für die Stromgrenze

$$I < 4\pi\epsilon_0\sqrt{\frac{2e}{m}}U^{3/2}\left(\frac{g_1 - \sqrt{3g_2^2 - g_1^2/3}}{4g_1^2 - 9g_2^2}\right)$$

gefunden und mit *bender*-Simulationen verifiziert werden. Außer der Strahlenergie hat auch die Strahlverteilung sowie die Strahlrohrgeometrie, enthalten in den Faktoren g_1 und g_2 am Start und Ende des Systems, einen starken Einfluss.

Die Teilchenbewegung unter der eigenen Raumladung ist gegeben durch eine langsame Drehung um die Strahlachse überlagert von schnellen radialen Oszillationen. Für homogen verteilte Strahlen verblieb das Profil in zwei-dimensionalen Simulationen unter dieser Bewegung stabil. In Strahlen, die einer McMillan-Verteilung folgen, welche für die Experimente an IOTA von Interesse ist, wurde jedoch das Enstehen von Ringen erhöhter Dichte bereits nach weniger als 1 m Transport beobachtet. Diese zeigen sich auch in Simulation der vollständigen IOTA-Elektronenlinse in der Form von Spiralen in der finalen Strahlverteilung. Da die Stabilität des Profils und insbesondere der Kicks auf den zirkulierenden Strahl von großer Bedeutung für die Anwendung der Linse ist, werden hier weitere Untersuchungen benötigt.

Contents

1. Introduction

With the advent of modern computers in the 60s of the last century, it became possible to investigate the dynamics of systems of many charged particles—such as plasmas and beams—by means of computer experiments. For this purpose, a model including the fundamental interactions required for the system of interest is built and then advanced in time. This makes it possible to investigate strongly non-linear and complex phenomena not treatable by theory. Compared to performing measurements on the system itself, computer experiments are usually much easier to set up in a controlled way and allow extracting as much information as required without disturbing the system.

For plasma simulation, these models started as the integration of the motion of one-dimensional charge sheets moving under the influence of the others, for example in [1]. A few years later, the first particle-in-cell models were introduced [2], which use a grid to calculate the electric fields. In the following decades, the method was applied to problems in two and later three dimensions, some including electrodynamic effects, realistic boundaries and collisions among the particles themselves or with neutral gases.

Particle-in-cell models are used extensively for the study of hadron particle accelerators to investigate the evolution of beams under the influence of the optics and their own electric and, if non-negligible, magnetic field. The self-fields become increasingly important when high beam intensities are involved. Since the rates of the reaction under investigation with these machines are directly proportional to the number of particles, the requirements on the beam current are continuously increasing. For example, this is the case for neutron sources of various types such as ESS [3], SNS [4] or FRANZ [5] and for high-energy colliders for elementary particle physics such as the LHC with its injectors [6]. Depending on the application, the design objectives are usually a low increase in the beam quality (emittance) as well as keeping particle losses along the accelerator low to avoid activation.

For this purpose, it is important to accurately model and to understand every part of the accelerator. Since the beam's electric field decreases with increasing energy, space charge forces are critical in the low-energy beam transport (LEBT) section of such a machine. They act as an additional continuous defocusing force on the beam, necessitating stronger lenses with larger fields. Additionally, space charge forces drive non-homogeneous beam distributions towards homogeneous ones. This reduces the energy contained within the electric field, which is converted into an unwanted increase of the beam's emittance [7].

The influence of space charge can be reduced when particles of opposite charge are allowed to accumulate within the potential of the beam. This is usually the case when no large external electric fields are present. The compensation particles are typically formed by ionization of the residual gas background. Measurements indicate that a full neutralization of the beam charge is not achieved in most cases. Furthermore, if the distribution of the compensating particles differs from the distribution of the beam, some

electric force will remain and can lead to an increase of the emittance.

Linear models of the compensation only predict the effects resulting from a reduction in space charge force but do not contain any effects from the secondary particle distribution(s). The degree of compensation is a free parameter that has to be chosen from experience. An improved model thus needs to treat both the beam and the additionally involved particle species self-consistently, as their distribution is interdependent. New ions and electrons are continuously formed within the system. In steady-state, there will be no net flow of charge but possibly a flow of energy, which in some way has to be provided by the beam. Various technical factors such as non-dc beams, fluctuating beam currents, influence from measurement devices and complicated field geometries make the description more difficult.

Analytic models like the model by Holmes [8] often need to make assumptions about the given geometry such as assuming a fixed beam distribution and require various approximations to be solvable.

In this work, an ab initio approach to modeling the compensation process by including the relevant particle species and production processes into a newly developed particle-in-cell code *bender* was chosen. Similar approaches were already taken in [9] or [10].

Along with some single-particle effects, **Chapter 2** introduces the Vlasov equation as the governing kinetic equation for particle beams as well as the KV envelope equations which result in a self-consistent solution for homogeneous particle beams. **Chapter 3** starts with a motivation of the particle-in-cell method as a solution to the Vlasov-Poisson system of equations. Then, the algorithms used for *bender* are discussed along with tests to verify their implementation. The chapter concludes with two tests of the full code against known solutions.

Chapter 4 covers the studies on the space charge compensation of a low-energy proton beam. The chapter starts with a short introduction on techniques used for the measurement of compensation in ion beams as well as some general definitions. For the simulations, a model for the ionization of the residual gas is required, which is presented subsequently. Section 4.3 then presents the results for a simple model system, which is compared to results from a theoretical model in Section 4.4.

While the presence of some level of compensation is assumed to be present in the design of most low-energy beam transport sections, space charge compensation in circular accelerators is a new topic. This is the subject of one of the experiments planned for the Integrable Optics Test Accelerator at the Fermi National Accelerator Laboratory. For this purpose, an electron beam guided using magnetic fields and overlapping the circulating beam is considered [10]. While not covering the compensation, **Section 5.1** presents the design of the electron lens as well as studies on the beam dynamics of the electron beam in such a device.

bender was used for the development of a novel chopper system for the FRANZ project in [11]. **Section 5.2** provides a short recapitulation on the performed simulations.

2. Aspects of single and multi-particle motion

2.1. Particle drifts

Particles in a homogeneous magnetic field B with a transverse velocity component $v_\perp$ perform a rotation with the cyclotron frequency ω_c and the gyroradius r_g,

$$\omega_\mathrm{c} = \frac{|qB|}{m} \quad \text{and} \quad r_\mathrm{g} = v_\perp/\omega_\mathrm{c} = \left|\frac{mv_\perp}{qB}\right|.$$

When an additional electric field is present, the magnetic field is inhomogeneous or the fields time-dependent, the motion deviates from the simple oscillation. However, if the changes in the fields are small during the gyration and the changes in time occur much slower than ω_c^{-1}, the motion can be approximated by a drift of a guiding center around which the oscillation occurs. In fields constant in time, [12, p. 139ff] derives an equation of motion for the guiding center,

$$\frac{\mathrm{d}\mathbf{r}}{\mathrm{d}t} = v_\parallel \mathbf{b} + \mathbf{V}_E + \mathbf{V}_{\nabla B} + \mathbf{V}_\kappa. \tag{2.1}$$

$\mathbf{b} = \mathbf{B}/|\mathbf{B}|$ is the (local) direction of the magnetic field and $v_\perp$ and $v_\parallel$ the particle velocity perpendicular and parallel to that vector.

The various components in (2.1) are the different occurring drifts. These are:

- The $E \times B$ drift $\mathbf{V}_\mathrm{E} = \frac{\mathbf{E}_\perp \times \mathbf{B}}{B^2}$, which is a result of the different transverse velocities during the cyclotron oscillation. Depending on the particle charge, the gyroradius is larger towards higher or lower potential respectively and smaller on the opposite side. During a cyclotron oscillation, particles end up with a displacement in direction perpendicular to both $\mathbf{E}$ and $\mathbf{B}$. The effect is not dependent on particle charge and mass.

- The *gradient* B drift $\mathbf{V}_{\nabla B} = \frac{q}{|q|}\frac{v_\perp^2}{2\omega_c}\frac{\mathbf{B}\times\nabla B}{B^2}$ is the result from a difference in gyroradii across a field gradient.

- The *curvature* B drift $\mathbf{V}_\kappa = \frac{q}{|q|}\frac{v_\parallel^2}{\omega_c}\frac{\mathbf{R}_\mathrm{c}\times\mathbf{B}}{R_\mathrm{c}^2 B}$ occurs when the magnetic field lines are not straight. The drift velocity is proportional to the inverse of the local radius of field line curvature R^{-1} and B^{-1}, i.e. the drift is smaller for larger field strengths and larger curvature radii (less curved fields).

When the current density is negligible and the electric field is constant in time, the curvature and the gradient B drift can be combined,

$$\mathbf{V}_{\nabla B} + \mathbf{V}_{\kappa} = \frac{q}{|q|}\frac{1}{\omega_\mathrm{c}}\left(v_\parallel^2 + \frac{1}{2}v_\perp^2\right)\frac{\mathbf{B}\times\nabla B}{B^2}.$$

2.2. Charged particle motion in a radial electric and longitudinal magnetic field

A radial electric field crossed with a longitudinal magnetic field is a commonly occurring field configuration in accelerator physics. One example are electron lenses (Section 5.1), where a high current electron beam producing the electric field is confined by a longitudinal magnetic field. A similar situation occurs in Gabor lenses [13], where the radial electric field is produced by an electron cloud confined by a magnetic and an additional (mainly) longitudinal electric field.

For a homogeneous beam with current I and radius R_b or a homogeneously charged cylinder, the radial electric field is

$$E_\mathrm{r}(r) = \frac{1}{2\pi\epsilon_0}\frac{|I|}{v}\frac{q}{|q|}\frac{r}{R_\mathrm{b}^2} = \frac{m\omega_\mathrm{p}^2}{2q}r, \tag{2.2}$$

where $\omega_\mathrm{p}^2 = nq^2/(m\epsilon_0)$ is the square of the plasma frequency, containing the density n of the beam or electron column. In a longitudinal magnetic field $\mathbf{B} = B\mathbf{e}_\mathrm{z}$, the force balance for a test particle rotating around the axis with an angular velocity $\omega_\mathrm{r} r$ is

$$F_\mathrm{centrifugal} = -m\omega_\mathrm{r}^2 r = \frac{1}{2}m\omega_\mathrm{p}^2 r + q\omega_\mathrm{r} B r = F_\mathrm{electric} + F_\mathrm{magnetic}, \tag{2.3}$$

with first and second term, the centrifugal and the electric force, always acting defocusing. Introducing the cyclotron frequency $\omega_\mathrm{c} = |qB|/m$,

$$\frac{1}{2}\omega_\mathrm{p}^2 + \frac{q}{|q|}\frac{B}{|B|}\omega_\mathrm{c}\omega_\mathrm{r} + \omega_\mathrm{r}^2 = 0. \tag{2.4}$$

The two solutions to the force balance equation

$$\omega_\mathrm{r}^\pm = -\frac{1}{2}\frac{q}{|q|}\frac{B}{|B|}\omega_\mathrm{c}\left(1 \pm \sqrt{1 - 2\frac{\omega_\mathrm{p}^2}{\omega_\mathrm{c}^2}}\right) \tag{2.5}$$

are the two angular frequencies at which the particle's orbit does not change and the motion is a circle around the origin. When the magnetic field is aligned with the longitudinal coordinate axis, $B/|B| = 1$, a positively charged particle will rotate clockwise around the axis and a negatively charged particle counterclockwise. In the following, the latter is assumed to be the case.

$\omega_\mathrm{r}^\pm$ are the two angular velocities at which a rigid rotation of a charged cylinder is

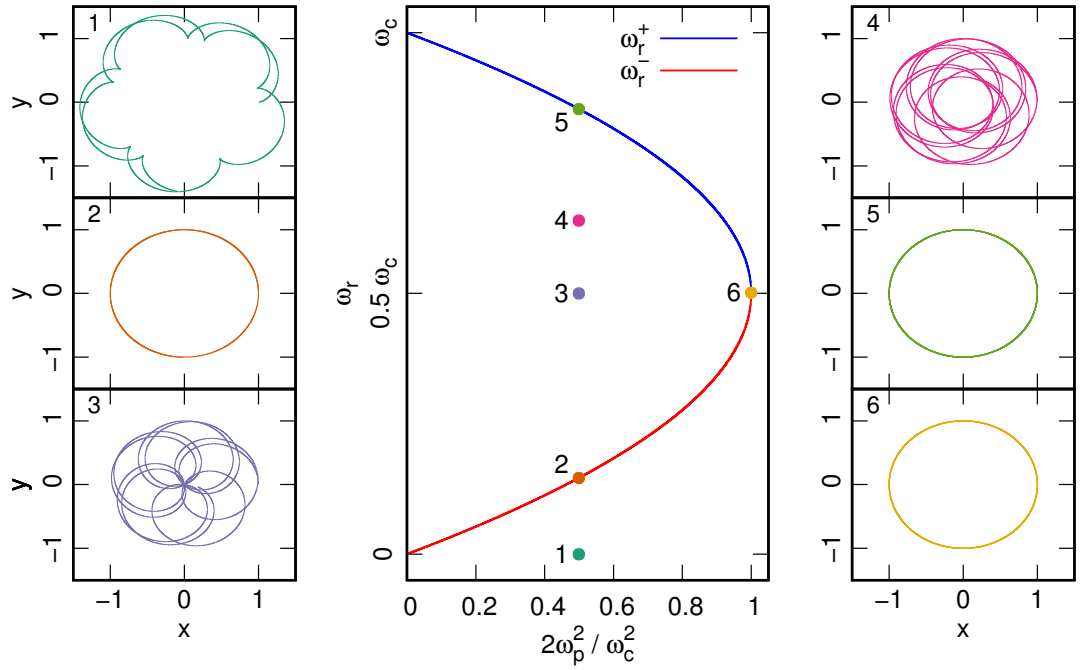

Figure 2.1.: Solutions $\omega_r^{\pm}$ to the force balance equation and the corresponding motion of a test particle. When the initial angular frequency of the test particle is equal to $\omega_r^{\pm}$ (points 2, 5 and 6) the particle simply rotates around the origin. These are points where rigid rotation of a homogeneous beam is possible.

possible. At different values, due to the radial expansion or contraction of the cylinder, the electric field changes, leading to a more complicated type of motion.

Figure 2.1 shows the different kinds of motion for different values of ω_r. At very low density and thus vanishing electric field, the two solutions correspond to a cylinder of fixed charges (no motion) and a cylinder rotating at the cyclotron frequency, at which the radius of rotation becomes equal to the initial radial position of the particle. Increasing the density, ω_r^- has to become larger for the magnetic force to be able to balance the increase in electric field. The inverse is the case for the fast rotation frequency ω_r^+. Its value decreases along with the electric force.

At the high density limit, also called Brillouin Flow limit, where

$$2\frac{\omega_p^2}{\omega_c^2} = 1, \tag{2.6}$$

the values of ω_r^- and ω_r^+ are equal and there is just one angular velocity at which rigid rotation is possible. At even higher density, the magnetic field is not able to balance the electric force any more and particles start escaping.

The motion of a particle in static crossed radial electric and longitudinal magnetic

fields are analytically solvable. The equations of motion are

$$\frac{\mathrm{d}^2}{\mathrm{d}t^2}\begin{pmatrix}x(t)\\y(t)\end{pmatrix} = \frac{1}{2}\omega_\mathrm{p}^2\begin{pmatrix}x(t)\\y(t)\end{pmatrix} + \omega_\mathrm{c}\frac{\mathrm{d}}{\mathrm{d}t}\begin{pmatrix}-y(t)\\x(t)\end{pmatrix}.$$

Transforming $x(t)$ and $y(t)$ to a frame rotating with some frequency ω, i.e.

$$\begin{pmatrix}\tilde{x}(t)\\\tilde{y}(t)\end{pmatrix} = \begin{pmatrix}\cos(\theta) & -\sin(\theta)\\\sin(\theta) & \cos(\theta)\end{pmatrix}^{-1}\begin{pmatrix}x(t)\\y(t)\end{pmatrix} = R(\omega t)^{-1}\begin{pmatrix}x(t)\\y(t)\end{pmatrix},$$

results in

$$\frac{\mathrm{d}^2}{\mathrm{d}t^2}\begin{pmatrix}\tilde{x}(t)\\\tilde{y}(t)\end{pmatrix} = \left(\frac{1}{2}\omega_\mathrm{p}^2 - \omega\omega_\mathrm{c} + \omega^2\right)\begin{pmatrix}\tilde{x}(t)\\\tilde{y}(t)\end{pmatrix} + (\omega_\mathrm{c} - 2\omega)\frac{\mathrm{d}}{\mathrm{d}t}\begin{pmatrix}-\tilde{y}(t)\\\tilde{x}(t)\end{pmatrix}. \tag{2.7}$$

If ω is chosen to be either ω_r^+ or ω_r^-, the first term on the right hand side of equation (2.7) drops out and thus

$$\frac{\mathrm{d}^2}{\mathrm{d}t^2}\begin{pmatrix}\tilde{x}(t)\\\tilde{y}(t)\end{pmatrix} = \pm\left(\omega_\mathrm{r}^+ - \omega_\mathrm{r}^-\right)\frac{\mathrm{d}}{\mathrm{d}t}\begin{pmatrix}\tilde{y}(t)\\-\tilde{x}(t)\end{pmatrix}. \tag{2.8}$$

The solution to this equation,

$$\begin{pmatrix}\tilde{x}(t)\\\tilde{y}(t)\end{pmatrix} = \begin{pmatrix}\tilde{x}_0\\\tilde{y}_0\end{pmatrix} + R\big(\mp\left(\omega_\mathrm{r}^+ - \omega_\mathrm{r}^-\right)t\big)\begin{pmatrix}\alpha\\\beta\end{pmatrix},$$

describes a rotation with $\omega_\mathrm{r}^+ - \omega_\mathrm{r}^-$ around a point, clockwise in a frame rotating with ω_r^+ or counterclockwise in a frame with ω_r^-. The two vectors on the right hand side are given by initial conditions. Transforming back to the laboratory frame,

$$\begin{pmatrix}x(t)\\y(t)\end{pmatrix} = R\big(\omega_\mathrm{r}^\pm\big)\begin{pmatrix}\tilde{x}_0\\\tilde{y}_0\end{pmatrix} + R\big(\omega_\mathrm{r}^\mp\big)\begin{pmatrix}\alpha\\\beta\end{pmatrix}$$

the motion is given as the addition of two points rotating at ω_r^+ and ω_r^- respectively. For a particle starting with some offset on the horizontal axis, $x(t=0) = x_0$ and $y(t=0) = 0$, and some initial angular velocity ω_r ($v_\mathrm{y}(t=0) = \omega_\mathrm{r}x_0$),

$$\begin{pmatrix}x(t)\\y(t)\end{pmatrix} = x_0\left(\omega_\mathrm{r}^+ - \omega_\mathrm{r}^-\right)^{-1}\begin{pmatrix}(\omega_\mathrm{r} - \omega_\mathrm{r}^+)\cos(\omega_\mathrm{r}^- t) + (\omega_\mathrm{r}^- - \omega_\mathrm{r})\cos(\omega_\mathrm{r}^+ t)\\(\omega_\mathrm{r} - \omega_\mathrm{r}^+)\sin(\omega_\mathrm{r}^- t) + (\omega_\mathrm{r}^- - \omega_\mathrm{r})\sin(\omega_\mathrm{r}^+ t)\end{pmatrix}. \tag{2.9}$$

When $\omega_\mathrm{r} = \omega_\mathrm{r}^\pm$, the component of the vector being rotated by the other frequency drops out and equation (2.9) describes a circle.

From (2.9), it is simple to calculate the excursion of a particle starting at some radius r_0 with no velocity by calculating $r(t)^2 = x(t)^2 + y(t)^2$ and finding the point where its

derivative becomes zero a second time. The result is

$$r_{\max} = r_0 \left(1 - 2\frac{\omega_\mathrm{p}^2}{\omega_\mathrm{c}^2}\right)^{-1/2} \approx \left(1 + \frac{\omega_\mathrm{p}^2}{\omega_\mathrm{c}^2}\right) r_0 = \left(1 + \frac{nm}{\epsilon_0 B^2}\right) r_0 = \left(1 + \frac{m}{e\epsilon_0}\frac{I}{v_\mathrm{b}}\frac{1}{\pi R_\mathrm{b}^2}\frac{1}{B^2}\right) r_0,$$

where the approximation holds in the low-density limit.

2.3. Vlasov's equation

One of the fundamental equations of classical statistical mechanics is the Liouville equation

$$\frac{\mathrm{d}f}{\mathrm{d}t} = \frac{\partial f}{\partial t} + \sum_{i=1}^{N}\left(\frac{\partial f}{\partial \mathbf{q}_i}\dot{\mathbf{q}}_i + \frac{\partial f}{\partial \mathbf{p}_i}\dot{\mathbf{p}}_i\right) = 0. \tag{2.10}$$

The density in phase-space f is a function of the canonical coordinates and momenta of all degrees of freedom. For a system of N particles, $f = f(\mathbf{q}_1, \ldots, \mathbf{q}_N, \mathbf{p}_1, \ldots, \mathbf{p}_N)$. (2.10) states that the density in the $6N$ dimensional phase-space remains constant along trajectories given from the solution of Hamilton's equations. This is Liouville's theorem, which in accelerator physics is often used to argue that the beam's phase space remains constant in certain cases.

The Hamiltonian of a system of N charged particles of mass m and charge q, omitting magnetic and external electric fields for shortness, is

$$H = \sum_{i=1}^{N}\left\{\frac{\mathbf{p}_i^2}{2m} + q\sum_{\substack{j=1\\ j<i}}^{N}\varphi_{i,j}\right\}, \tag{2.11}$$

where $\varphi_{i,j} = q\left(4\pi\epsilon_0 \left|\mathbf{q}_i - \mathbf{q}_j\right|\right)^{-1}$. (2.10) can be rewritten as a hierarchy of equations for a reduced probability function [14, p.44]. The functions f_s are defined by integrating over the phase-space coordinates $X_i = (\mathbf{q}_i, \mathbf{p}_i)$ of $(s+1)\ldots N$ particles,

$$f_s(X_1, \ldots, X_s) \propto \int f(X_1, \ldots, X_N)\,\mathrm{d}X_{s+1}\ldots\mathrm{d}X_N.$$

For these f_s and the special choice of Hamiltonian (2.11) [14, p. 43],

$$\frac{\partial f_s}{\partial t} + \sum_{i=1}^{s}\frac{\mathbf{p}_i}{m}\frac{\partial f_s}{\partial \mathbf{q}_i} - q\sum_{i=1}^{s}\sum_{\substack{j=1\\ i\neq j}}^{s}\frac{\partial \varphi_{i,j}}{\partial \mathbf{q}_i}\frac{\partial f_s}{\partial \mathbf{p}_i} = q\sum_{i=1}^{s}\int\frac{\partial \varphi_{i,s+1}}{\partial \mathbf{q}_i}\frac{\partial f_{s+1}}{\partial \mathbf{p}_i}\mathrm{d}X_{s+1}. \tag{2.12}$$

Therefore, the evolution of the s'th distribution function depends on the distribution function of the next order. This hierarchy is called BBGKY hierarchy after the physicists Bogoliubov, Born, Green, Kirkwood and Yvon involved in its derivation. Its solution is identical to that of the full Liouville equation.

The f_s can be written in terms of distribution function of lowest order $\hat{f}(X_1)$ and correlation functions of increasing order

$$\begin{aligned} f_1(X_1) &= \hat{f}(X_1) \\ f_2(X_1, X_2) &= \hat{f}(X_1)\,\hat{f}(X_2) + P(X_1, X_2) \\ &\vdots \end{aligned}$$

The lowest order of (2.12) is then

$$\frac{\partial \hat{f}}{\partial t} + \frac{\mathbf{p}_1}{m}\frac{\partial \hat{f}}{\partial \mathbf{q}_1} - q\frac{\partial \hat{f}}{\partial \mathbf{p}_1}\int \frac{\partial \varphi_{1,2}}{\partial \mathbf{q}_1}\hat{f}(X_2)\,\mathrm{d}X_2 = q\int \frac{\partial \varphi_{1,2}}{\partial \mathbf{q}_1}\frac{\partial P(X_1, X_2)}{\partial \mathbf{p}_1}\mathrm{d}X_2.$$

The evolution of $\hat{f}$ depends on the electric field

$$\mathbf{E}(\mathbf{q}_1) = -\int \frac{\partial \varphi_{1,2}}{\partial \mathbf{q}_1}\hat{f}(X_2)\,\mathrm{d}X_2 = \frac{q}{4\pi\epsilon_0}\int \hat{f}(\mathbf{q}', \mathbf{p})\,\frac{\mathbf{q_1} - \mathbf{q}'}{|\mathbf{q_1} - \mathbf{q}'|^3}\mathrm{d}\mathbf{q}'\mathrm{d}\mathbf{p}$$

and the two-particle correlation function $P(X_1, X_2)$. The evolution of P is then dependent on the three-particle correlation function and so on. Up to this point, no simplification was achieved, since $\hat{f}$ depends on a long chain of unknown correlation functions.

However, if the chain of equations can be truncated at some point, the situation is strongly simplified. For a plasma, the authors in [14, p. 46-48] argue why this should be possible: due to Debye shielding—the statistical redistribution of particles to shield any other charge—the r^{-1} dependence of the potential is modified to $r^{-1}\exp(-r/\lambda_\mathrm{d})$. For this reason, the correlation functions should be increasingly small in the plasma parameter Λ. $\Lambda = (4/3)\pi n\lambda_\mathrm{d}^3$ is the number of particles per Debye sphere. According to the argument, for large numbers, particle correlations become negligible. Then, at any given time, the probability to find a particle in a segment of phase space is completely independent on the location of the other particles.

The equation resulting from $P(X_1, X_2) = 0$ is called Vlasov equation or also collisionless Boltzmann equation,

$$\frac{\partial \hat{f}}{\partial t} + \frac{\mathbf{p}_1}{m}\frac{\partial \hat{f}}{\partial \mathbf{q}_1} + q\mathbf{E}_1\frac{\partial \hat{f}}{\partial \mathbf{p}_1} = 0. \tag{2.13}$$

Together with Poisson's equation for the electric field $\nabla\mathbf{E} = \epsilon_0^{-1}\int \hat{f}\mathrm{d}p$, this results in a closed system. (2.13) has a similar form to the Liouville equation, but only contains the one-particle distribution function. $\hat{f}(\mathbf{q}, \mathbf{p})\,\mathrm{d}\mathbf{q}\mathrm{d}\mathbf{p}$ can be interpreted as the number of particles in an infinitesimal phase space volume. The Vlasov equation then dictates that the density in six-dimensional phase space remains constant along the particle trajectories and therefore, the phase space volume is conserved.

In a system described by the Vlasov equation, particles only interact via the mean electric field and not as individual particles. One illustrative case, where this results in a difference, is a close encounter between two particles in a quasineutral plasma. In this case, the electric field is zero. Vlasov's equation then predicts that particles move in

straight lines. Physically however, when two particles pass by very close to each other, there will be some scattering. Anything resulting from this kind of process is excluded from (2.13).

The Vlasov equation is difficult to solve due to the problem of self-consistency: $\hat{f}$ and the electric field are interdependent and can not be solved for alone. While general solutions do not exist, solutions can be found numerically. The method chosen for the work in this thesis will be presented in Section 3.1. In the following section, a common example from accelerator physics where further simplifications are possible will be given.

2.4. Beam dynamics with space charge: KV envelope equation

When the time in (2.13) is replaced by $s = v_\mathrm{b} t$ as an independent variable and the longitudinal coordinate neglected, it becomes

$$\frac{\mathrm{d}f}{\mathrm{d}s} = \frac{\partial f}{\partial s} + x' \frac{\partial f}{\partial x} + \left(\frac{E_x}{(E\rho)} - k_x^2(s)\, x \right) \frac{\partial f}{\partial x'} + y' \frac{\partial f}{\partial y} + \left(\frac{E_y}{(E\rho)} - k_y^2(s)\, y \right) \frac{\partial f}{\partial y'} = 0. \quad (2.14)$$

$x' = v_\mathrm{x}/v_\mathrm{b}$ and $y' = v_\mathrm{y}/v_\mathrm{b}$ are transverse angles and $(E\rho) = m v_\mathrm{b}^2/q$ the electric rigidity. External forces, which were previously omitted, are included by the $k_\mathrm{x,y}$ terms. To further simplify the situation, moments of (2.14) can be taken. The n'th moment is defined as

$$\overline{x^n} = \int (x - \bar{x})^n \, f\big(x, x', y, y'\big) \, \mathrm{d}x\mathrm{d}x'\mathrm{d}y\mathrm{d}y' \text{ with } \bar{x} = \int x f\big(x, x', y, y'\big) \, \mathrm{d}x\mathrm{d}x'\mathrm{d}y\mathrm{d}y'.$$

The evolution of these moments can be found from their s derivatives. If $\bar{x} = 0$, $\overline{x'} = 0$ initially and $\overline{E_x} = 0$, the first moments $\bar{x}$ and $\overline{x'}$ will remain zero. For the second moments in x,

$$\frac{\mathrm{d}\overline{x^2}}{\mathrm{d}s} = 2\overline{xx'}, \; \frac{\mathrm{d}\overline{xx'}}{\mathrm{d}s} = \overline{x'^2} + (E\rho)^{-1} \, \overline{xE_x} - k_x^2 \overline{x^2} \text{ and } \frac{\mathrm{d}\overline{x'^2}}{\mathrm{d}s} = 2\,(E\rho)^{-1} \, \overline{x'E_x} - 2k_x^2 \overline{xx'}. \quad (2.15)$$

The root-mean-squared (rms) size of the beam is given by $\tilde{x} = \sqrt{\overline{x^2}}$. Its second derivative in s is

$$\frac{\mathrm{d}^2\tilde{x}}{\mathrm{d}s^2} = (E\rho)^{-1} \, \frac{\overline{xE_x}}{\tilde{x}} - k_x^2 \tilde{x} + \frac{\epsilon_x(s)^2}{\tilde{x}^3} = \frac{1}{2} \frac{K}{\tilde{x} + \tilde{y}} - k_x^2 \tilde{x} + \frac{\epsilon_\mathrm{rms,x}(s)^2}{\tilde{x}^3}. \quad (2.16)$$

This equation was first derived by Sacherer in [15] who also found that $\overline{xE_x} \propto \tilde{x}/\,(\tilde{x} + \tilde{y})$ for beams with elliptical symmetry (used in the second step). Therefore, in general, the rms emittance

$$\epsilon_\mathrm{rms,x} = \sqrt{\overline{x^2}\,\overline{x'^2} - \overline{xx'}^2} \quad (2.17)$$

is the only quantity in (2.16) dependent on s. Its value is often used as a measure of the

beam quality [16, p. 58]. The generalized perveance

$$K = \frac{1}{2\pi\epsilon_0}\frac{1}{(E\rho)}\frac{I}{v_\mathrm{b}} = \frac{q}{2\pi\epsilon_0}\frac{I}{mv_\mathrm{b}^3} \tag{2.18}$$

quantifies the strength of the space charge forces.

In a special case, the rms emittance remains constant. This can be seen from

$$\frac{\mathrm{d}\epsilon_{\mathrm{rms,x}}^2}{\mathrm{d}s} = \overline{x^2}\,\overline{x'E_x} - \overline{xx'}\,\overline{xE_x}, \tag{2.19}$$

which can be calculated from the second moments in (2.15). Beyond the trivial case $E_x = 0$, if $E_x \propto x$, the rms emittance also remains preserved. This is the case for a homogeneous distribution of particles in real space. Then, (2.16) only contains known functions. In [17, p.77] it is shown that a homogeneous distribution minimizes the electric field energy and will remain homogeneous.

For a homogeneous beam, the envelopes are $X(s) = 2\tilde{x}(s)$ and $Y(s) = 2\tilde{y}(s)$. The effective emittance is $\epsilon_\mathrm{x} = 4\epsilon_{\mathrm{rms,x}}$. By inserting into (2.16),

$$\begin{aligned}
&\frac{\mathrm{d}^2X(s)}{\mathrm{d}s^2} + k_\mathrm{x}^2(s)\,X(s) - \frac{2K}{X(s)+Y(s)} - \frac{\epsilon_\mathrm{x}^2}{X(s)^3} = 0\\
&\frac{\mathrm{d}^2Y(s)}{\mathrm{d}s^2} + k_\mathrm{y}^2(s)\,Y(s) - \frac{2K}{X(s)+Y(s)} - \frac{\epsilon_\mathrm{y}^2}{Y(s)^3} = 0,
\end{aligned} \tag{2.20}$$

which are the Kapchinsky-Vladimirsky (KV) envelope equations. The KV distribution, which corresponds to a distribution function

$$f\big(x,x',y,y'\big) \propto \delta\Big(1-(x/X)^2-\big(x'/X'\big)^2-(y/Y)^2-\big(y'/Y'\big)^2\Big),$$

is self-consistent under linear focusing, when the paraxial approximation ($v_{x,y} \ll v_b$) holds and longitudinal electric fields are small.

2.4.1. Periodic transport channel

An often used model system in accelerator physics are periodic transport channels. For example, these can be constructed by an alternating combination of focusing and defocusing quadrupole magnets. With an appropriate choice of beam parameters, the beam envelopes $X(s)$ and $Y(s)$ and their derivatives have the same periodicity as the cell length S. When this is the case, the beam is said to be *matched*.

Mathematically, the condition that the beam ellipse is mapped to itself by a transport matrix M can be written as

$$M\begin{pmatrix}\beta_e & -\alpha_e\\ -\alpha_e & \gamma_e\end{pmatrix}M^T = \begin{pmatrix}\beta_e & -\alpha_e\\ -\alpha_e & \gamma_e\end{pmatrix}.$$

α_e, β_e and γ_e are the ellipse parameters. If this condition holds, M can be shown to have

the following parameterization [17, p.107ff],

$$M = \begin{pmatrix} \cos\sigma + \alpha_e \sin\sigma & \beta_e \sin\sigma \\ -\gamma_e \sin\sigma & \cos\sigma - \alpha_e \sin\sigma \end{pmatrix}.$$

Between cells, particles move on their eigenellipses. The phase advance σ is proportional to the phase-space area covered in each cell. In beam dynamics for rings, the tune $Q = 2\pi/\sigma$, which is the number of cells required for the particles to perform one turn around the eigenellipse, is also often used.

For $\sigma > 180°$, with or without space charge, the beam is focused so strongly, that it enters the following cell with a larger diameter. In that case, no periodic solutions exist. If the electric field of the beam becomes non-negligible, the phase advance is reduced from its zero-current value σ_0. With space charge, only phase advances $\sigma_0 < 90°$ are unconditionally stable [17]. When $\sigma_0 > 90°$, σ also has to be larger than 90° [17].

To find the ellipse parameters for which the beam is matched, an algorithm given in [17, p. 60ff] can be used. There, a unitless mismatch factor is defined as

$$\begin{aligned} F &= (\alpha(S) - \alpha(0))^2 - (\beta(S) - \beta(0))(\gamma(S) - \gamma(0)) \\ &= \frac{1}{\epsilon^2}\left(X(S)\,X'(0) - X(0)\,X'(S)\right)^2 + \frac{X(S)^2}{X(0)^2} + \frac{X(0)^2}{X(S)^2} - 2. \end{aligned} \tag{2.21}$$

If the state of the system is defined as $P_i(s) = (X(s), X'(s), Y(s), Y'(s))$, the following iteration minimizes (2.21),

$$P_{i+1}(0) = \frac{1}{2}\left(P_i(0) + P_i(S)\right),$$

where $P_i(S)$ is calculated using numerical integration of the envelope equations. Faster algorithms for beam matching exist. For the purposes in this thesis however (Section 3.4.2), the algorithm was found to work satisfactorily.

2.4.2. Calculation of phase advance from a simulated map

Following an idea by J. Struckmeier [18], given a mapping of particle locations and angles between two positions, a matrix can be found, that reproduces the given transformation as well as possible. From this matrix, an approximate value of the phase advance σ can be determined. This algorithm is utilized in Section 3.4.2 to obtain an estimate for σ. One way to obtain a fit is to minimize the sum of the squared differences between the transformed initial (index i) and the final particle (index f) states.

$$\text{Minimize } \forall p\text{:} \quad \vec{S}_p = \begin{pmatrix} m_{11} & m_{12} \\ m_{21} & m_{22} \end{pmatrix} \begin{pmatrix} r_p^{\mathrm{i}} \\ r_p'^{\mathrm{i}} \end{pmatrix} - \begin{pmatrix} r_p^{\mathrm{f}} \\ r_p'^{\mathrm{f}} \end{pmatrix}$$

$$S = \frac{1}{N}\sum_{p=1}^{N}\left[\gamma^2\left(m_{11}r_p^{\mathrm{i}} + m_{12}r_p'^{\mathrm{i}} - r_p^{\mathrm{f}}\right)^2 + \gamma'^2\left(m_{21}r_p^{\mathrm{i}} + m_{22}r_p'^{\mathrm{i}} - r_p'^{\mathrm{f}}\right)^2\right]$$

γ and γ' normalize the residual to a unit-less value.

Minimizing the residual, $\mathrm{d}S/\mathrm{d}m_{ij} = 0$, leads to two independent linear system of equations for m_{1j} and m_{2j}.

$$\begin{pmatrix}0\\0\end{pmatrix} = \frac{1}{2}\begin{pmatrix}\frac{\mathrm{d}S}{\mathrm{d}m_{11}}\\\frac{\mathrm{d}S}{\mathrm{d}m_{12}}\end{pmatrix} = \gamma^2 Q\begin{pmatrix}m_{11}\\m_{12}\end{pmatrix} - \frac{\gamma^2}{N}\sum_{p=1}^{N}\begin{pmatrix}r_p^{\mathrm{i}} r_p^{\mathrm{f}}\\ r_p'^{\mathrm{i}} r_p^{\mathrm{f}}\end{pmatrix}$$

$$\begin{pmatrix}0\\0\end{pmatrix} = \frac{1}{2}\begin{pmatrix}\frac{\mathrm{d}S}{\mathrm{d}m_{21}}\\\frac{\mathrm{d}S}{\mathrm{d}m_{22}}\end{pmatrix} = \gamma'^2 Q\begin{pmatrix}m_{21}\\m_{22}\end{pmatrix} - \frac{\gamma'^2}{N}\sum_{p=1}^{N}\begin{pmatrix}r_p^{\mathrm{i}} r_p'^{\mathrm{f}}\\ r_p'^{\mathrm{i}} r_p'^{\mathrm{f}}\end{pmatrix}$$

$$Q = \frac{1}{N}\sum_{p=1}^{N}\begin{pmatrix}\left(r_p^{\mathrm{i}}\right)^2 & r_p^{\mathrm{i}} r_p'^{\mathrm{i}}\\ r_p^{\mathrm{i}} r_p'^{\mathrm{i}} & \left(r_p'^{\mathrm{i}}\right)^2\end{pmatrix} = \begin{pmatrix}\overline{r^{\mathrm{i}2}} & \overline{r^{\mathrm{i}} r'^{\mathrm{i}}}\\ \overline{r^{\mathrm{i}} r'^{\mathrm{i}}} & \overline{r'^{\mathrm{i}2}}\end{pmatrix}$$

The matrix Q is known as the beam matrix. The weights γ and γ' drop out of the calculation of the coefficients of M. Inverting for M, results in

$$M = \left[\frac{1}{N}\sum_{p=1}^{N}\begin{pmatrix}r_p^{\mathrm{i}} r_p^{\mathrm{f}} & r_p'^{\mathrm{i}} r_p^{\mathrm{f}}\\ r_p^{\mathrm{i}} r_p'^{\mathrm{f}} & r_p'^{\mathrm{i}} r_p'^{\mathrm{f}}\end{pmatrix}\right] Q^{-1}.$$

The phase advance can then be calculated by taking the trace of M,

$$\sigma = \arccos\left(\frac{1}{2}\mathrm{Tr}(M)\right).$$

Therefore, all that is required for the determination of the phase advance are the initial second moments as well as those between the initial and final values.

3. The codes *bender* and *tralitrala*

In the previous chapter, it was motivated that the Vlasov equation along with Poisson's equation provides a description of a system of charged particles,

$$\frac{\partial f_j(\mathbf{r},\mathbf{v})}{\partial t} + \mathbf{v}\frac{\partial f_j(\mathbf{r},\mathbf{v})}{\partial \mathbf{r}} + \frac{q_j}{m_j}\left(\mathbf{E} + \mathbf{E}_{\text{ext}} + \mathbf{v}\times\mathbf{B}_{\text{ext}}\right)\frac{\partial f_j(\mathbf{r},\mathbf{v})}{\partial \mathbf{v}} = 0, \tag{3.1}$$

$$\nabla\mathbf{E} = \frac{\rho(\mathbf{r})}{\epsilon_0} = \frac{1}{\epsilon_0}\sum_j q_j \int f_j(\mathbf{r},\mathbf{v})\,\mathrm{d}\mathbf{v}. \tag{3.2}$$

These equations include multiple species (index j) as well as external electric and magnetic fields, which were previously ignored.

In the derivation two important approximations were made:

- The particle velocities are much smaller than the speed of light and the motion is non-relativistic.

- The magnetic self-fields have been omitted. Beyond the field produced by the particle currents, in the electrostatic approximation, propagation of electromagnetic waves is also excluded. Such an approximation should be valid for the simulations presented in this thesis. In Chapter 4, the focus lies on the steady state properties, where the electric field remains constant. For both Chapter 4 and Chapter 5, the current densities are low enough not to produce a significant magnetic field.

There are various approaches to numerically solving the system (3.1) and (3.2). One class of algorithms [19] introduces a grid in phase-space on which (3.1) is discretized. Due to the six-dimensional grid required for three space dimensions, the computational effort required by these methods can become very large. Additionally, the grid needs to be fine enough to resolve the structures of interest in phase-space.

The approach chosen for the simulations in this thesis is the particle-in-cell (PIC) method. To solve (3.1), simulation particles are reintroduced to sample the phase space. PIC methods only require a grid in real space and are therefore computationally not as expensive in higher dimensions. However, due to the statistical sampling, problems from noise can occur and alter the results.

In the following section a derivation of the PIC algorithm will be sketched. Section 3.2 presents the algorithms used in the 3d PIC code written for the work in this thesis, along with some implementation details. Following similar principles, a 2d code was also implemented, which is presented in Section 3.3. Finally, in Section 3.4, two tests of the written codes against self-consistent solutions will be presented.

3.1. The particle-in-cell algorithm

By using an ansatz for the phase-space density f, the calculations required for the particle-in-cell method can be derived. The derivation follows [20]. It is given in only one dimension to reduce the complexity of the equations. However, the same approach works for two or more dimensions. For further simplification, external magnetic fields are ignored.

The phase-space density is assumed to be covered by macroparticles with a finite size,

$$f(t,x,v) = \sum_i N_i S(x - x_i(t))\, \delta(v - v_i(t))\,. \tag{3.3}$$

The functions $x_i(t)$ and $v_i(t)$ are degrees of freedom which will be identified with the macroparticle position and velocity later on. The shape function $S(x)$ has to satisfy three conditions:

1. Compact support: The function is non-zero only in a "small" range around 0.
2. Normalization: $\int_{-\infty}^{\infty} S(x)\,\mathrm{d}x = 1$
3. Symmetry: $S(x) = S(-x)$

In velocity space, the macroparticles are points, so that they do not spread out over time. The density $n(t,x) = \int_{-\infty}^{\infty} \mathrm{d}v\, f(t,x,v)$ of particles can be calculated from f via

$$n(x) = \sum_i N_i S(x - x_i(t)) \int_{-\infty}^{\infty} \delta(v - v_i(t))\,\mathrm{d}v = \sum_i N_i S(x - x_i(t))\,.$$

The total number of (physical) particles is then

$$N = \int_{-\infty}^{\infty} n(x)\,\mathrm{d}x = \sum_i N_i \int_{-\infty}^{\infty} S(x - x_i(t))\,\mathrm{d}x = \sum_i N_i.$$

Thus, the N_i are the numbers of particles per phase-space volume covered by macroparticle i.

3.1.1. Equation of motion

By looking at the evolution of the first order moments in x and v of the Vlasov equation, the equation of motion can be found for the macroparticles. For compactness only the solutions will be given here. The full calculation can be found in appendix A. The first moment in space is

$$0 = \int x \frac{\mathrm{d}f}{\mathrm{d}t} \mathrm{d}x\mathrm{d}v = \int x \left\{ \frac{\partial f}{\partial t} + v\frac{\partial f}{\partial x} + \frac{q}{m} E(x) \frac{\partial f}{\partial v} \right\} \mathrm{d}x\mathrm{d}v = \sum_i \left(\frac{\partial x_i(t)}{\partial t} - v_i(t) \right). \tag{3.4}$$

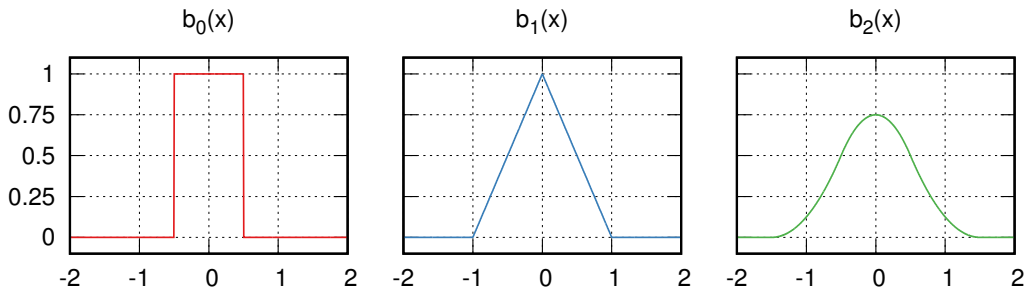

Figure 3.1.: The three b splines of lowest order.

The first moment in velocity space is

$$0 = \int v \frac{\mathrm{d}f}{\mathrm{d}t} \mathrm{d}x \mathrm{d}v = \sum_i \left(\frac{\partial v_i(t)}{\partial t} - \frac{q}{m} \int_{-\infty}^{\infty} E(x)\, S(x - x_i(t))\, \mathrm{d}x \right). \tag{3.5}$$

According to equation (3.4) and (3.5), which are Newton's equations, the macroparticles move just like real particles. However, the electric field is replaced by the convolution of the field with the particle shape function.

For the shape of the particles, b-splines are often chosen [21, p. 142]. The first function is defined as

$$b_0(x) = \begin{cases} 1 & |x| < 1/2 \\ 0 & |x| \geq 1/2 \end{cases} \tag{3.6}$$

and functions of higher order as convolution with $b_0(x)$,

$$b_n(x) = \int_{-\infty}^{\infty} b_0\big(x - x'\big)\, b_{n-1}\big(x'\big)\, \mathrm{d}x'. \tag{3.7}$$

The first three b's are displayed in Figure 3.1. For a PIC code of order n with a particle size the same as the grid spacing Δx, $S(x) = (1/\Delta x) b_n(x/\Delta x)$.

The Vlasov equation needs to be solved self-consistently with Poisson's equation. Most approaches use a grid spanning the computational volume. From the ansatz for f (3.3), instructions how to calculate the charge density on the grid as well as how to interpolate the electric field can be derived. If the grid points are equidistantly spaced with Δx and the grid cells defined as centered around the grid points, the charge density on the grid can be calculated from the average of $\rho(x)$ over a cell. Then, for the j'th point,

$$\begin{aligned} \rho_j &= \frac{1}{\Delta x} \int_{x_{j-\frac{1}{2}}}^{x_{j+\frac{1}{2}}} \rho(x)\, \mathrm{d}x = \frac{q}{\Delta x} \sum_i N_i \int_{x_{j-\frac{1}{2}}}^{x_{j+\frac{1}{2}}} S(x - x_i(t))\, \mathrm{d}x \\ &= \frac{q}{\Delta x^2} \sum_i N_i \int_{-\infty}^{\infty} b_n\left(\frac{x - x_i(t)}{\Delta x} \right) b_0\left(\frac{x - x_j}{\Delta x} \right) \mathrm{d}x \end{aligned}$$

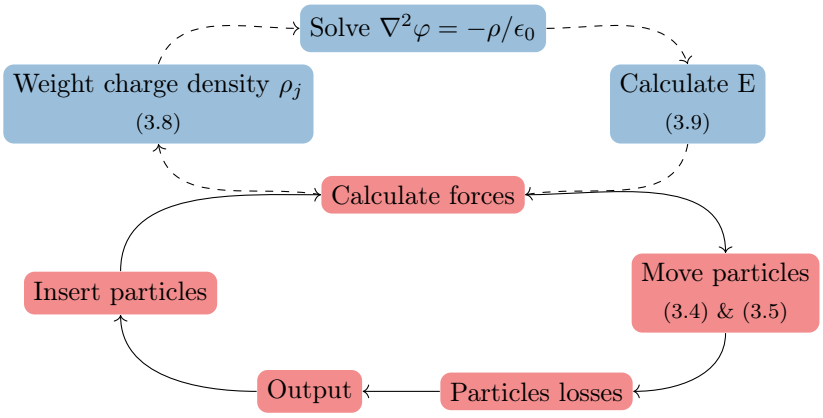

Figure 3.2.: Particle-in-cell algorithm.

$$= \frac{q}{\Delta x} \sum_i N_i b_{n+1}\left(\frac{x_j - x_i(t)}{\Delta x}\right). \tag{3.8}$$

Assuming that the electric field has a constant value E_j within a grid cell, i.e. between $x_{j-\frac{1}{2}}$ and $x_{j+\frac{1}{2}}$,

$$\begin{aligned}\int E(x)\, S(x - x_i(t))\, \mathrm{d}x &= \sum_j E_j \int_{-\infty}^{\infty} S(x - x_i(t))\, b_0\left(\frac{x - x_j}{\Delta x}\right) \mathrm{d}x \\ &= \sum_j E_j b_{n+1}\left(\frac{x_j - x_i(t)}{\Delta x}\right). \end{aligned} \tag{3.9}$$

Therefore, both the charge density and the electric field are interpolated using the same type of function as $S(x)$, but with the order increased by one.

For *bender*, $n = 0$ and therefore $S(x) = (1/\Delta x) b_0(x/\Delta x)$ was chosen (in all three dimensions), where the particle "size" is set to the grid spacing Δx. This choice leads to the *cloud-in-cell* (CIC) version of the particle-in-cell algorithm. A delta-function, $S(x) = \delta(x)$, leads to the *nearest-grid-point* (NGP) version.

The charge assignment (3.8) and the field interpolation (3.9) are reduced to linear interpolation for the cloud-in-cell version. Charges and fields are weighted proportionally to the distance to the opposite grid point. For example, equation (3.9) becomes

$$\int E(x)\, S(x - x_i(t))\, \mathrm{d}x = \underbrace{\left(1 - \frac{x_i(t) - x_j}{\Delta x}\right)}_{\text{rel. distance to } x_{j+1}} E_j + \underbrace{\left(\frac{x_i(t) - x_j}{\Delta x}\right)}_{\text{rel. distance to } x_j} E_{j+1}. \tag{3.10}$$

Figure 3.2 contains a schematic of the main particle-in-cell loop. How to implement the important parts of the algorithm—the solution of Poisson's equation on the grid and the integration of Newton's equations—has not been specified yet. These will be explained in the following section.

3.2. Implementation of the particle-in-cell code *bender*

3.2.1. Integration of motion

The Velocity Verlet algorithm (in its positional form, [22]), can be derived by expanding the particle positions at the preceding and the advanced time step,

$$\mathbf{r}(t+\Delta t) = \mathbf{r}(t) + \left.\frac{\partial \mathbf{r}}{\partial t}\right|_t \Delta t + \frac{1}{2}\left.\frac{\partial^2 \mathbf{r}}{\partial t^2}\right|_t \Delta t^2 + \mathcal{O}\left(\Delta t^3\right) \tag{3.11}$$

$$\mathbf{r}(t-\Delta t) = \mathbf{r}(t) - \underbrace{\left.\frac{\partial \mathbf{r}}{\partial t}\right|_t}_{\mathbf{v}(t)} \Delta t + \frac{1}{2}\underbrace{\left.\frac{\partial^2 \mathbf{r}}{\partial t^2}\right|_t}_{\mathbf{a}(t)} \Delta t^2 + \mathcal{O}\left(\Delta t^3\right) \tag{3.12}$$

Combining (3.11) and (3.12) leads to a version of the algorithm that calculates the new particle position from the two previous positions. The velocity $\mathbf{v}(t)$ can then be calculated using the centered-difference,

$$\mathbf{v}(t) = \left(\mathbf{r}(t+\Delta t) - \mathbf{r}(t-\Delta t)\right)/(2\Delta t). \tag{3.13}$$

To calculate the velocity at time t requires the knowledge of the particle position at $t+\Delta t$. To start a simulation, the positions would have to be known in two adjacent time steps.

Using (3.11) to update the particle positions, adding the expansion for $\mathbf{r}(t+\Delta t)$ and $\mathbf{r}(t+2\Delta t)$ and inserting (3.13) leads to the Velocity Verlet algorithm. For the Lorentz force and using momenta instead of velocities, it reads

$$\mathbf{p}\left(t+\frac{1}{2}\Delta t\right) = \mathbf{p}(t) + \frac{q\Delta t}{2}\mathbf{E}(\mathbf{r}(t)) + \frac{q\Delta t}{2m}\mathbf{p}(t)\times\mathbf{B}(\mathbf{r}(t)) \tag{3.14}$$

$$\mathbf{r}(t+\Delta t) = \mathbf{r}(t) + \frac{\Delta t}{m}\mathbf{p}\left(t+\frac{1}{2}\Delta t\right) \tag{3.15}$$

$$\begin{aligned}\mathbf{p}(t+\Delta t) = \mathbf{p}\left(t+\frac{1}{2}\Delta t\right) &+ \frac{q\Delta t}{2}\mathbf{E}(\mathbf{r}(t+\Delta t)) \\ &+ \frac{q\Delta t}{2m}\mathbf{p}(t+\Delta t)\times\mathbf{B}(\mathbf{r}(t+\Delta t))\,.\end{aligned} \tag{3.16}$$

Introducing a matrix

$$\Omega = \begin{pmatrix} 0 & B_z & -B_y \\ -B_z & 0 & B_x \\ B_y & -B_x & 0 \end{pmatrix}, \text{ where } \Omega \begin{pmatrix} v_x \\ v_y \\ v_z \end{pmatrix} = \begin{pmatrix} v_x \\ v_y \\ v_z \end{pmatrix} \times \begin{pmatrix} B_x \\ B_y \\ B_z \end{pmatrix},$$

(3.16) can be inverted:

$$\mathbf{p}(t+\Delta t) = \left(\mathbb{1} - \frac{q\Delta t}{2m}\Omega(t+\Delta t)\right)^{-1}\left(\mathbf{p}\left(t+\frac{1}{2}\Delta t\right) + \frac{q\Delta t}{2}\mathbf{E}(\mathbf{r}(t+\Delta t))\right), \tag{3.17}$$

where (with $\tilde{B}_i = q\Delta t/(2m)B_i$): $(\mathbb{1} - q\Delta t/(2m)\Omega(t+\Delta t))^{-1}$

$$= \left(1 + \tilde{B}_x^2 + \tilde{B}_y^2 + \tilde{B}_z^2\right)^{-1} \begin{pmatrix} 1+\tilde{B}_x^2 & \tilde{B}_x\tilde{B}_y + \tilde{B}_z & \tilde{B}_x\tilde{B}_z - \tilde{B}_y \\ \tilde{B}_x\tilde{B}_y - \tilde{B}_z & 1+\tilde{B}_y^2 & \tilde{B}_y\tilde{B}_z + \tilde{B}_x \\ \tilde{B}_x\tilde{B}_z + \tilde{B}_y & \tilde{B}_y\tilde{B}_z - \tilde{B}_x & 1+\tilde{B}_z^2 \end{pmatrix}.$$

The algorithm is second-order accurate in time [23] and can be shown to be time-reversible, i.e. a step by Δt followed by a step by $-\Delta t$ results in the original position and momentum.

The implementation in *bender* calculates (3.14) after (3.15) and (3.17), i.e. calculates $\mathbf{p}\left(t + {}^3\!/_2\Delta t\right)$. Thus, for each step, the forces from the electric and magnetic fields have to be evaluated only once. In the calculations made in Chapter 4 and Chapter 5, it was found that the time taken for the evaluation of the field values typically outweighs the calculations to update the particle's position and momenta. Hence, for these applications, the Velocity Verlet algorithm is preferable over lower-order integrators (like a symplectic Euler scheme) or higher order integrators, which require more field evaluations per step.

A number of physical systems were used to test the implementation of the integrator: a pendulum implemented using electric fields, the gradient B drift described in Section 2.1 and the motion of particles in a radial electric and longitudinal magnetic field, a configuration described in Section 2.2. The integrated motion was compared to the results from the standard Runge-Kutta scheme (RK4) [24].

Figure 3.3 shows the phase space of the pendulum for three different initial conditions with the parameters $m = 1\,\mathrm{kg}$, $q = 1\,\mathrm{C}$ and $E(x) = -1\,\mathrm{V\,m^{-1}}\sin(\pi x)$. For a low initial amplitude, the solution behaves like an harmonic oscillator, while at larger initial amplitudes the oscillation time increases. The Velocity Verlet algorithm follows the behaviour of a symplectic integrator: the energy of the particle oscillates within fixed bounds, which were found to decrease quadratically with the timestep. This behaviour is different from the standard RK4 integrator, where the energy constantly decreases over time. This can also be observed in the phase space plot in Figure 3.3a, where the solution found using the RK4 algorithm slowly spirals towards 0.

For different time steps Δt, Figure 3.4a shows the oscillation times of four particles with different initial amplitudes compared to the analytic value. For larger time steps, the oscillation frequency of the numerical solution was found to be smaller than the physical value. To reproduce the oscillation time for example to 1%, more than 10 timesteps per period were required.

The integrator also correctly reproduces effects in inhomogeneous magnetic field, such as the gradient B drift. Figure 3.4b contains the deviation of the total downward drift as well as the oscillation time for different time steps from the correct values. In this case, the revolution time approaches the correct value from higher values.

Figure 3.5 shows some results for the integration of particle motion (m=1 kg, q=1 C) in a radial electric field ($E_\mathrm{r} = 0.1\,\mathrm{V\,m^{-1}}r$) and homogeneous magnetic field ($B_z = 1\,\mathrm{T}$). This is the field configuration already discussed in Section 2.2. Just as in the previous tests, the energy oscillates but remains bounded over long periods of time. The amplitude of this oscillation is displayed in Figure 3.5b. It shrinks proportional to the square of the time

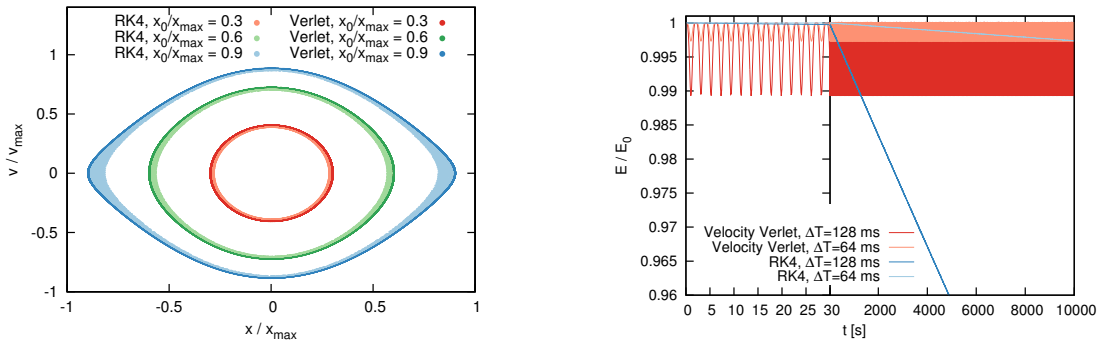

(a) Phase space.

(b) Energy.

Figure 3.3.: Comparison of a standard RK4 integrator to the Velocity Verlet algorithm for particle motion in inhomogeneous electric fields.

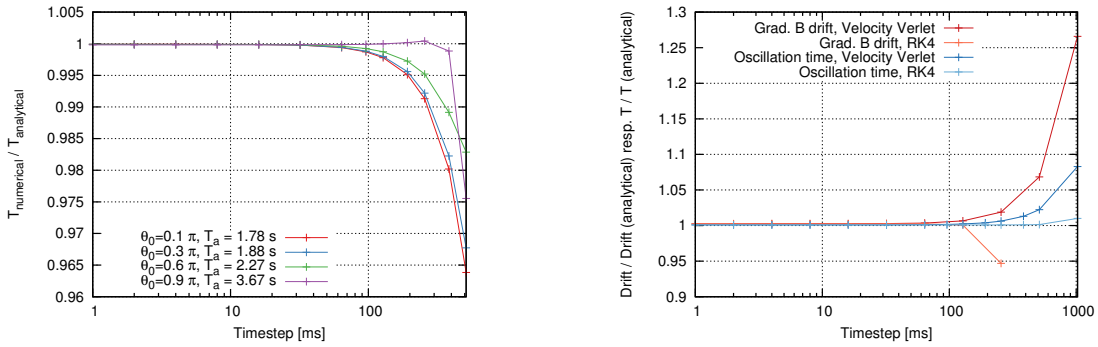

(a) Oscillation period of the "electric" pendulum.

(b) Oscillation period and downward drift in the gradient B test.

Figure 3.4.: Deviation of the oscillation period from the analytically calculated value for the "electric" pendulum and in the gradient B drift simulation.

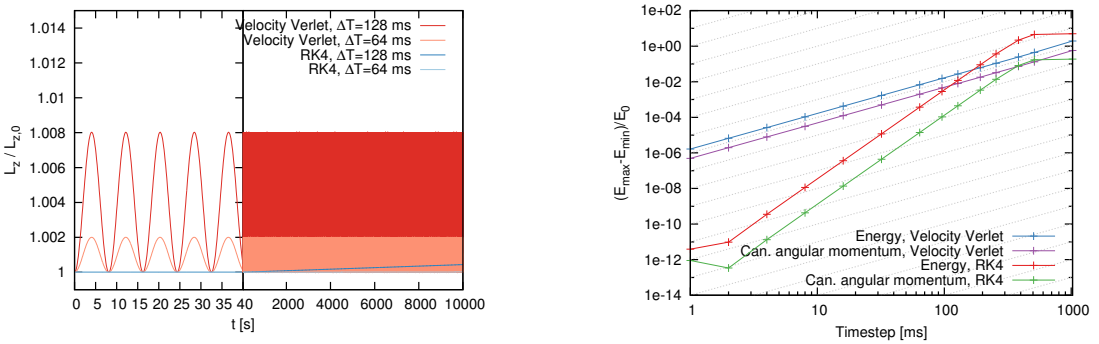

(a) Behaviour of the longitudinal component of the canonical angular momentum.

(b) Deviation of energy and angular momentum from its initial value over the period of time shown in (a).

Figure 3.5.: Comparison of a standard RK4 integrator to the Velocity Verlet algorithm for particle motion in a radial electric field and longitudinal homogeneous field.

step (grey curves). The canonical angular momentum $L_z = xp_y - yp_x + qB_z\left(x^2 + y^2\right)/2$ shows a similar behaviour. Here, the solution by the RK4 method shows a continuous increase in angular momentum.

These simple tests suggest that the Velocity Verlet algorithm is a good candidate for long-time integration of motion in electromagnetic fields.

3.2.2. Solver for Poisson's equation

As an electrostatic particle-in-cell code, *bender* has to solve Poisson's equation

$$\nabla^2\varphi(x,y,z) = \left(\frac{\partial^2}{\partial x^2} + \frac{\partial^2}{\partial y^2} + \frac{\partial^2}{\partial z^2}\right)\varphi(x,y,z) = -\frac{1}{\epsilon_0}\rho(x,y,z)$$

at least once in every timestep to obtain the potential as well as the electric field of the particles. A number of common algorithms were implemented: a solver in three-dimensions as well as a solver for radially symmetric geometries using a finite difference approximation and a three dimensional solver using Fourier transforms. The best choice depends on the geometry of the system as well as on the time available for the calculation.

In the next section, these algorithms and their implementation will be presented.

Finite difference 3d solver

Finite difference approximations of differential equations replace the derivatives by corresponding difference quotients on a grid. The three-dimensional Cartesian solver implemented for *bender* uses the Shortley-Weller [25] approximation. In each dimension, the second derivative is replaced by

$$\begin{aligned}\left.\frac{\partial^2\varphi(x)}{\partial x^2}\right|_{x=x_i} \approx{}& \frac{2}{\Delta_-\left(\Delta_+ + \Delta_-\right)}\varphi_{i-1} - \frac{2}{\Delta_+\Delta_-}\varphi_i + \frac{2}{\Delta_+\left(\Delta_+ + \Delta_-\right)}\varphi_{i+1} \\ &+ \mathcal{O}(\Delta_-(1-\lambda)) + \mathcal{O}\left(\left(\lambda^2 - \lambda + 1\right)\Delta_-^2\right), \qquad \lambda = \Delta_+/\Delta_-.\end{aligned} \tag{3.18}$$

Δ_+ and Δ_- are the grid spacings to both sides of the grid point. When the spacing is equal in both directions, $\Delta = \Delta_+ = \Delta_-$ ($\lambda = 1$), the truncation error is of order Δ^2. In the presence of conductors, the grid spacing can be changed locally to move neighboring points to their surface. An example for this is shown in Figure 3.6a.

Applying (3.18) to each grid point produces a large system of equations. These couple the potential value $\varphi_{i,j,k}$ at each grid point to its six neighbors and the charge density $\rho_{i,j,k}$. At the grid boundaries, the implementation supports Dirichlet, Neumann and periodic boundary conditions.

In the first case, the value of the potential at the boundary is known and does not need to be solved for. The term containing the affected point in the equation of neighboring points can be moved to the right-hand side of Poisson's equation. Periodic boundary conditions can be implemented by replacing all occurrences of φ_N by φ_0 and φ_{-1} by φ_{N-1} (on a grid of N points, $i \in [0, N-1)$).

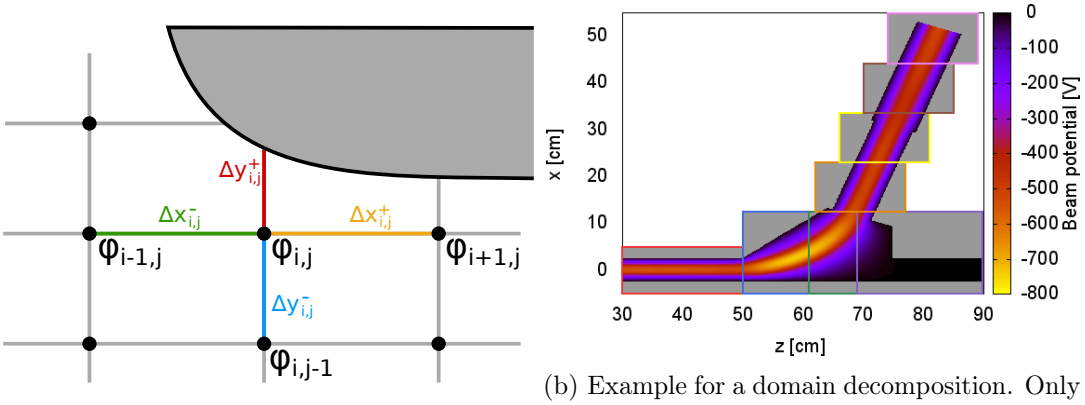

(a) Shortley-Weller finite difference stencil at a conducting surface.

(b) Example for a domain decomposition. Only the gray parts of the domain are considered for the computation.

Figure 3.6.: Finite difference stencil and an example for domain decomposition.

For Neumann boundary conditions, the normal derivative $\mathbf{n} \cdot \nabla\varphi(x, y, z) = E_n$ is specified, where $\mathbf{n}$ is the normal on some surface. *bender* only handles the case where $\mathbf{n}$ is pointing along one of the coordinate axes and the grid point is located on one of the surfaces of the Cartesian grid. In this case, the boundary condition can be approximated by finite difference, here for example for $i = 0$, by $(\varphi_1 - \varphi_{-1}) / (2\Delta) = -E_n$. Solving for φ_{-1} and inserting, (3.18) then becomes

$$\frac{\partial^2\varphi(x)}{\partial x^2}\Big|_{x=x_0} \approx -\frac{2E_\mathrm{n}}{\Delta} + \frac{2}{\Delta^2}\left(\varphi_1 - \varphi_0\right).$$

Once again, the first term can then be moved to the right hand side of Poisson's equation.

Including boundary conditions, (3.18) produces a system of linear equations for the potential. The problem can be written in matrix form as $A\mathbf{x} = \mathbf{b}$. Since each grid point only references its neighbors, the matrix A is only sparsely populated with a maximum of 7 non-zeros per row. Various methods exist to solve these systems efficiently:

- *Relaxation methods* work by repeatedly calculating $\varphi_{i,j,k}$ from its neighboring values using (3.18). The algorithms are relatively simple to implement but converge more slowly than other methods [26]. However, in combination with a hierarchy of grids, these methods are good at smoothing high-frequency components in the solution error. These *Multigrid* methods are able to find a solution in $\mathcal{O}(N)$ steps, where N is the total number of grid points. Due to the effort involved in implementing such a solver in the presence of an arbitrary boundary geometry, such a solver was not implemented.

- Krylov subspace methods [27] are iterative algorithms, which in the m'th iteration build an approximation of the solution from the Krylov subspace

$$\mathcal{K}_m(A, \mathbf{r}_0) = \mathrm{span}\left\{\mathbf{r}_0, A\mathbf{r}_0, A^2\mathbf{r}_0, \ldots, A^{m-1}\mathbf{r}_0\right\},$$

where $r_0 = \mathbf{b} - A\mathbf{x}_0$ is the residual of some initial solution $\mathbf{x}_0$. A large number of algorithms exist which differ in the choice of the new approximation vector $\mathbf{x}_m \in \mathcal{K}_m(A, \mathbf{r}_0)$. Here, the Generalized Minimal Residual (GMRES) algorithm [28] or the Biconjugate Gradient Stabilized (BiCGStab) were used.

- The solution of $A\mathbf{x} = \mathbf{b}$ can also be calculated directly, for example using Gaussian elimination. Another procedure, LU decomposition, first splits the matrix A into a lower and an upper triangular matrix such that $A = LU$, which then allows to calculate the solution by forward and backward substitution, $L\mathbf{y} = \mathbf{b}$ and then $U\mathbf{x} = \mathbf{y}$. These methods have the advantage, that once L and U are known, the solution $\mathbf{x}$ can be repeatedly calculated very efficiently for different $\mathbf{b}$. However L and U are not necessarily as sparse as A, sometimes vastly increasing the required memory to store the matrices. For the grids used in Chapter 5, the matrices have millions of unknown and using LU decomposition is not feasible. For the two dimensional solver presented below, using LU decomposition provides an increase in speed compared to the Krylov subspace methods.

bender uses the PetSc [29] library for all sparse matrix operations. PetSc provides parallel implementations of all of the algorithms listed above.

Once the solution is known, the electric field components at each grid point are calculated from the potential by using

$$E_{\mathrm{x},i} = -\left.\frac{\partial\varphi(x)}{\partial x}\right|_{x=x_i} \approx \frac{\Delta_+}{\Delta_-\left(\Delta_- + \Delta_+\right)}\varphi_{i-1} - \frac{\Delta_+ - \Delta_-}{\Delta_-\Delta_+}\varphi_i - \frac{\Delta_-}{\Delta_+\left(\Delta_- + \Delta_+\right)}\varphi_{i+1} + \mathcal{O}(\Delta_+\Delta_-)\,. \tag{3.19}$$

The electric field is then interpolated to each particle's position by linear interpolation.

To generate the sparse matrix, the distances $\Delta_\pm$ in all directions have to be found. These are calculated by testing each grid line for intersections against a given list of boundary elements. In the first iteration, along the x-axis, each grid point outside a boundary element is assigned an index in ascending order. This index is then used for all local data arrays. To avoid storing the grid spacing for each of these "active" grid points (which would require 48 byte per point), a bitset only stores if such information is present (1 byte per point). This enables the code to quickly check if a grid point is located close to a boundary or is regular. The distance to the boundary is then stored in a binary-search tree. After indexing, a global index is calculated from the local index, which numbers the rows in the system matrix and which is used to reference grid points in communication between processors.

For the right hand side of the system, two vectors are maintained: one containing the charge density and one containing contributions by the boundary conditions. In cases where only the charge density changes between successive solves, a recalculation of the second vector can thus be avoided.

For parallel computations, the solver allows rectangular parts of the global grid to be handed to different processors. Parts not assigned to a processor are not considered for

the calculation. An example is shown in Figure 3.6b. Since the sides of the computational domains do not necessarily have to be aligned, before indexing, each processor checks the list of computational domains for its neighbors and numbers those parts of its boundary that are not adjacent to another processor for reference by the user.

Fast Fourier solver

bender includes an implementation of the well-known Fast Fourier algorithm [21, 30].

In the discrete case, the second derivatives in Poisson's equation lead to a relation between potential values on different grid points. This necessitates the use of solution methods like the sparse matrix methods employed for the finite difference solver. However, when the solution is expanded in eigenfunctions of the differential operator, the expansion coefficients are decoupled. The choice of function depends on the boundary conditions. For example, in the case of zero potential on both sides of a domain of length L on a grid of N grid points, when the potential $\varphi(x)$ and the charge density $\varphi(x)$ are expanded using sine functions

$$\varphi(x) = 2 \sum_{k=0}^{N-1} \tilde{\varphi}_k \sin\Big(\pi\,(k+1)\,\frac{x}{L}\Big)\,, \tag{3.20}$$

the differential equation $\mathrm{d}^2\varphi(x)\,/\mathrm{d}x^2 = -\rho(x)$ turns into

$$-2 \sum_{k=0}^{N-1} \tilde{\varphi}_k \left[\frac{\pi}{L}\,(k+1)\right]^2 \sin\Big(\pi\,(k+1)\,\frac{x}{L}\Big) = -2 \sum_{k=0}^{N-1} \tilde{\rho}_k \sin\Big(\pi\,(k+1)\,\frac{x}{L}\Big)\,.$$

Due to the linear independence of the sine, $\tilde{\varphi}_k = \left[\frac{\pi}{L}\,(k+1)\right]^{-2} \tilde{\rho}_k$.

On "simple" geometries such as rectangular domains, Poisson's equation is separable i.e. the solution has the form $\varphi(x,y,z) = \varphi_\mathrm{x}(x) \cdot \varphi_\mathrm{y}(y) \cdot \varphi_\mathrm{z}(z)$ and

$$\nabla^2\varphi(x,y,z) = \frac{\mathrm{d}^2\varphi_\mathrm{x}(x)}{\mathrm{d}x^2}\varphi_\mathrm{y}(y)\,\varphi_\mathrm{z}(z) + \varphi_\mathrm{x}(x)\,\frac{\mathrm{d}^2\varphi_\mathrm{y}(y)}{\mathrm{d}y^2}\varphi_\mathrm{z}(z) + \varphi_\mathrm{x}(x)\,\varphi_\mathrm{y}(y)\,\frac{\mathrm{d}^2\varphi_\mathrm{z}(z)}{\mathrm{d}z^2}.$$

By using an expansion such as (3.20) in each dimension, $\varphi(x,y,z)$ can be solved for by calculating

$$\tilde{\varphi}_{i,j,k} = \epsilon_0^{-1} \left\{ \left[\frac{\pi}{L_\mathrm{x}}\,(i+1)\right]^2 + \left[\frac{\pi}{L_\mathrm{y}}\,(j+1)\right]^2 + \left[\frac{\pi}{L_\mathrm{z}}\,(k+1)\right]^2 \right\}^{-1} \tilde{\rho}_{i,j,k}. \tag{3.21}$$

The algorithm solves Poisson's equation by first calculating the Fourier transform of the charge density $\tilde{\rho}_{i,j,k}$. Then, the Fourier coefficients of the potential $\tilde{\varphi}_{i,j,k}$ are found from (3.21). By using the inverse transform, the potential $\varphi_{i,j,k}$ can be calculated.

A direct calculation of the Fourier transform (3.20) would require $\mathcal{O}\big(N^2\big)$ operations. However, Fast Fourier transforms exist, which calculate the transform in $\mathcal{O}(N \log N)$ by recursively reusing previously computed values [31]. The implementation in *bender* uses the distributed-memory version of the FFTW library [32]. This version of the

Boundary condition	Transform / Inv. transform		
$\varphi(x)\,\vert_{x=0} = \varphi(x)\,\vert_{x=L} = 0$	$\tilde{\varphi}_k = 2\sum_{j=0}^{N-1} \varphi_j \sin\left(\pi\,[k+1]\,\frac{x_j}{L}\right)$	$\frac{x_j}{L} = \frac{j+1}{N+1}$	(DST-I)
$\varphi(x)\,\vert_{x=0} = 0$ $\frac{\mathrm{d}\varphi(x)}{\mathrm{d}x}\vert_{x=L} = 0$	$\tilde{\varphi}_k = \varphi_0 + 2\sum_{j=0}^{N-1} \varphi_j \cos\left(\pi\left[k+\frac{1}{2}\right]\frac{x_j}{L}\right)$		(DCT-III)
	$\varphi_j = 2\sum_{k=0}^{N-1} \tilde{\varphi}_k \cos\left(\pi\left[k+\frac{1}{2}\right]\frac{x_j}{L}\right)$	$\frac{x_j}{L} = \frac{j}{N}$	(DCT-II)
$\frac{\mathrm{d}\varphi(x)}{\mathrm{d}x}\vert_{x=0} = \frac{\mathrm{d}\varphi(x)}{\mathrm{d}x}\vert_{x=L} = 0$	$\tilde{\varphi}_k = \varphi_0 + 2\sum_{j=1}^{N-2} \varphi_j \cos\left(\pi k\frac{x_j}{L}\right) + (-1)^k\,\varphi_{N-1}$	$\frac{x_j}{L} = \frac{j}{N-1}$	(DCT-I)

Table 3.1.: Boundary conditions and respective (unnormalized) Fourier transforms used in the implementation of the Fast Fourier solver. DST-I and DCT-I are their own inverse transforms.

library can calculate the required Fourier transforms while distributing the data along one direction among multiple processes. The solver supports either zero potential (Dirichlet) or zero electric field (Neumann) boundary conditions for each of the six surfaces of the computational domain. The transforms used as well as the corresponding multiplication factors are listed in Table 3.1.

Similar to the finite difference solver, the charge density is calculated using trilinear interpolation. The electric fields are calculated from the potentials using a second-order accurate finite difference approximation and interpolated linearly to the particle position inside each cell,

$$E_j^x = \frac{\varphi_{j+1} - \varphi_{j-1}}{2\Delta x}, E_0^x = \begin{cases} \frac{4\varphi_1 - \varphi_2}{2\Delta x} & \text{Dirichlet} \\ 0 & \text{Neumann} \end{cases} \text{ and } E_{N-1}^x = \begin{cases} \frac{\varphi_{N-2} - 4\varphi_{N-1}}{2\Delta x} & \text{Dirichlet} \\ 0 & \text{Neumann} \end{cases}.$$

R-Z poisson solver

In Low-Energy Beam Transport scenarios involving solenoid magnets, cylindrical symmetry is often kept approximately. In this case, the calculation can be sped up significantly by using a two-dimensional Poisson solver. Reducing the dimensionality not only reduces the number of grid points, but also the number of particles required to reproduce the charge densities.

A radially symmetric solver was implemented using the finite difference scheme given in [33] for equidistantly spaced meshes,

$$-\frac{\rho_{j,k}}{\epsilon_0} = \frac{2j+1}{2\Delta r^2}\varphi_{j+1,k} - 2\frac{j}{\Delta r^2}\varphi_{j,k} + \frac{2j-1}{2\Delta r^2}\varphi_{j-1,k} + \frac{1}{\Delta z^2}\left(\varphi_{j,k+1} - 2\varphi_{j,k} + \varphi_{j,k-1}\right).$$

The solver supports Neumann boundaries in longitudinal direction using the same scheme as the three-dimensional solver. The grid can be distributed among multiple processors along the z-direction. Solution of the linear system is again implemented using PetSc [29], where LU decomposition is the default solution algorithm.

For charge accumulation, area weighting is used. Compared to linear weighting, the contribution of a particle is not distributed according to the relative position of the particle within the cell but relative to the enclosed area,

$$Q_j = \frac{r_{j+1}^2 - r^2}{r_{j+1}^2 - r_j^2} \cdot Q, \quad Q_{j+1} = \frac{r^2 - r_j^2}{r_{j+1}^2 - r_j^2} \cdot Q. \tag{3.22}$$

Linear weighting is used in longitudinal direction. To calculate charge densities, the contributions at the grid points (i, j) are divided by the cell volumes $V_{i,j}$. As proposed in [34], the volumes $V_{i,j}$ are calculated by weighting the volume elements in the same way as the particles,

$$\begin{aligned} V_{i,j} &= \int W_j(\vec{r}) \, \mathrm{d}V \\ &= 2\pi\Delta z \left(\int_{r_{j-1}}^{r_j} r \frac{r_{j+1}^2 - r^2}{r_{j+1}^2 - r_j^2} \mathrm{d}r + \int_{r_j}^{r_{j+1}} r \frac{r^2 - r_{j-1}^2}{r_j^2 - r_{j-1}^2} \mathrm{d}r \right) \\ &= \frac{\pi}{2} \Delta z \left(r_{j+1}^2 - r_{j-1}^2 \right) = 2\pi\Delta z \Delta r^2 j, \end{aligned}$$

where the last step is only valid for a regular lattice $r_j = j\Delta r$ and $W_j(\mathbf{r})$ is the particle shape function corresponding to the choice in (3.22). For the inner- and outermost cells in radial direction, the volumes are obtained by dropping the out-of-bounds integrals. The results are $V_{i,0} = \frac{1}{2}\pi\Delta z\Delta r^2$ and $V_{i,N_r} = \frac{2N-3}{2}\pi\Delta z\Delta r^2$.

Parallelization

The computation for all of the solvers presented above can be distributed among multiple processors. Both the Fast Fourier and the RZ solver support distribution in z, while the three-dimensional finite difference solver allows arbitrary blocks inside the global grid to be distributed. The communication during the solution process is handled by the specific libraries, but communication is still required for the charge accumulation step and the calculation of the electric field.

Without any load balancing, *bender* keeps particles in the same process they were inserted on. Consequently, in this mode of operation, particles can be located anywhere on the grid and are not necessarily contained within the local portion of the grid. Since it is much more likely for a particle to be located completely inside the grid volume on one processor than between two or multiple grid portions, sending the particle position (in units relative to the grid to avoid recomputation) instead of the charge contribution to the individual grid points is more efficient. Particles located in the cells between two grid portions, then have to be sent to both processors. Synchronous communication is used

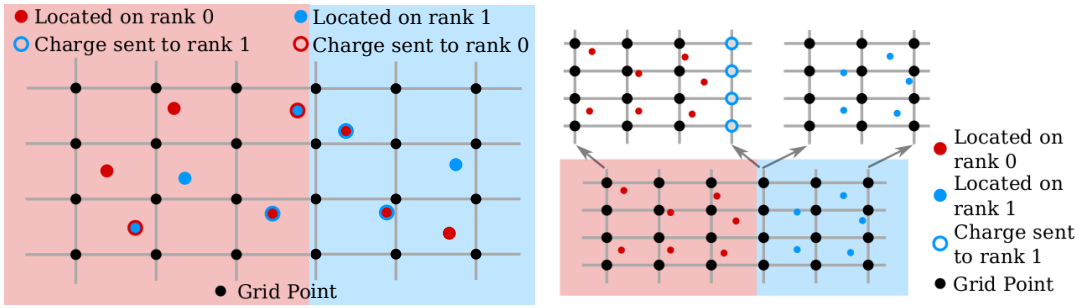

(a) "Non-local" mode. (b) "Local" mode.

Figure 3.7.: Charge accumulation in multiprocessor runs.

for sending particles, i.e. the code first iterates over all particles, storing those that have to be sent to other processors and then sends these collectively.

During the accumulation of the electric field values at the particle positions, all non-local particle positions are synchronously sent to the corresponding processors. These then answer the requests by sending a list of electric field values at the requested positions.

When the particle distribution in the computational domain is approximately homogeneous, it is much more efficient to keep particles local to the grid. When the load leveling provided by the solver implementations is used, only particles in the grid cells between grid portions can contribute to the charge density accumulated at another process. In this mode, the charge density array is expanded at each processor interface, so that the usual charge accumulation routine treats all particles like local particles. Afterwards, the charge density on the interfaces is sent to the adjacent processor and added. Additionally, in local mode, the solvers share the values of the potential in the affected regions after the solution. This allows calculating the electric field for all particles without requiring any further communication among processors.

Figure 3.7 shows the two possible ways charge density accumulation is treated.

Tests

The solvers were tested for a number of distributions, for which expressions for the electric field and the potential can be found. Figure 3.8 contains some results for a charged sphere and a cylinder, both with a Gaussian distribution in the radius r,

$$\rho(r) = \rho_0 \exp\left(-\frac{r^2}{2\sigma^2}\right). \tag{3.23}$$

For the numerical computation, the distributions have to be cut off due to the finite grid size. For the test a grid with $d = 1\,\mathrm{m}$ was used. Using $\sigma = 5\,\mathrm{cm}$, a comparison to the solution of the infinitely extended distribution is valid, since the fraction of charge located outside of the lattice volume is extremely small. Such a comparison is given in Figure 3.8.

For the tests, the charge distribution was calculated from (3.23) and not sampled using a large number of particles to avoid contributions from statistical error.

$$E_\mathrm{r}(\mathrm{r}) = (2\pi)^{-\frac{3}{2}} \frac{Q}{\epsilon_0} \frac{1}{r^2} \left[\sqrt{\frac{\pi}{2}} \mathrm{erf}\left(\frac{r}{\sqrt{2}\sigma} \right) - \frac{r}{\sigma} \exp\left(-\frac{r^2}{2\sigma^2} \right) \right]$$

$$E_\mathrm{r}(\mathrm{r}) = -\frac{1}{2\pi\epsilon_0} \frac{I}{v} \frac{1}{r} \left[\exp\left(-\frac{r^2}{2\sigma^2} \right) - 1 \right]$$

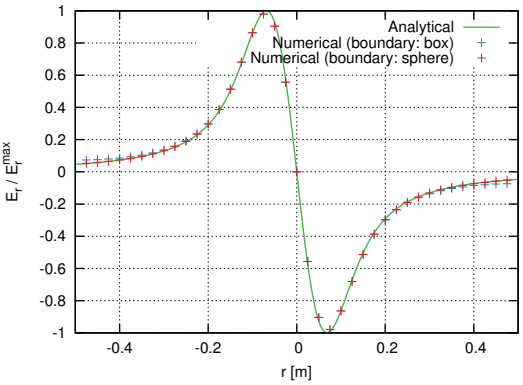

(a) Radial electric field.

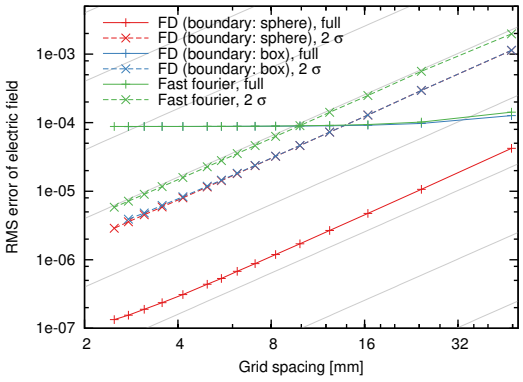

(b) Error for different grid spacings.

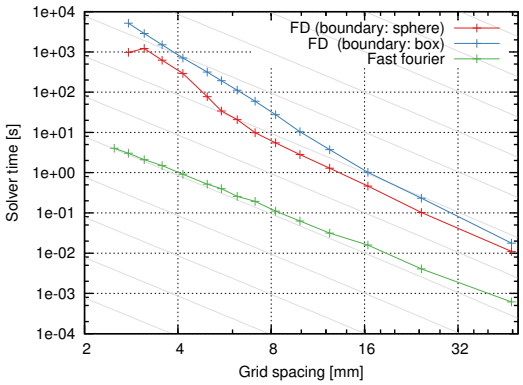

(c) Solution time for different grid spacings.

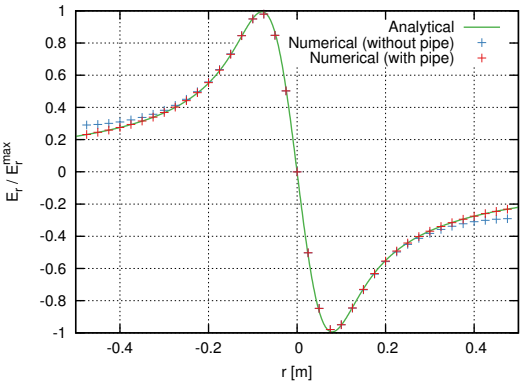

(d) Radial electric field.

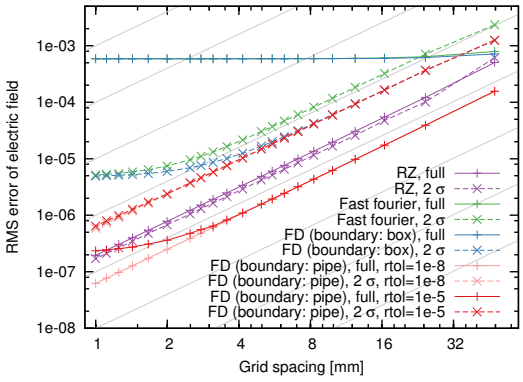

(e) Error for different grid spacings.

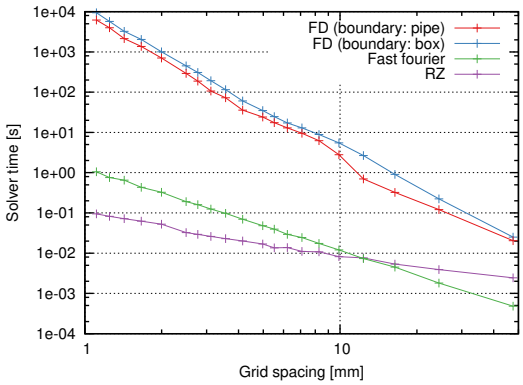

(f) Solution time for different grid spacings.

Figure 3.8.: Test of the Poisson solvers using a Gaussian distributed sphere (left) and a Gaussian distributed cylinder (right), $\sigma = 5\,\mathrm{cm}$ on a grid of $d = 1\,\mathrm{m}$.

For the charged sphere, Dirichlet boundary conditions $\varphi(r) = 0$ were used on all faces of the grid box. An additional calculation was made using the finite difference (FD) solver, including a grounded sphere of 50 cm radius. For the cylinder, Neumann boundary conditions $\mathrm{d}\varphi/\mathrm{d}z = 0$ were used longitudinally for all solvers and Dirichlet boundary conditions transversely. For the Fast Fourier (FFT) solver, these are rectangular, while for the rz solver the boundary is a cylinder. The finite difference solver allows calculation of both cases.

Rectangular boundary conditions introduce an artificial octupolar component, i.e. the field is higher along the coordinate axes and lower along the diagonals of the grid. The effect can be seen in Figure 3.8a and d, where E_r was calculated along the coordinate axis.

For different grid resolutions, Figure 3.8b and e contain the root-mean-square deviation in the electric field calculated over the complete grid and as well as over a volume of 2σ around the center. Due to the systematic error produced by the boundary conditions, when using higher resolutions, the deviation over all grid points does not decrease significantly for the FFT solver and the FD solver without the appropriate boundaries. When these are included, the deviation decreases quadratically over the simulated range. The FD solver uses the GMRES algorithm with incomplete LU preconditioning [29] per default, which is aborted when the norm of the residual $||\rho - A\varphi||_2$ falls below a certain value (per default, $\mathrm{rtol} \cdot ||\rho||_2$, $\mathrm{rtol} = 10^{-5}$). For higher resolutions, this value is reached before the deviation is sufficiently reduced, which leads to the visible divergence from quadratic convergence. For $\mathrm{rtol} = 10^{-8}$, as is shown in Figure 3.8e, the rms deviation continues to decrease.

Looking at the points within 2σ, the deviation decreases quadratically for all solvers. For the cases with incorrect boundary conditions however, once a certain value is reached, there is no further improvement.

Figure 3.8c and f contain the times required for solving for the potential. If possible and especially for high resolution calculations, using the rz solver is faster than the FFT solver, mainly due to the greatly reduced number of degrees of freedom.

In general, for calculations in 3d, the FFT solver can be up to a factor of 1000 times faster. However, the values have to be taken with a grain of salt: in a particle-in-cell application, the FD solver reuses the potential values from the previous step as a starting point whereas the FFT solver—as a direct method—always requires the same number of operations for the solution. In cases where the changes in charge density are low, the FD solver converges much faster than shown in the figures.

3.2.3. Structure of the code

bender is implemented using the C++ language. Linear algebra routines are provided by the Armadillo library [35]. The code uses the Message Passing Interface (MPI) via the Boost.MPI library [36] for communication among processes. Figure 3.9 provides an overview of the class structure of the code.

The `Species` class contains the data for macroparticles of equal charge and mass. The positions and the momenta in the laboratory frame are stored together with an index

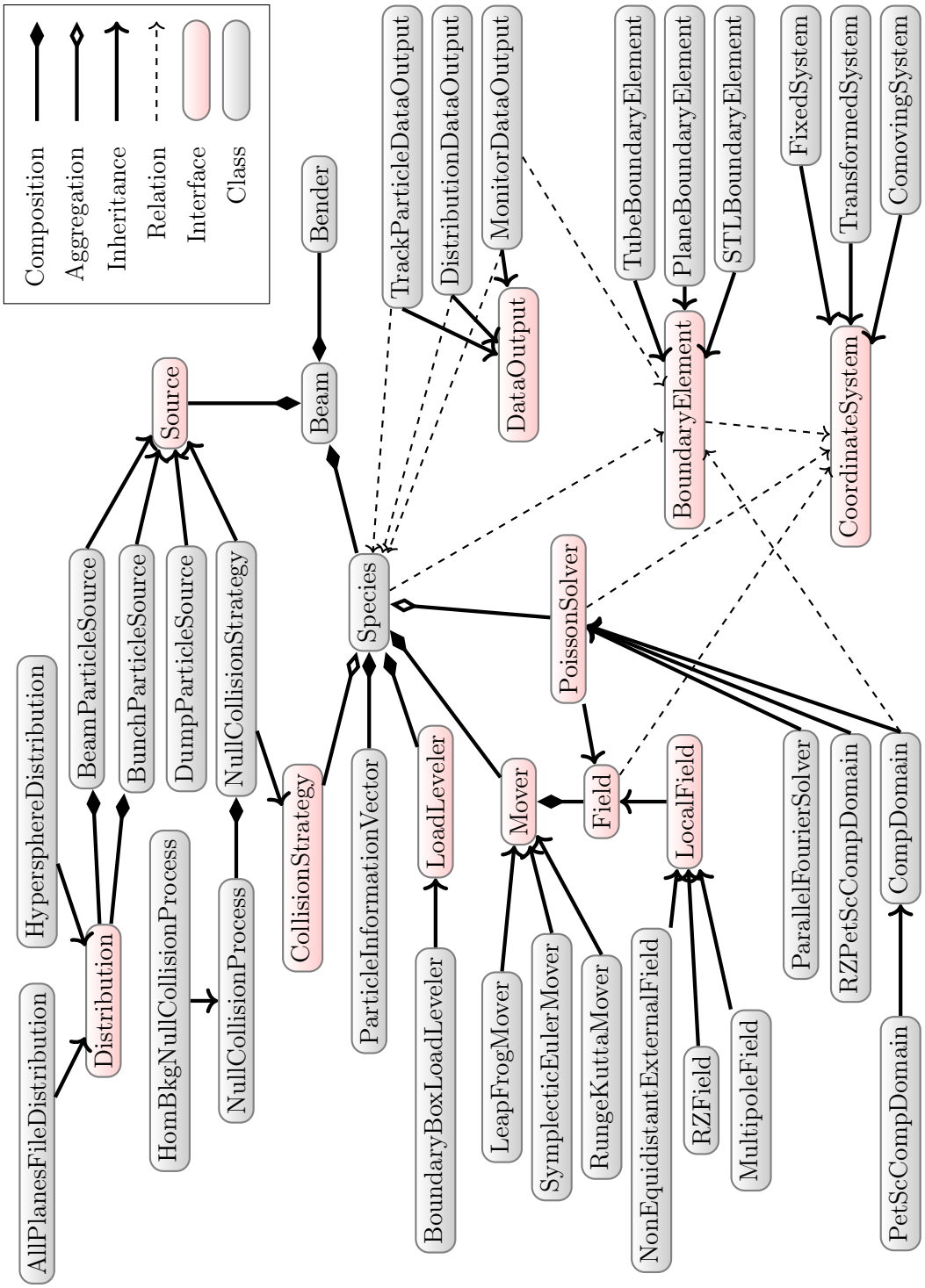

Figure 3.9.: Structure of the code *bender*.

unique for each particle as well as the macroparticle's real particle count, which is required in the charge accumulation step. The index can be used to track particles, since various operations such as particle losses may change the order of the storage array. Additionally the class contains routines for filtering particles against elements bounding the simulation implemented via the `BoundaryElement` interface, which can be used either for particle losses i.e. for removing particles or for monitoring.

If required, any other part of the code may request additional per particle storage contained in `ParticleInformationVector`, which is updated along with the regular particle array. This feature is used by some of the mover algorithms to avoid recalculation of quantities between timesteps.

Particles can be inserted into the simulation via particle sources derived from the `ParticleSource` class. The `BunchParticleSource` inserts a fixed number N of particles into the simulation once. These consist of $N_{\text{macro}} = I/\left(f_{\text{rf}} N q_{\text{species}}\right)$ real particles, where I is the beam current, f_{rf} a given rf frequency and q_{species} the particle charge of the corresponding species. The `BeamParticleSource` builds a continuous beam by inserting N particles with $N_{\text{macro}} = I\Delta t/\left(q_{\text{species}} N\right)$, where Δt is the time step of the simulation. The `DumpParticleSource` can be used to restart a simulation using an exported particle distribution from a previous simulation.

For `BunchParticleSource` and `BeamParticleSource` the distribution in phase space can be specified by using one of the specializations of the `Distribution` interface. These can be either read from file in various formats or, for continuous beams, generated from a number of model distributions.

The equation of motion for particles are integrated using the various implementations of the `Mover` class. The algorithm used is described in Section 3.2.1. As input, it uses a list of objects implementing the `Field` interface to calculate electric and magnetic fields. In the current version, the code treats external fields in the same way as the space charge fields.

In general, for multi-processor runs, *bender* does not assume particles to be local to the fields. Theoretically, field maps could be located on another process than the particles. To avoid long waiting times until requests for the field contribution to a foreign process have been answered, the Accumulate method of the `Field` class calculates all field values for a given list of positions at once. This enables the implementations to continue calculating values at local positions while waiting for requests to other processors to be answered.

However, even for the very large field maps used in the simulations in Chapter 5, keeping a copy available in every process was still possible and the cost of increased communication from keeping the data only one on process far outweigh the savings in memory. Thus, all currently implemented field models derive from `LocalField`, which implements Accumulate as a simple calculation loop over the list of positions. Among the implemented field models are a Biot-Savart solver used in Section 5.1 and simple multipole fields.

The only parallel-aware `Field` implementations are the solvers for Poisson's equation, since these only hold a local portion of the grid on each processor. Apart from operations such as charge accumulation, solving for the potential and accumulation of electric field values, the `PoissonSolver` class provides a common interface for setting

boundary conditions. Two of the implemented solvers—the three-dimensional Cartesian and cylindrical finite difference solvers—support using objects of the `BoundaryElement` class to define these. The `CompDomain` solver assigns an index to each surface to allow boundary conditions to be set.

The code uses a concept termed "coordinate systems" implemented via the specializations of the `CoordinateSystem` class to transform various objects in the simulation. Implementation for simple translations (`FixedSystem`) as well as general affine transformations (e.g. rotations, scaling and shears) implemented in `TransformedSystem` are provided. The class `ComovingSystem` provides a transformation into a system which is pinned to the center of mass or charge of a particle distribution and aligned to its direction of movement. This allows the use of the available solvers for Poisson's equation in a comoving frame without any additional code. Currently, only Galileo transformations, i.e. non-relativistic transformations, are supported.

For objects such as the `BoundaryElement`, `ParticleSource` and `LoadLeveler` classes, wrappers exist that transform all positions in calls to these objects as well as their results using `CoordinateSystem`. `Field` also provides support for these coordinate systems. This allows flexibly placing these objects in the simulation space without reimplementing support in every class.

Various classes deriving from the `DataOutput` class implement routines for analysis and for exporting data from the simulation. Objects of these classes are triggered in a list of steps given by the user. Currently implemented are output of a list of particles either at a given time or when they intersect given geometric objects, output of particle losses, tracking, output of the potential, electric and magnetic fields used in the simulation and calculation of various parameters such as kinetic or potential energy of all particles.

The contents of a simulation are specified in an XML-type format, which closely follows the class hierarchy. This input file is read by the `Bender` class, which also contains the main particle-in-cell loop.

3.3. The 2d code *tralitrala*

When effects such as space charge compensation or time-dependent external fields are not present or their detailed description is not of interest, beam matching simulations of dc beams can usually be performed using a much simpler code. During the work for this thesis, such a code, named *tralitrala*, was written.

Instead of time, as is conventional in accelerator physics, the reference path length s is used as independent variable. The software calculates the particle motion in the transverse plane, using x, x' and y, y'. When x' and y' are small, the paraxial approximation can be used. This makes it possible to use transfer matrices [37, p. 120ff]. *tralitrala* includes matrices for drift sections, quadrupole magnets, dipoles with edge focusing and thin lenses. For solenoids, the code includes an integrator of the paraxial equation of motion [17, p. 65] in fields imported from other simulation software. The algorithm used is similar to the one in Section 3.2.1.

Space charge can be included. The code features a 2d solver in a rectangular geometry

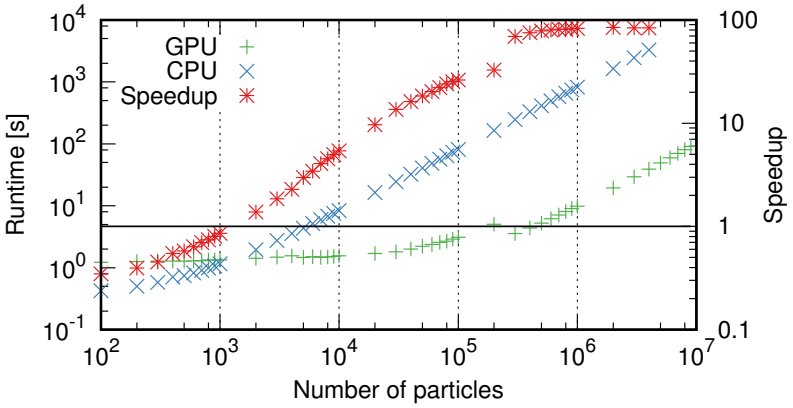

Figure 3.10.: Comparison of the simulation times for a simulation of the FRANZ LEBT (Section 5.2.2) using the CPU or the graphics card version of *tralitrala*[1] depending on the number of particles. A grid of 512 points was used. Simulation times were averaged over five runs.

using the algorithm described in Section 3.2.2 and a radial solver using the trapezoidal rule to integrate

$$E_\mathrm{r}(r) = -\frac{1}{r}\frac{1}{\epsilon_0}\int_0^r \mathrm{d}r' r' \rho(r') \,. \tag{3.24}$$

The kick by the electric field

$$M_{\mathrm{sc,x}}(\Delta s) = \begin{pmatrix} 1 & 0 \\ E_x \Delta s/(E\rho) & 1 \end{pmatrix},$$

where $(E\rho) = 2E/q$ is the electric rigidity of a particle with energy E, is included by applying

$$M(\Delta s) = M_\mathrm{m}(\Delta s/2)\, M_\mathrm{sc}(\Delta s)\, M_\mathrm{m}(\Delta s/2)$$

in each step, where M_m is the matrix or the integrator for the optical element. This results in a method that is second-order accurate in Δs [38, p.47].

The code is written in C++ and can be controlled using a Python interface. The algorithms for the optical elements and the solution of equation (3.24) were also implemented for execution on graphic cards using CUDA. Most of the calculations are trivially parallel since each particle can be handled separately. Only during the calculation of the space charge density, data needs to be shared among threads. The implementation assigns the particle list in equal parts to a number of CUDA thread blocks, which then calculate the density of these particles in their shared memory using atomic adds. Finally, the results are copied to global memory and added by a single thread block. The integration of the electric field is implemented as a parallel reduction.

Figure 3.10 shows the running time of a simulation of the FRANZ LEBT (3.8 m length,

[1] On a Nvidia Geforce GTX 770, Intel Core i7-3770K.

1 mm step size). For the graphics card version, below 1×10^4 particles, the Poisson solver and various management tasks dominate the run time, which remains constant. For more than 3×10^5 particles, the run time increases linearly with the number of particles. Compared to the CPU version, the GPU version can be up to 100 times faster. This reduces run times of a couple of hours to a few minutes. This improvement allows mapping of the parameter space of a beam line. An example is given in Section 5.2.2.

3.4. Tests against self-consistent solutions

In the code tests so far, only single elements of the particle-in-cell algorithm were tested—the integration of motion and the solver for Poisson's equation—but not the code as a whole. For this purpose, model systems for which the solution can be found by simpler or even analytic means can used. In the following, two examples are presented and compared to *bender* simulations: a plasma cloud in thermal equilibrium as well as a periodic transport channel.

3.4.1. Poisson-Boltzmann equation

Derivation and numerical solution

It can be shown [39, p. 52] that any phase space distribution $f(\mathbf{r}, \mathbf{p})$ which is a function of the single particle constants of motion such as the Hamiltonian H is a solution to the steady-state Vlasov equation. In electrostatic approximation,

$$\frac{\mathbf{p}}{m} \nabla_r f(\mathbf{r}, \mathbf{p}) + q\mathbf{E} \nabla_p f(\mathbf{r}, \mathbf{p}) = 0. \tag{3.25}$$

Thus, for a group of particles of mass m and charge q trapped inside a confining potential $\varphi_{\text{ext}}(\mathbf{r})$, a Boltzmann distribution

$$f(\mathbf{r}, \mathbf{p}) = f_0 \exp\left(-\frac{H}{k_\text{b} T}\right) = f_0 \exp\left(-\frac{\mathbf{p}^2}{2mk_\text{b} T}\right) \exp\left(-\frac{q\left(\varphi_\text{c}(\mathbf{r}) + \varphi_\text{ext}(\mathbf{r})\right)}{k_\text{b} T}\right) \tag{3.26}$$

solves equation (3.25). Additionally, Poisson's equation must be fulfilled,

$$\nabla^2 \varphi_\text{c}(r) = -\frac{q}{\epsilon_0} \int f(\mathbf{r}, \mathbf{p}) \, \mathrm{d}\mathbf{p} = -\frac{\rho_\text{c}}{\epsilon_0} \exp\left(-\frac{q\varphi(\mathbf{r})}{k_\text{b} T}\right). \tag{3.27}$$

Here, $\varphi(\mathbf{r}) = \varphi_\text{c}(\mathbf{r}) + \varphi_\text{ext}(\mathbf{r})$.

This is the Poisson-Boltzmann equation, which can be used to calculate the potential and the density of such a trapped particle cloud. The total charge of the cloud ρ_c can be chosen freely. To provide a confining field in all spatial directions, the external potential has to be produced by a charge distribution ρ_ext. For the present purpose, this distribution is considered as fixed.

Sometimes, it is convenient to replace ρ_c by a compensation degree η defined as the

ratio of the cloud's charge to that of the confining charges,

$$\rho_\mathrm{c} \int \mathrm{d}V \exp\left(-\frac{q\varphi_\mathrm{c}(\mathbf{r})}{k_\mathrm{b}T}\right) = \eta \int \mathrm{d}V \rho_\mathrm{ext}(\mathbf{r})\,.$$

The Poisson-Boltzmann equation can be non-dimensionalized by scaling the potential $\tilde{\varphi} = e\varphi/\left(k_\mathrm{b}T\right)$ and by scaling the coordinates by $\lambda_\mathrm{d}^{-1} = \left(\epsilon_0 k_\mathrm{b}T/\left(n_\mathrm{c}e^2\right)\right)^{-1/2}$, where n_c is the density of the compensation particles on the axis. Thus,

$$\tilde{\nabla}^2\tilde{\varphi}_\mathrm{c} = -\mu \exp(\tilde{\varphi}_\mathrm{ext}(\tilde{\mathbf{r}}) + \tilde{\varphi}_\mathrm{c}(\tilde{\mathbf{r}}))\,. \tag{3.28}$$

Including ρ_ext, equation (3.28) for the total potential $\tilde{\varphi} = \tilde{\varphi}_\mathrm{ext} + \tilde{\varphi}_\mathrm{c}$ is

$$\tilde{\nabla}^2\tilde{\varphi} = f_\mathrm{ext}(\tilde{\mathbf{r}}) - \mu \exp(\tilde{\varphi}(\tilde{\mathbf{r}}))\,. \tag{3.29}$$

Algorithms for both equations were implemented and their convergence properties compared.

The solutions of (3.29) are fully characterized by the Debye length λ_d and the compensation degree contained within the factor

$$\mu = \eta \int \mathrm{d}V \exp(\tilde{\varphi}(\mathbf{r})) \left(\int \mathrm{d}V f_\mathrm{ext}(\mathbf{r})\right)^{-1}.$$

The potential φ will take equal shapes for a thin and cold plasma and a dense and hot plasma with equal values of λ_d.

In practice, n_c is not known beforehand, since its value depends nonlinearly on η and the temperature. For the numerical implementation, it is still beneficial to use the given nondimensionalization to keep values in the same order of magnitude. For the examples given below, the density of the confining particles at the origin was used as guess for n_c, which is a good choice for low Debye lengths.

Following the approach in [40], a dependence on a parameter t can be added to solve (3.29) numerically,

$$\frac{\mathrm{d}\tilde{\varphi}}{\mathrm{d}t} = \tilde{\nabla}^2\tilde{\varphi} - f_\mathrm{ext}(\tilde{\mathbf{r}}) + \mu \exp(\tilde{\varphi}(\tilde{\mathbf{r}})) = R(\tilde{\varphi})\,. \tag{3.30}$$

This equation is similar to the heat equation, except for the added exponential part. To solve (3.30), the Crank-Nicholson method [24, p. 1045] can be used for the linear part. For the exponential term, to avoid solving a non-linear equation in every step, a more simple Forward Euler method can be used. Using the Forward Euler method for the spatial derivative as well, i.e. using only $R(\tilde{\varphi}^n)$, was found to be unstable. Then, the following differential equation has to be solved in every iteration:

$$\left(\mathbb{1} - \frac{\Delta t}{2}\tilde{\nabla}^2\right)\tilde{\varphi}^{n+1}(\tilde{\mathbf{r}}) = \tilde{\varphi}^n(\tilde{\mathbf{r}}) + \frac{\Delta t}{2}\tilde{\nabla}^2\tilde{\varphi}^n(\tilde{\mathbf{r}}) + \Delta t\left(f_\mathrm{ext}(\tilde{\mathbf{r}}) + \mu \exp\tilde{\varphi}^n(\tilde{\mathbf{r}})\right). \tag{3.31}$$

The second derivatives can be discretized using finite differences. For the purpose

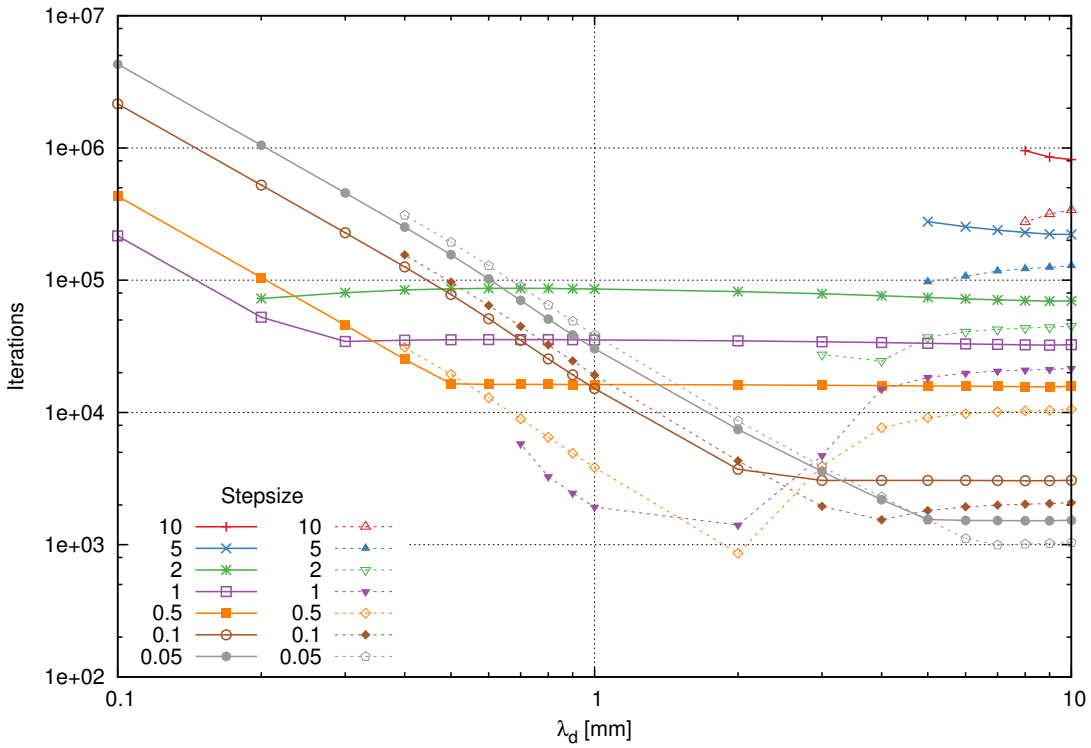

Figure 3.11.: Number of steps required by the one-dimensional implementation in cylindrical coordinates to reduce the norm of the residual $||R(\tilde{\varphi})||$ to below 10^{-6} for various step sizes and Debye lengths in a system with $\eta = 0.95$ and $R_{\text{system}} = 3\,\text{cm}$. Missing points indicate divergence of the algorithm. The dashed curves are for the version of the algorithm solving (3.28), solid curves are for the version solving (3.29).

of testing *bender*, a version for spherically symmetric systems was developed. In the iteration, the resulting tridiagonal linear system is solved using routines from LAPACK [41]. For the simulations in Section 4.4, a one-dimensional radial and a two dimensional $r - z$ version of the algorithm in cylindrical coordinates were implemented. The same discretization as in Section 3.2.2 as well as routines from the LAPACK and UMFPACK [42] libraries were used respectively.

Figure 3.11 shows the number of steps required to reduce the norm of the residual $||R(\tilde{\varphi})||$ to below 10^{-6} for both variants of the algorithm. Missing points indicate divergence of the algorithm.

In many cases, the algorithm excluding the external charge distribution is faster. Only towards lower Debye lengths and for small step sizes, the alternative version provides a small benefit. The version of the algorithm solving for the complete potential is more robust against divergence, which occurs when the parameter μ exceeds the range of a double precision variable.

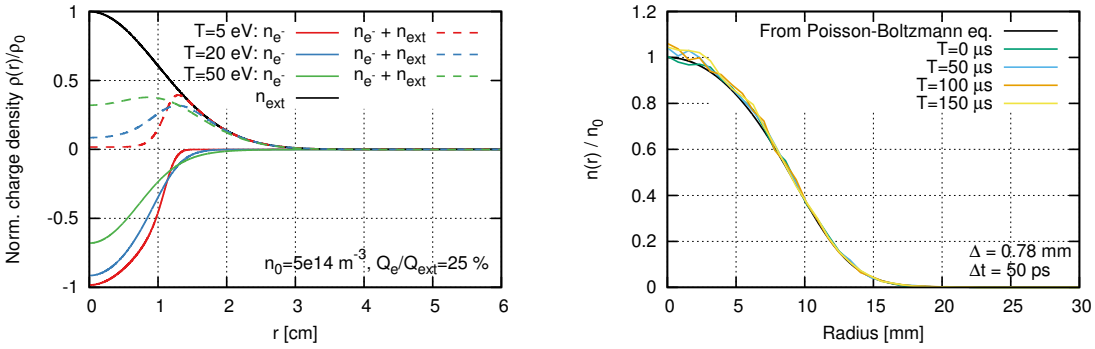

(a) Radial distribution of an electron cloud with different temperatures in the potential well of a Gaussian charge distribution.

(b) Long-term time evolution of the distribution from *bender* for a simulation with grid spacing $\Delta \approx 0.5\lambda_{d,0}$ and $\omega_{\mathrm{p},0}\Delta t \approx 0.06$.

Figure 3.12.: Code test using a thermal confined electron cloud. $T = 20\,\mathrm{eV}$ was used in the PIC simulations.

Test against *bender*

For the tests, a Gaussian charge distribution $\sigma = 1\,\mathrm{cm}$ and $n_0 = 5 \times 10^{14}\,\mathrm{m}^{-3}$ was used to confine an electron cloud. With the algorithm described in the previous section, the Poisson-Boltzmann equation was solved to calculate its radial charge density profile $\rho_e(r)$. The confining charge density as well as $\rho_e(r)$ for various temperatures are displayed in Figure 3.12a. For the $T = 20\,\mathrm{eV}$ case, particle distributions with Maxwellian speed distribution were generated following $\rho_e(r)$. Those were then loaded in *bender*.

The probability for electrons to be located far away from the confining charge density is practically zero: for example $\rho_\mathrm{e}(3\sigma) \approx 1.510^{-8}\rho_\mathrm{e}(0)$. In the tests, a grid extending to $10\sigma = 10\,\mathrm{cm}$ was used to guarantee that no particle is ever located close to the boundaries of the grid. Additionally, the systematic error in the electric field due to the incorrect boundary conditions (potential set to zero on a box instead of a sphere) should be very small in the area where particles are located, as was shown in the tests in Section 3.2.2.

The plasma parameters calculated using the density $n_{\mathrm{e},0} \approx 4.6 \times 10^{14}\,\mathrm{m}^{-3}$ at the origin are $\omega_{\mathrm{p},0} \approx 1.2\,\mathrm{GHz}$, $\lambda_{\mathrm{d},0} \approx 1.5\,\mathrm{mm}$ and $\Lambda \approx 2.2 \times 10^7$. The rms size of the cloud is $x_\mathrm{rms} \approx 5.6\,\mathrm{mm}$.

Even over long time scales, for simulations with relatively high resolution, the distribution in the *bender* simulation changes very little. An example is shown in Figure 3.12b, for a grid spacing of $\Delta \approx 0.5\lambda_{\mathrm{d},0}$ and $\omega_{\mathrm{p},0}\Delta t \approx 0.06$ after up to 3 million time steps ($T = 150\,\mu\mathrm{s}$, $\omega_{\mathrm{p},0}\Delta t \approx 180000$). Only a small oscillation in the rms size with a frequency of $983.5\,\mathrm{MHz} \approx 0.82\omega_{\mathrm{p},0}$ was found. The amplitude of this oscillation decreases with grid resolution, from $0.5\,\%x_\mathrm{rms}$ at $1.6\,\mathrm{mm} \approx \lambda_{d,0}$ grid spacing to $0.15\,\%x_\mathrm{rms}$ at $0.6\,\mathrm{mm} \approx 0.3\lambda_{d,0}$ grid spacing. Fluctuations of similar magnitude are present in the kinetic and potential energy.

However, a slow increase in the total energy of the system over time was observed. An example for relatively low-resolution simulations (at approximately $\lambda_{d,0}$ grid spacing) is

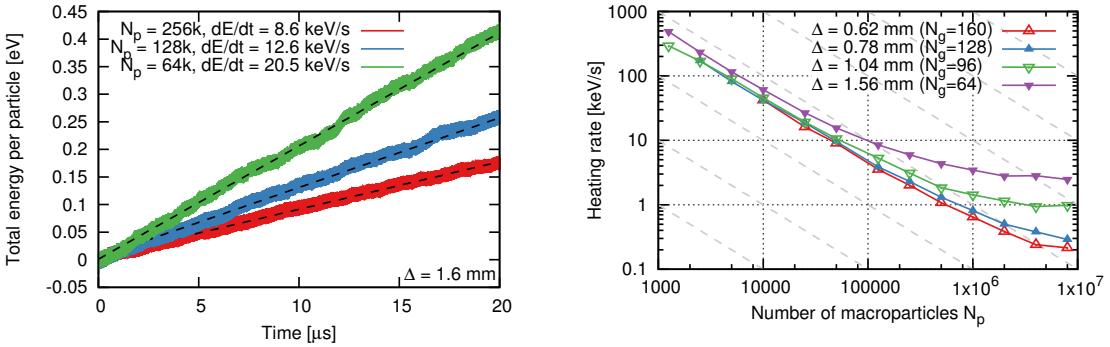

(a) Linear energy increase over time for different numbers of macroparticles.

(b) Rate of energy increase for runs with different grid resolutions and amount of macroparticles.

Figure 3.13.: Stochastic heating in the simulation of a thermal electron cloud.

shown in Figure 3.13a. The energy increases linearly with a rate that depends on the numerical parameters of the simulation. For simulations of up to 25 million steps, no change in the behaviour over time was observed, except for simulations with the lowest used resolutions. For these, a few particles were accelerated to energies high enough to leave the grid volume.

An explanation for the increase in energy is given in [21, p. 316]. The authors start with the assumption that all errors in the simulation can be included in a random "error" electric field δE. On average, this field should not accelerate particles, i.e. $\overline{\delta E} = 0$, but has a variance $\overline{\delta E^2} \neq 0$. This error field leads to a change in velocity for each particle $\delta v_i = (q/m)\delta E_i \Delta t$ in every time step Δt. Under this assumption, they calculate the average change in kinetic energy per particle ΔT between two steps resulting from this kind of field,

$$\Delta T = \overline{T_{j+1} - T_j} = \frac{1}{2} m \left(\overline{(v_i + \delta v_i)^2} - \overline{v_i^2} \right) = \frac{1}{2} m \left(2 v_i \overline{\delta v_i} + \overline{\delta v_i^2} \right) = \frac{1}{2} \frac{q^2}{m} \overline{\delta E^2} \Delta t^2. \quad (3.32)$$

Since the error occurs in every time step, the energy increases linearly. This matches the observation in the presented simulations. Simulations with different time steps also show the quadratic dependence on the timestep Δt predicted by (3.32), at least for $\Delta t > 0.2\,\mathrm{ns}$. For smaller step sizes, the heating rate stays constant.

For low numbers of macroparticles, one can assume that the error in the field is of statistical origin and $\delta E \sim 1/\sqrt{N_p}$, where N_p is the number of macroparticles. This was also found in [43, Sec. II] in a more detailed analysis for KV and Gaussian beam distributions. Then, from (3.32), $\Delta T \sim N_p^{-1}$. Figure 3.13b shows the dependence of the energy increase rate on grid spacing and macroparticle count, as well as $1/N_\mathrm{p}$ curves as grey dashed lines for comparison. The energy increase rates calculated from the simulation follow the predicted behaviour well. Depending on the grid resolution, the behaviour diverges towards higher macroparticle counts—indicating that some other, unidentified

P.	Value
W	120 keV
m	1 u
g	3.0582 T m^{-1}
σ_0	60°
σ	14.9°
β	1.63 m
α	−5.1
ϵ	25 mm mrad
I	15.77 mA
K	0.25×10^{-3}

(a) Parameters.

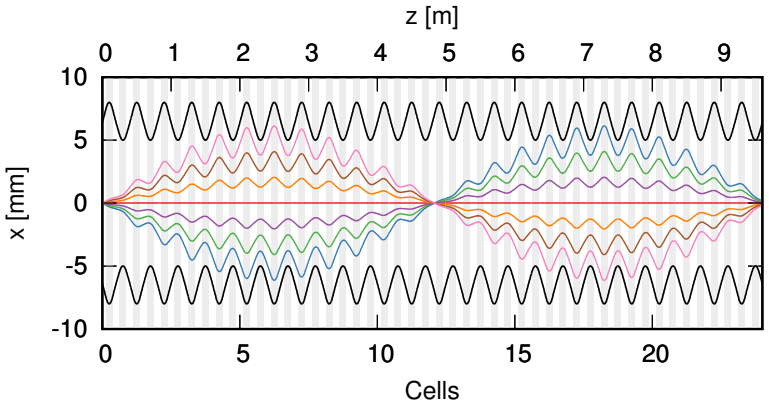

(b) Envelope and single particle tracks from the integration of (2.20).

Figure 3.14.: Parameters of the periodic transport channel used to test *bender* and *tralitrala*.

process becomes relevant as the fluctuation in the charge density becomes smaller.

By smoothing the potential (and thus the electric field), the observed heating rate can be decreased. This was done using the Fast Fourier solver (Section 3.2.2) by setting the high-frequency part of the spectrum to zero before performing the inverse transform. For 50000 macroparticles and a grid of 64^3, the heating rate decreased from 14.2 keV s^{-1} to 7.3 keV s^{-1}, when cutting off above $i^2 + j^2 + k^2 > 0.25N_g^2$. At this level of reduction however, ringing artifacts were clearly visible in the charge density. Therefore, if filtering like this were to be used, special care needs to be taken not to significantly change the charge density of interest. Smoothing the particle distribution was not further investigated in this thesis.

In retrospect, the choice of test system was not optimal. Due to the inhomogeneity of the chosen electron cloud, finding a dependence on parameters such as the Debye length of the plasma is difficult and was not performed. A better choice would have been either choosing a system with many Debye lengths contained within the electron cloud or the simulation of a periodic system.

For the beam simulations in Chapter 5, stochastical heating is likely not relevant. For example, for the simulations of the FRANZ LEBT, i.e. the transport of a 120 keV proton beam over 3.7 m, at 100 keV s^{-1}, the numerical energy increase amounts to 80 meV, corresponding to 0.8 mrad if present in one of the transverse planes. For long-term simulations, such as the beam compensation studies in Chapter 4 or for long-term tracking of beams in circular accelerators [43] however, the effect is of great importance.

3.4.2. KV envelope solution

As was described in Section 2.4, the Kapchinsky-Vladimirsky (KV) distribution is self-consistent under transport including space charge in two dimensions. For this choice of distribution, the envelope can be calculated from the KV envelope equation (2.20),

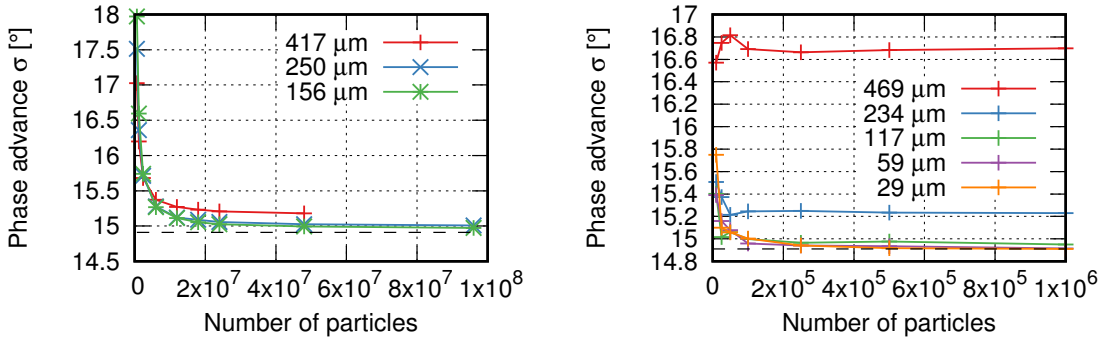

(a) *bender*. (b) *tralitrala*.

Figure 3.15.: Comparison of the phase advance calculated from simulations using different grid resolutions and number of particles. The correct value is shown as a dashed line.

which as a system of two ordinary differential equations is much simpler to solve than the Vlasov equation. To verify the correct functioning of a PIC-code, simulation results can be compared to the resulting envelope.

As a test case, a periodic focusing channel was chosen and a beam matched using the algorithm described in Section 2.4.1. The channel has a cell length of 40 cm with two quadrupole magnets of 10 cm length placed at 5 cm and 25 cm. The first focuses in x, the second in y. The parameters of the channel and the matching are summarized in Figure 3.14a. A plot of the envelope and some particle trajectories is shown in Figure 3.14b. Using a matched beam has the benefit that the envelope does not oscillate strongly and the solution is known for an arbitrarily long transport. Furthermore, results for the phase advance per cell can be compared instead of the envelopes.

Only for *tralitrala*, a full agreement can be expected. As a three-dimensional code, *bender* also includes the longitudinal coordinate and therefore the influence of the longitudinal electric field produced by the envelope oscillation of the beam. Furthermore, the integration of motion does not include the paraxial approximation and particles on the outer trajectories will fall behind those closer to the axis. Therefore, a KV distributed beam will not be perfectly self-consistent in three dimensions. Since both effects are small at the chosen parameters—$x' \approx 22$ mrad and the beam potential varying only approximately by 1 V on the axis—no differences can be expected over the short lengths calculable.

For the simulation in *bender*, 10 cells of the channel were simulated by continuously injected particles at the start of the channel. After 4 m, at the end of the simulated region, the beam is dumped. An initial beam distribution was generated from the results of the integration of the envelope equation. Without such an initial distribution, particles are accelerated forward by electric field of the forming beam. The calculations were run long enough for the initial distribution to be lost and the phase advances calculated only from newly inserted particles. For *tralitrala*, a step size of 1 mm was used. The field was

calculated using the two-dimensional FFT solver. In both cases, a 6 cm wide grid was used. For the *bender* simulation, the quarter symmetry was exploited to decrease the number of grid points and particles.

The phase advance was fitted using the algorithm described in Section 2.4.2. The results are shown in Figure 3.15. *tralitrala* reproduces the correct value 14.91°, but requires a resolution of 60 µm and more than 5×10^5 particles to reach this value. At coarser resolutions, the particle distribution showed a slight drop of the beam density at the edge. This can be explained by looking at the calculated electric field. When the edge of the beam falls within a grid cell, the electric field in this cell slightly deviates from the required radially linear behaviour.

Simulations with grid resolutions this fine would have required prohibitively long simulation times using *bender*. For the smallest grid spacing used, the result $\sigma = 14.97°$ nevertheless agrees relatively well with the expected value. Varying the longitudinal grid spacing from the 2.8 cm to 1.7 mm while keeping the number of particles per cell constant only resulted in a difference of 0.14°. For the simulations in Figure 3.15a, a spacing of 3.5 mm was used. This result legitimizes using a coarser resolution in the propagation direction for simulation of continuous beams, unless effects in this direction are specifically of interest.

4. Simulation of space charge compensated systems

This chapter covers the studies on space charge compensation using *bender*.

Even though the processes involved in the compensation of negative ion beams—the most important example being H^- beams often used in high-intensity proton machines—are similar to the positive case, only the compensation of positive ion beams will be considered. The studies were further limited to the case of proton beams. However, using the same approach, calculations for different beams could be performed as long as cross section data for the relevant processes is available.

The chapter starts with a short overview over commonly used measurement methods and general definitions. In Section 4.2, sources of compensation electrons as well as the simulation model will be discussed. Results are presented in Section 4.3 and compared with predictions from a simpler model in Section 4.4.

4.1. Space charge compensation

4.1.1. Measurements

Commonly, in low-energy beam transport lines, Faraday cups and slit-grid emittance scanners are used as diagnostics to provide information about the beam. Faraday cups measure the beam current by capturing the entire beam with a geometry usually designed to minimize the deposited beam power density. Most designs include either an electrostatic repeller or a magnetic dipole field to prohibit secondary electrons produced on the surface from leaving the cup, which would alter the current measurement. Slit-grid emittance scanners consist of a slit with an array of wires positioned at some distance, which are moved transversely through the beam. The slit cuts out a slice of the beam which drifts onto the wires and registers as current. From the current measurements, the beam distribution in one plane and thus the emittance can be calculated.

Both methods are destructive and influence the compensation state, either by allowing secondary electrons to escape into the beam (emittance scanner) or by introducing the repeller fields. Therefore, for diagnostics of a compensated beam, non-destructive methods are preferable. One option currently under investigation at IAP is tomography [44], which reconstructs the density from images taken around the beam.

To gather information on the state of compensation, diagnostics from plasma physics such as Langmuir probes have been used, for example in [8]. In a plasma, the remaining potential, the density and the electron temperature can be deduced from the measured

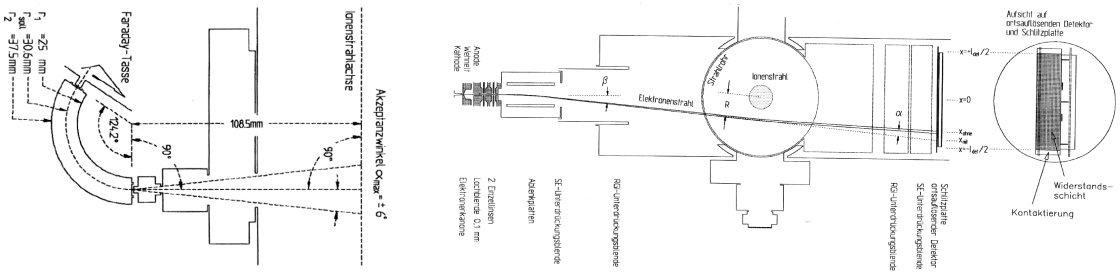

(a) 127° residual gas ion energy spectrometer.

(b) Electron beam probe for potential measurement.

Figure 4.1.: Non-interceptive beam diagnostics. Images taken from [45].

current-voltage characteristic. For measurements on beams, [45, p. 145] lists various difficulties that limit the applicability of the method.

When the beam has cylindrical symmetry, the beam potential can be deduced from a measurement of the deflection of a low current electron beam. As long as the current is low enough, the method does not significantly disturb the system. A possible setup is shown in Figure 4.1b.

Residual gas ions are a good probe for the potential. They start with low initial energies and are accelerated from the system (nearly) interaction-free. Thus, at the walls, their energy only comes from the potential at the point of ionization. For an energy-resolved measurement, an electrostatic spectrometer such as the one shown in Figure 4.1a can be used. In the deliberately decompensated case, the beam distribution can be deduced from such a measurement.

When the results of two measurements are combined, the density of all beam components can be reconstructed in the compensated case. This is possible by combining a measurement of the beam profile (for example via a backtracked measured distribution) with the measurement from an electron probe or from a residual gas ion spectrometer [45, p. 132ff].

Measuring the energy distribution of the compensation electrons is difficult, even when a Maxwell-Boltzmann is assumed. In [45], an RF probe connected to a network analyzer was used to measure the response of the electrons to an excitation. From the Q factor (i.e. the damping of the oscillation), an upper limit of the electron temperature was deduced. Another option are Langmuir probe measurements [8]. Temperatures could also be measured optically: for example, in [13], the ratio of two optical emission lines was used to measure the electron temperature in a Gabor lens.

Figure 4.2 shows two exemplary results of measurements taken from [46]. These were performed at a two-solenoid beam line containing various devices for diagnostics as well as six electrodes to confine or extract electrons. The residual gas ion spectrum in Figure 4.2a shows the influence of an electrode located approximately 40 cm downstream of the spectrometer. Much larger ion energies at positive bias indicate a global decompensation. This demonstrates that a local perturbation of the compensation state can have a far-reaching influence.

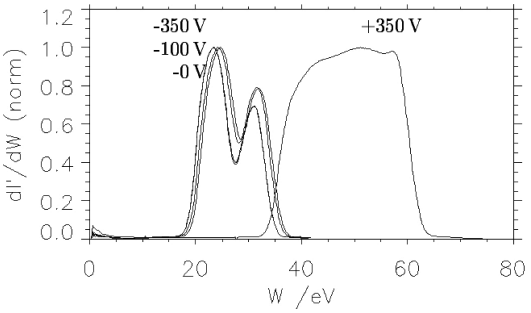

(a) Residual gas ion energy measurement.

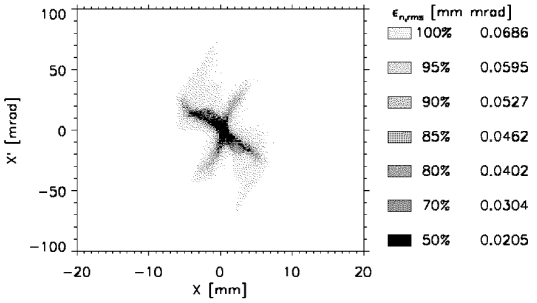

(b) Emittance measurement after a compensated beam line in a configuration similar to an injector of an accelerator.

Figure 4.2.: Two measurement results from [46, Fig. 4.31, Fig. 4.22].

The beam distribution displayed in Figure 4.2b is a measurement taken when the system was configured to produce a focused beam in a configuration similar to that of an injector for an accelerator. A compensated state was allowed to form by terminating the system with a repeller electrode on $-200\,\mathrm{V}$. The distribution is similar to that of two beams—one focused and one defocused. The appearance of this "satellite beam" was interpreted as a consequence from the additional focusing resulting from an accumulation of compensation electrons on the axis of the solenoids. Therefore, the local distribution of compensation particles can strongly influence the behaviour of the beam.

One motivation for simulating the compensation process is an improved understanding and, if unwanted, the mitigation of these effects.

4.1.2. Compensation degree

The most simple model for the compensation process used in modeling LEBTs assumes a constant reduction of the space charge forces by introducing a compensation degree η. The factor linearly reduces the perveance of the beam $K = (1-\eta)K_0$ (as defined in (2.18)) and thus also the focusing required. Values around 90 % are typically used based on experimental experience or as input from some more elaborate code (examples in [47, 11]). This degree is sometimes chosen to vary longitudinally or over time.

In the following, three definitions of a space charge compensation factor will be used. These capture different aspects of the compensation process. As a measure of the electron charge,

$$\eta_{\mathrm{part}}(z) = \frac{\lambda_{e^-}(z)}{\lambda_{\mathrm{beam}}(z) + \lambda_{\mathrm{rgi}}(z)} = \frac{\lambda_{e^-}(z)}{I/v_{\mathrm{b}} + \lambda_{\mathrm{rgi}}(z)}, \tag{4.1}$$

where the λ are the line charge densities of the various particle species. In cases where the electron density is not proportional to the beam density, the quantity can be misleading. As a worst case example, if all electrons were located outside the beam's radius, $\eta_{\mathrm{part}} > 0$, but there is no force reduction inside the beam. However, η_{part} can be useful as an input for theoretical models.

Since $\varphi(r) = \int_R^r E_\mathrm{r}(r')\,\mathrm{d}r'$,

$$\eta(r) = 1 - \frac{\varphi(r) - \varphi(0)}{\varphi_\mathrm{uncomp}(r) - \varphi_\mathrm{uncomp}(0)} \tag{4.2}$$

is proportional to the remaining electric force below radius r. In the following either $\eta_\mathrm{beam} = \eta(R_\mathrm{beam})$ or $\eta_\mathrm{pot} = \eta(R_\mathrm{wall})$ will be given.

The choice of "uncompensated" potential φ_uncomp is ambiguous since the beam extension can change due to the compensation. Both the potential of a beam transported without electrons or the potential of the beam particles are a valid choice. The former better fits an intuitive interpretation of "compensation degree", but predicts compensation in cases where none is present[1]. Thus, φ_uncomp was calculated from the beam distribution taken from the compensated simulation without any secondary particles.

When the only source of electrons is ionization of a residual gas, the electron density will change with

$$\frac{\mathrm{d}n}{\mathrm{d}t} = n_\mathrm{b} n_\mathrm{g} \sigma v_\mathrm{b} - \left(\frac{\mathrm{d}n}{\mathrm{d}t}\right)_\mathrm{loss}. \tag{4.3}$$

The density of the background gas n_g can be calculated from the equation of state of an ideal gas. n_b and v_b are the beam density and velocity respectively. Assuming the absence of particle losses and processes such as recombination, the time to reach full compensation is

$$\tau_\mathrm{scc} = \frac{1}{n_\mathrm{g}\sigma v_\mathrm{b}} = \frac{I}{v_\mathrm{b} e}\left(\frac{W}{L}\right)^{-1} = \frac{kT}{v_\mathrm{b} p \sigma}, \tag{4.4}$$

where

$$P_{p^+} = \frac{W}{L} = \frac{Ip\sigma}{kT} \tag{4.5}$$

is the rate of ionization inside a beam of current I per length L.

In low-energy beam transport sections of high-intensity linacs, the residual gas pressure ranges from 1×10^{-4} mbar to 1×10^{-8} mbar. At these values, the gas is in a molecular flow regime, i.e. the mean free path is larger than the characteristic length of the system and particles collide mostly with the walls. The density of the gas molecules for these values are almost always larger than the density of the beam. For example, a 100 mA, 120 keV proton beam with 1 cm beam radius has the same density as an ideal gas with 1.7×10^{-8} mbar at room temperature. At higher pressures, due to the large difference in the number of particles, it can be assumed that the impact of the beam on the gas is low. Whether this is true at lower pressures is difficult to ascertain.

[1] A simple example would be a system with two sections, one either fully neutralized or fully decompensated, one fully decompensated. If the beam has a larger radius in the second section when neutralization is permitted in the first section, $\eta(r)$ would be larger than 0 just from the change in beam radius.

4.1.3. Estimation of the residual gas ion background

Residual gas ions are accelerated outwards radially by the electric field of the beam. Depending on the transit time, a background of ions will form. The time for a positively charged particle of mass m and charge q to move from an initial radius r_0 to r in a homogeneous beam of current I and velocity v_b is given by

$$T(r_0, r) = \pi \sqrt{\epsilon_0 \frac{m}{q} \frac{v_\mathrm{b}}{I}} \begin{cases} r_0 \mathrm{erfi}\left(\sqrt{\ln\left(\frac{r}{r_0}\right)}\right) & \text{if } r_0 > R_\mathrm{b} \\ R_\mathrm{b}\sqrt{\frac{2}{\pi}}\cosh^{-1}\left(\frac{R_\mathrm{b}}{r_0}\right) + R_\mathrm{b}\exp\left(\frac{1}{2}\left(\frac{r_0^2}{R_\mathrm{b}^2} - 1\right)\right) & \text{if } r_0 < R_\mathrm{b},\ r > R_\mathrm{b} \\ \quad \cdot \left[\mathrm{erfi}\left(\sqrt{\frac{1}{2}\left(1 - \frac{r_0^2}{R_\mathrm{b}^2}\right) + \ln\left(\frac{r}{R_\mathrm{b}}\right)}\right) - \mathrm{erfi}\left(\sqrt{\frac{1}{2}\left(1 - \frac{r_0^2}{R_\mathrm{b}^2}\right)}\right)\right] & \\ R_\mathrm{b}\sqrt{\frac{2}{\pi}}\cosh^{-1}\left(\frac{r}{r_0}\right) & \text{if } r_0 < r < R_\mathrm{b} \end{cases} \tag{4.6}$$

R_b is the beam size and $\mathrm{erfi}(x) = -i\mathrm{erf}(ix)$ the imaginary error function. Space charge compensation can be included by scaling the current $I \to (1-\eta)I$. $T(r_0, r)$ is not necessarily monotonically increasing. For small beam radii, it is possible for ions created inside the beam to overtake those created at the edge.

Neglecting the effects of the charge of the residual gas ions, it is possible to estimate the amount of ions remaining. At radius R,

$$\lambda_\mathrm{rgi}(R) = 2\pi \int_0^R \frac{\mathrm{d}\rho_\mathrm{rgi}}{\mathrm{d}t} T(r_0, r)\, r_0 \mathrm{d}r_0 = \frac{2}{R_\mathrm{b}^2}\frac{Ip\sigma}{kT}\int_0^R T(r_0, r)\, r_0 \mathrm{d}r_0. \tag{4.7}$$

Thus the line charge from residual gas ions contained within the beam is

$$\lambda_\mathrm{rgi}(R_\mathrm{b}) = \frac{2}{R_\mathrm{b}}\frac{Ip\sigma}{kT}\sqrt{\frac{m}{q}\frac{2\pi\epsilon_0 v_\mathrm{b}}{(1-\eta)\, I}}\int_0^{R_\mathrm{b}} \cosh^{-1}\left(\frac{R_\mathrm{b}}{r_0}\right) r_0 \mathrm{d}r_0 = \frac{p\sigma}{kT} R_\mathrm{b}\sqrt{\frac{m}{q}\frac{2\pi\epsilon_0 v_\mathrm{b}}{(1-\eta)}} I. \tag{4.8}$$

Lighter particles are more easily accelerated by the electric field, reducing the ion background. Due to the lower remaining electric field, the number of residual gas ions increases with the compensation degree. Close to full compensation, the electric field produced by the ion charge becomes significant. In these cases, the real behaviour will differ from (4.8). In relation to the beam line charge density, $\lambda_\mathrm{rgi}(R_\mathrm{b})\,/\lambda_\mathrm{beam}$, a change in compensation leads to the same behaviour as a reduction of beam current.

4.2. Sources of compensation electrons

In a beam transport line, secondary particles are continuously introduced by various processes. Both ions and electrons can ionize remaining residual gas atoms and will, on impact with the vacuum vessel or other objects within their path, release further secondary particles. In the following, all of these particles will be said to be "produced", even though no new particles are actually formed.

The level of compensation results from a balance between the rate at which these are formed and at which these are able to escape the system. Therefore, an important ingredient in a model of the compensation are the production processes. In this section, those most relevant for proton beams will be covered.

4.2.1. Proton impact ionization

Using the semiempirical model by Rudd et al. [48], the differential cross section for the ionization of a shell i containing N_i electrons can be calculated from

$$\frac{\mathrm{d}\sigma}{\mathrm{d}W} = 4\pi a_0^2 R^2 N_i B_i^{-3} \frac{F_1(t) + F_2(t)\, w}{1 + \exp\left(\alpha\,(w - w_c(t))\, t^{-1/2}\right)} \frac{1}{(1+w)^3}. \tag{4.9}$$

$w = W/B_i$ is the energy of the secondary electron W scaled by the binding energy B_i, $t = (m_\mathrm{e}/m_\mathrm{p})T/B_i$ the energy of the proton T scaled by the electron-proton mass ratio and the binding energy. $R = 13.6\,\mathrm{eV}$ is the Rydberg energy constant and $a_0 = 0.529\,\text{Å}$ the Bohr radius.

The dependence on the projectile energy is contained in the functions

$$w_c(t) = 4t - 2\sqrt{t} - R/(4B)$$

and

$$\begin{aligned} F_1(t) &= L_1(t) + H_1(t) & F_2(t) &= L_2(t)\, H_2(t)\,/(L_2(t) + H_2(t)) \\ H_1(t) &= A_1 \ln(1+t)\left(t + B_1 t^{-1}\right)^{-1} & H_2(t) &= A_2 t^{-1} + B_2 t^{-2} \\ L_1(t) &= C_1 t^{D_1/2}\left(1 + E_1 t^{D_1/2+2}\right)^{-1} & L_2(t) &= C_2 t^{D_1/2}. \end{aligned}$$

The parameters $A_{1,2} \ldots D_{1,2}$, E_1 and α need to be fitted to measured cross sections. Reference [48] lists values for various gas atoms and molecules. Those that were used in this thesis are listed in Table 4.1. The authors give values for "inner shells", which is to be used for all shells with $B_i < 2B_{1\mathrm{s}}$, where $B_{1\mathrm{s}}$ is the ionization energy of the first shell. The atomic data required for the calculation for these gases in Table 4.2 was taken from the same reference.

Figure 4.3a shows the total and differential ionization cross sections for various gases that were used in the simulations. The total cross sections were determined by numerical integration of (4.9). Their maxima all fall inside the range of beam energies typically found in low-energy beam transport sections.

The authors of the model report an accuracy of probably 10 % to 15 % for the argon ionization cross sections in the range between 50 keV to 500 keV and for electron energies below a few hundred eV.

For impact of 120 keV protons on argon atoms, the average secondary electron energy is 27.5 eV and the median of the distribution is 12.6 eV.

Species	A_1	B_1	C_1	D_1	E_1	A_2	B_2	C_2	D_2	α
He	1.02	2.4	0.70	1.15	0.70	0.84	6.0	0.70	0.50	0.86
Ar	1.20	8.0	0.86	0	0.80	0.90	2.7	0.75	0.80	0.71
H_2	0.96	2.6	0.38	0.23	2.2	1.04	5.9	1.15	0.20	0.87
N_2	1.05	12.0	0.74	-0.39	0.80	0.95	1.20	1.00	1.30	0.70
Inner shells	1.25	0.5	1.00	1.00	3.0	1.10	1.30	1.00	0	0.66

Table 4.1.: Fitting constants for Rudd's model. Excerpt from [48, Table V].

	B	U	N
1s	24.59	39.51	2

(a) He

	B	U	N
$1\sigma_g$	15.43	31.96	2

(b) H_2

	B	U	N
1s	3202.9	4192.9	2
2s	326.0	683.1	2
2p	249.18	651.4	6
3s	29.24	103.5	2
3p	15.82	78.07	6

(c) Ar

	B	U	N
$1\sigma_g$	409.9	601.78	2
$1\sigma_u$	409.9	602.68	2
$2\sigma_g$	37.3	69.53	2
$2\sigma_u$	18.78	62.45	2
$1\pi_g$	16.96	55.21	4
$3\sigma_g$	15.59	44.27	2

(d) N_2

Table 4.2.: Atomic data for the gases used in the space charge compensation simulations: binding energy B in eV, kinetic energy U (required only for the BEB cross section) in eV and number of electrons N. Excerpt from [48, Table I(a)].

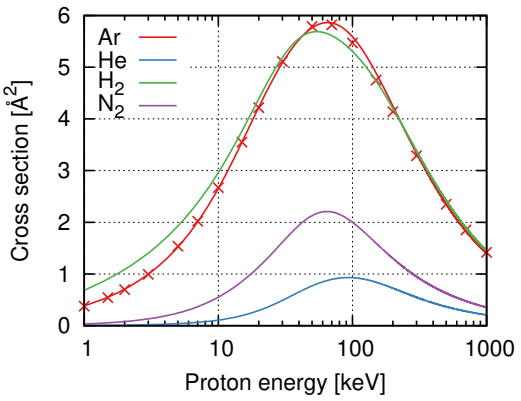

(a) Total ionization cross section for various gases. Solid lines calculated using Rudd's model, data points from [49, Table IV].

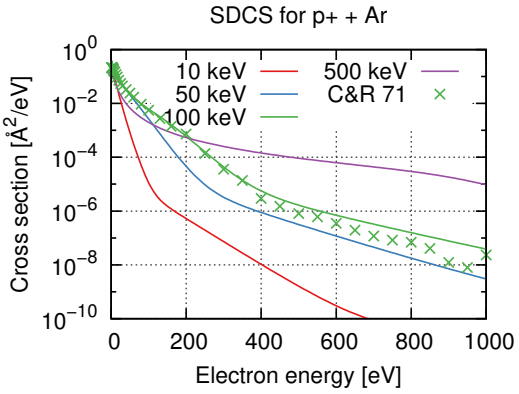

(b) Single differential cross section of argon for various proton energies. Data "C&R 71" from [50, p. 424].

Figure 4.3.: Cross sections calculated from Rudd's model for proton impact ionization.

For multiatomic targets more than one reaction is possible on proton impact, such as

$$\begin{aligned} \mathrm{p} + X_2 &\rightarrow \mathrm{p} + \mathrm{X}_2^+ + \mathrm{e}^- && (4.10)\\ &\rightarrow \mathrm{p} + \mathrm{X}^+ + \mathrm{X}^0 + \mathrm{e}^- && (4.11)\\ &\rightarrow \mathrm{p} + \mathrm{X}_2^{2+} + 2\mathrm{e}^- \\ &\dots \end{aligned}$$

The remaining ions and atoms could also remain in excited states. The cross section calculated from (4.9) only predicts the total ionization cross section and leaves the remaining ion unspecified.

Data from Shah and Gilbody [51, Table 1] for molecular hydrogen shows that the cross section for the dissociation reaction only contributes at most 14 % to the total ionization cross section at the lowest measured energy of 38.3 keV. For higher energy, the fraction decreases further. Considering the uncertainties in the cross sections, for H_2, it should be valid to only include reaction (4.10). For molecular nitrogen, such data could not be found. The current implementation also assumes that only N_2^+ is formed.

4.2.2. Electron impact ionization

Only a fraction of the electrons resulting from proton impact ionization have enough energy to ionize an additional gas atom. For a 120 keV proton beam passing though an argon gas, (4.9) predicts, that 45 % of the electrons have energies higher than the lowest ionization energy. When the remaining beam potential is sufficiently small, electrons cannot gain enough energy to cause further ionization.

This is not the case during build-up of the compensation, in cases of low compensation degrees as well as for high-intensity beams. Thus, *bender* also includes a model for electron impact ionization.

The Binary-Encounter-Bethe (BEB) model [52] was chosen to calculate the cross section for electron-impact ionization. The SDCS of a single shell i as defined by the BEB theory is given by

$$\frac{\mathrm{d}\sigma_i(t,w)}{\mathrm{d}w} = 4\pi a_0^2 N \left(\frac{R}{B}\right)^2 \sum_{n=1}^{3} F_n(t) \left[\frac{1}{(w+1)^n} + \frac{1}{(t-w)^n}\right], \tag{4.12}$$

$$\text{where} \quad F_1(t) = -\frac{F_2}{t+1}, \quad F_2(t) = \frac{2-(b/N)}{t+u+1}, \quad F_3(t) = \frac{b}{N}\frac{\ln(t)}{t+u+1}.$$

The primary particle energy T, the secondary electron energy W and the mean kinetic energy U of a bound electron are all incorporated after division by the binding energy B: $t = T/B_i$, $w = W/B_i$, $u = U/B_i$. Multiple electrons in the same shell are included by multiplication of the cross section with their number N_i. The data from Table 4.2 was used. $b = 1.605$ for Helium and $b = 1.173$ for H_2 was taken from [52, Table I]. For nitrogen and argon, $b/N = 1$ was assumed.

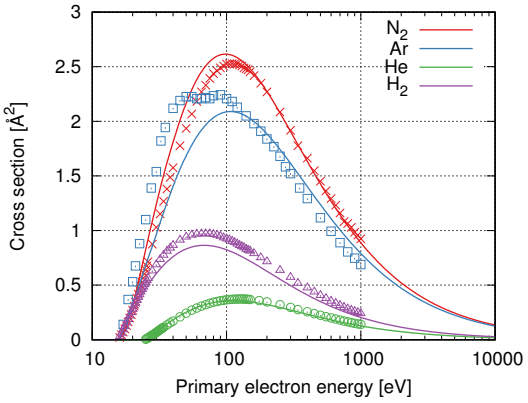

(a) Total ionization cross section for various gases. Comparison against data from [53, Table V], data for argon from [54, Table II].

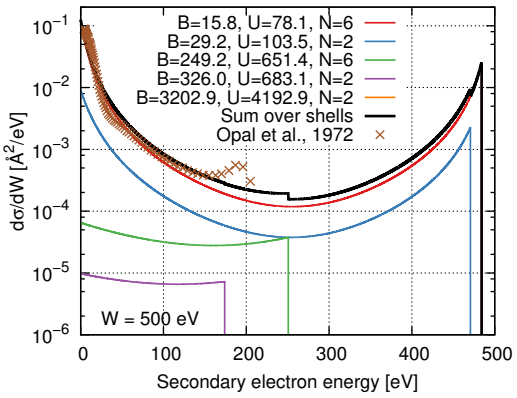

(b) Single differential cross section for argon. Comparison against data from [55].

Figure 4.4.: Cross sections calculated from the BEB model [52] (solid lines) in comparison to measured data (data points).

Integrated over w, the total cross section of a single shell is

$$\sigma_i(t) = \frac{4\pi a_0^2 N \left(R/B\right)^2}{t+u+1} \left\{ \frac{1}{2}\frac{b}{N} \left(1-t^{-2}\right) \ln(t) + \left(2-(b/N)\right) \left[1 - t^{-1} - \frac{\ln(t)}{t+1} \right] \right\}. \quad (4.13)$$

Figure 4.4 shows data for various gases as well as the differential cross section for electron impact ionization of argon. In general, agreement to the presented measured data from [53], [54] and [55] is quite good, even though some features such as the maximum of the cross section in argon or the small peak in the secondary cross section data are not well reproduced.

4.2.3. Secondary electron production on surfaces

An additional purpose of Low-Energy Beam Transport sections is often the separation of unwanted ion fractions. From proton ion sources, a fraction of H_2^+ and H_3^+ ions is extracted. Since these ions have a higher magnetic rigidity, they are not focused as strongly as the main beam and are continually lost throughout the beam line. In addition, the transmission of the beam is often not 100 %. When these ions hit the vacuum vessel, electrons and atoms are emitted. The atoms will not be considered further here. Depending on the projectile as well as the surface material and composition, the number of produced electrons at energies used in LEBT sections is in the order of $\eta = 1 \ldots 10$ electrons per ion [56]. Thus, when the losses per meter

$$\frac{\lambda_{\text{loss}}}{I_{\text{b}}} > \frac{1}{\eta} \frac{p\sigma}{k_{\text{b}} T}, \quad (4.14)$$

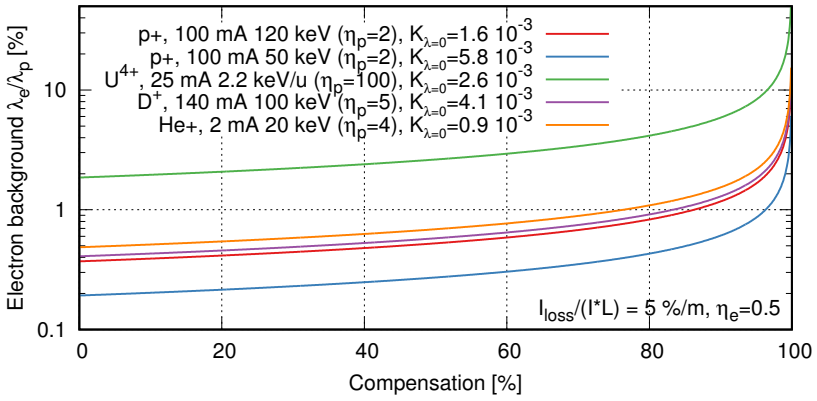

Figure 4.5.: Electron background forming due to particle losses on the vacuum vessel. Values of η_p are rough guesses.

the number of electrons produced by secondary electron emission exceeds that of the ionization process with cross section σ. At $p = 1 \times 10^{-3}\,\mathrm{Pa}$ and $\sigma = 5.3\,\text{Å}^2$ (proton impact ionization cross section on argon at 120 keV), even at a comparatively low value of $\eta = 2$, (4.14) results in $0.6\,\%\,\mathrm{m}^{-1}$. Thus, it is quite likely that the electron production rate at the walls exceeds that of impact ionization.

The secondary electrons emitted from the walls will see the attractive potential of the beam and oscillate once across its volume. If during this period no process leads to an energy loss, they will simply hit the wall on the opposite side of the system. There is some probability, that the electron is reflected or produces a number of secondary electrons—[57] gives a value of $\eta_e = 50\,\%$ for electrons close to 0 eV impacting a stainless steel surface. The charge of the electrons in flight will provide some compensation. The line charge density of electrons inside the beam can be estimated using

$$\lambda_\mathrm{e} = \eta_\mathrm{p}\lambda_\mathrm{loss}T_\mathrm{transit}\sum_{i=0}^{\infty}\eta_\mathrm{e}^i = \frac{\eta_\mathrm{p}}{1-\eta_\mathrm{e}}\frac{I_\mathrm{loss}}{L}T_\mathrm{transit}, \tag{4.15}$$

where T_transit is the time required for an electron to cross the vacuum vessel. Assuming radial symmetry and since electrons outside the beam's volume have no influence on it, one can assume that new electrons are directly created at its edge with no initial energy. The real transit times will be lower due to the velocity gained outside the beam radius. Then,

$$\frac{\lambda_\mathrm{e}}{\lambda_\mathrm{b}} = \frac{\eta_\mathrm{p}}{1-\eta_\mathrm{e}}\frac{I_\mathrm{loss}}{I_\mathrm{b}L}\sqrt{2\frac{m_\mathrm{e}}{e}\epsilon_0}\frac{(\pi v_\mathrm{b})^{3/2}}{\sqrt{(1-\eta)\,I}}R_\mathrm{b} = \frac{\eta_\mathrm{p}}{1-\eta_\mathrm{e}}\frac{I_\mathrm{loss}}{I_\mathrm{b}L}\pi\sqrt{\frac{m_\mathrm{e}}{m_\mathrm{b}}}\sqrt{\frac{Q}{K}}R_\mathrm{b}. \tag{4.16}$$

Under the given assumptions, the background is thus proportional to the beam loss per meter, the beam radius and inversely proportional to square root of the beams perveance K. Q is the charge state of the beam. (4.16) diverges for compensation degrees $\eta \to 1$

due to the vanishing electric field. In this case however, the assumption that the electron background does not significantly alter the electric field of the beam is not valid.

Figure 4.5 displays values calculated from (4.16) for various beam parameters. Unless the beam is already strongly compensated by some other effect, the contribution from secondary electrons is negligible. With the same argument, secondary electrons from residual gas ions—the yield for Ar^+ ions is lower than 0.1 for energies below 100 eV [58]—as well as from escaping electrons can be neglected.

The situation is different in cases when the beam impinges on a surface longitudinally. Initial simulations showed instabilities due to the electrons propagating against the beam's direction. These were not pursued further.

4.2.4. Simulation of ionizing collisions

The probability for a process j to occur for a particle with energy E_i in a time step Δt is given by

$$P_{i,j} = 1 - \exp(-n_\mathrm{t}(\mathbf{r})\,\sigma_j(E_i)\,v_i\Delta t) = 1 - \exp(-\nu_{i,j}(\mathbf{r}, E_i)\,\Delta t)\,, \tag{4.17}$$

where σ_j is the cross section, n_t the density of the target species, $v_i\Delta t$ the distance traveled and $\nu_{i,j}$ the collision frequency. Evaluating equation (4.17) directly for each particle in each step is computationally expensive: the main cost comes from evaluating the cross section for each particle energy in every step.

By introducing a maximum collision frequency,

$$\nu_\mathrm{max} = \max_{\mathbf{r},E}(\nu(\mathbf{r}, E)) = \max_E(v\sigma_\mathrm{T}(E)) \max_\mathbf{r}(n_\mathrm{t}(\mathbf{r}))\,, \tag{4.18}$$

where the total cross section σ_T is the sum of the cross sections of all possible processes, the upper limit of collisions per step can be calculated,

$$N_\mathrm{col} = N_\mathrm{particles}\,(1 - \exp(-\nu_\mathrm{max}\Delta t))\,. \tag{4.19}$$

N_col particles are then picked at random. To reproduce the exact collision rate, the implementation in *bender* carries over the fractional part between time steps. For each of these particles, the collision rates $\nu_{i,j}$ are then calculated and compared to ν_max. Drawing a random number $R \in [0, 1]$, reaction 1 occurred if $R < \nu_1/\nu_\mathrm{max}$, reaction 2 occurred if $\nu_1/\nu_\mathrm{max} < R < (\nu_1 + \nu_2)/\nu_\mathrm{max}$ and so on. For $R > \sum_j \nu_j/\nu_\mathrm{max}$, no collision is calculated. This algorithm is called Null collision method [59] for this reason. The approach is illustrated in Figure 4.6 including three possible unspecified processes.

Using the Null collision method, the collision probability only needs to be calculated for N_col particles instead for all particles. For the simulations below, the ratio to the number of macroparticles was in the order of per mill. In cases where ν_max does not differ greatly from the sum of all collision rates, this number should be small, because otherwise the probability for multiple collisions to occur during one timestep is not negligible anymore.

When an ionizing collision was found to have occurred, the energy of the secondary particle W_sec is picked at random from the distribution given by the differential cross

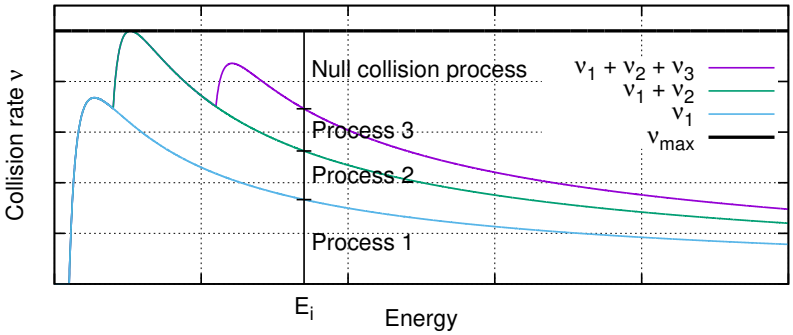

Figure 4.6.: Null collision algorithm: the selection of particles is performed using a maximum collision frequency, after which the type of collision is determined including a "null collision".

section of the reaction. Apart from the secondary electron energy, only the momentum and energy of the incoming projectile as well as the binding energy B are known. Both the final velocity vector of the projectile as well as that of the remaining ion are unknown, as is the direction of movement of the secondary electron.

To be able to calculate these quantities, the following assumptions were made:

1. Rotational symmetry around the projectile velocity vector. Since the orientation of the gas atoms or molecules is completely random, this assumption should be valid.

2. The secondary electron emission angle is known. For the present simulations, as a rough estimation, a completely isotropic distribution was assumed. In reality, for certain secondary electron energies, the differential cross sections differ over many orders of magnitude over different emission angles, both for proton impact ionization (114 keV $\mathrm{p} + \mathrm{H_2}$, [60, Fig. 2]) and electron impact ionization (500 eV $\mathrm{e^-} + \mathrm{Ar}$, [61, Fig. 2]). If a significant influence of the simulation results on the secondary electron angular distribution should be found, the angular distribution could also be taken from double differential cross section data.

3. The ion moves in the same direction as the incoming projectile, $\varphi_\mathrm{i} = 0$.

The main goal of this model is not to provide an accurate model of the kinematics of ionizing collisions but to ensure energy and momentum conservation in the simulation. Under the given assumptions, calculation of the three remaining quantities φ_p, v_p and v_i is possible.

The final ion momentum is

$$p_\mathrm{i} = \left(1 + \frac{m_\mathrm{p}}{m_\mathrm{i}}\right)^{-1} \left\{ \Delta p - \sqrt{\Delta p^2 - \left(1 + \frac{m_\mathrm{p}}{m_\mathrm{i}}\right)\left[\left(1 + \frac{m_\mathrm{p}}{m_\mathrm{t}}\right) p_t^2 + 2 m_\mathrm{p} B - 2 \bar{p}_\mathrm{p} p_\mathrm{t} \cos\varphi_\mathrm{t}\right]} \right\},$$

with $\Delta p = \bar{p}_\mathrm{p} - p_\mathrm{t} \cos\varphi_\mathrm{t}$. The quantities with indices t, p and i label properties of the target electron, the projectile ion or electron and the residual gas ion respectively. $\bar{p}_\mathrm{p}$ is

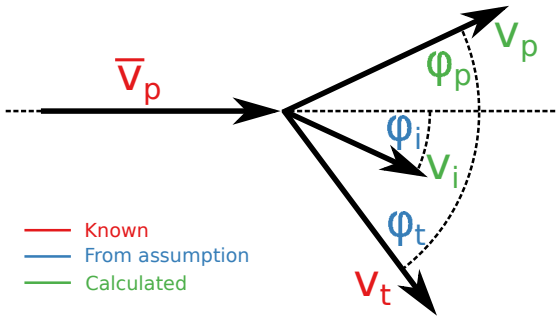

Figure 4.7.: Quantities in the classical collision model.

the momentum of the incoming projectile. The argument of the square root is negative for $\cos\varphi^{-}_{\mathrm{t,min}} < \cos\varphi_\mathrm{t} < \cos\varphi^{+}_{\mathrm{t,min}}$, where

$$\cos\varphi^{\pm}_{\mathrm{t,min}} = -\frac{m_\mathrm{p}}{m_\mathrm{i}}\frac{\bar{p}_\mathrm{p}}{p_\mathrm{t}} \pm \sqrt{\left(1+\frac{m_\mathrm{p}}{m_\mathrm{i}}\right)\left[\left(\frac{m_\mathrm{p}}{m_\mathrm{i}}-1\right)\frac{\bar{p}_\mathrm{p}^2}{p_\mathrm{t}^2} + \frac{m_\mathrm{p}}{m_\mathrm{t}}\left(1+\frac{B}{E_\mathrm{t}}\right)+1\right]}. \tag{4.20}$$

For high secondary electron energies in the range of the projectile energy, this limits the emission angle to either the forward or the backward direction. Figure 4.8a shows the dependence of the final ion energy in the impact of a 500 eV electron on argon. The energy imparted on the ion is largest for backward emission of the electron. For the depicted case, due to the huge mass difference, only up to 25 meV are transferred. However, also in cases with no mass difference such as 120 keV proton impact on atomic hydrogen, the predicted energy transfer to the ion does not exceed a few 10 eV.

The final proton momentum is then

$$p_\mathrm{p} = \sqrt{(\Delta p - p_\mathrm{i})^2 + p_\mathrm{t}^2 \sin^2\varphi_\mathrm{t}}$$

and the scattering angle of the projectile is related to that of the electron by

$$\sin\varphi_\mathrm{p} = \frac{p_\mathrm{t}}{p_\mathrm{p}}\sin\varphi_\mathrm{t}.$$

Figure 4.8b shows the scattering angle of the projectile. Since the calculation is classical, it is possible to distinguish the incoming projectile from the secondary electron. Most electrons are deflected only by a few degrees and the deflection decreases with the increased projectile velocity. For 120 keV protons for example, the angular distribution has a similar shape centered at 0.1 mrad.

In the implementation in *bender*, the calculation is made in a frame oriented along the direction of movement of the projectile. The two "created" macroparticles are then rotated back into the reference frame.

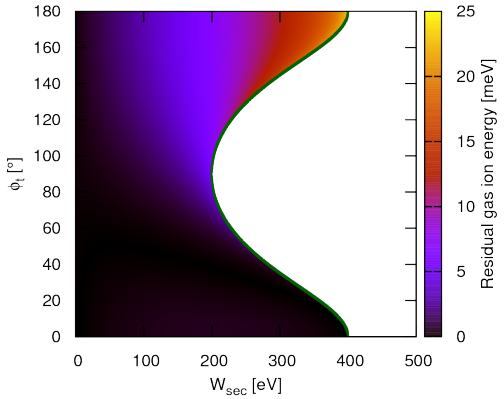

(a) Ion energy distribution for 500 eV electron impact on argon. The green lines are the two branches of (4.20).

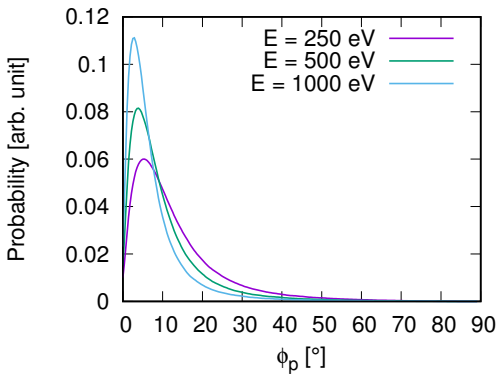

(b) Scattering angle of the projectile.

Figure 4.8.: Results from the classical collision model for electron impact ionization of argon gas.

4.3. Simulation of a drift system

Space charge compensation in two scenarios was investigated: in a beam drift over a distance of 50 cm and in a model LEBT section consisting of two solenoids. Only the results for the drift section will be presented here.

A 120 keV proton beam was transported. This is the maximum beam energy of the low-energy beam transport section at the upcoming FRANZ facility (Section 5.2.2) and will enable a comparison between simulation results and measurements. A beam current of 100 mA with a homogeneous distribution and an rms emittance of 25 mm mrad (unnormalized) were arbitrarily chosen. For the drift system, the beam was matched using *tralitrala* in a way that no particles are lost inside the system for currents below 100 mA. The ellipse parameters of $\alpha = 7.4$ and $\beta = 1.89$ m were chosen so that the envelope of the beam is approximately symmetric around the middle of the system for full current as well as for 95 % compensation. At full current, most particles are reflected before crossing the beam core, while at high compensation, most particles are able to cross over. The beam envelope along with some particle tracks are displayed in Figure 4.9.

The simulated systems are bounded by cylindrical repeller electrodes. For the drift system, unless otherwise specified, a beam pipe with 4 cm diameter terminated by repellers with 5 mm length and an aperture of 35 mm was used. In such a geometry, the potential on the axis drops to 56 % of the applied voltage. Thus, to prohibit an electron with no energy from leaving the system longitudinally, at least about twice the beam potential (400 V) has to be applied. To also stop electrons with higher energies, a voltage $U_{\mathrm{rep}} = -1.5$ kV of about four times the uncompensated beam potential was used if not otherwise specified. This guarantees that there is no particle flux from or to the simulation volume.

Unless otherwise specified, argon was used as a residual gas. This choice was made due

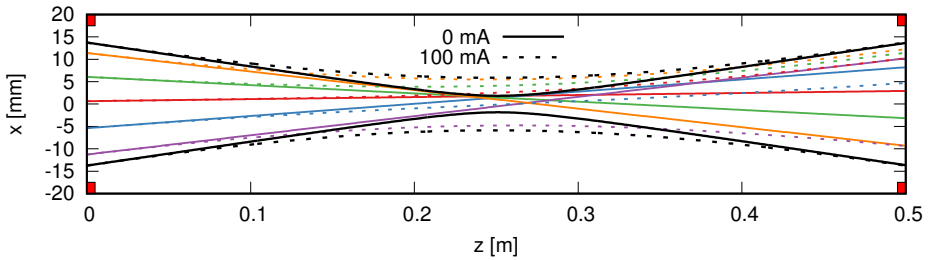

Figure 4.9.: Beam envelope at full current and full neutralization (black curves), along with some particle tracks (colored). The red rectangles give the location of the repeller electrodes.

to the comparatively high ionization cross sections—keeping simulation times low—and to avoid dealing with multiple reaction products as in the case of gases forming molecules. Another factor was the availability of tabulated double differential cross section data [50]. This data however was not used.

In a real low-energy transport line, the residual gas will likely contain a large amount of gas from the ion source, with the pressure decreasing with distance, depending on the beam pipe geometry and pump position. To avoid the complexity involved in interpreting the results of a simulation with locally varying production rate, a constant pressure is assumed over the simulation volume. An argon background of $p = 1 \times 10^{-5}$ mbar was used, except where otherwise specified. Experimentally, such a composition could be achieved by flooding a vacuum chamber with argon gas.

Secondary electrons from particle impact on the vacuum vessel were not considered, since their influence was estimated to be small (see Section 4.2.3).

The simulations were made using the Fourier solver described in Section 3.2.2 utilizing quarter symmetry by using Neumann boundary conditions on the $x - z$ and $y - z$ planes. Due to the rectangular geometry, there is a systematical error. The electric field along the axes will always be higher than along the diagonals. Furthermore, the repeller electrodes are not included as boundary conditions in the calculation of the potential of the particles. Due to the large aperture compared to the beam pipe radius, the influence on the potential by this should be small. A grid resolution of approximately 0.4 mm in all three directions and a time step of 50 ps was used.

For the drift system, on two nodes of the HHLR Fuchs Cluster[2], at 1000 particles per step (resulting in 2.1 million proton, 1.8 million electron and 200000 residual gas ion macroparticles), 50 µs of simulated time or one million steps took two weeks.

4.3.1. Build-up of compensation

If no electrons were lost, compensation should reach 100 % after $\tau_{\mathrm{scc}} \approx 16.25$ µs (equation (4.4)).

[2] AMD Opteron Processor 6172, 2.1 GHz, 12-core [62]

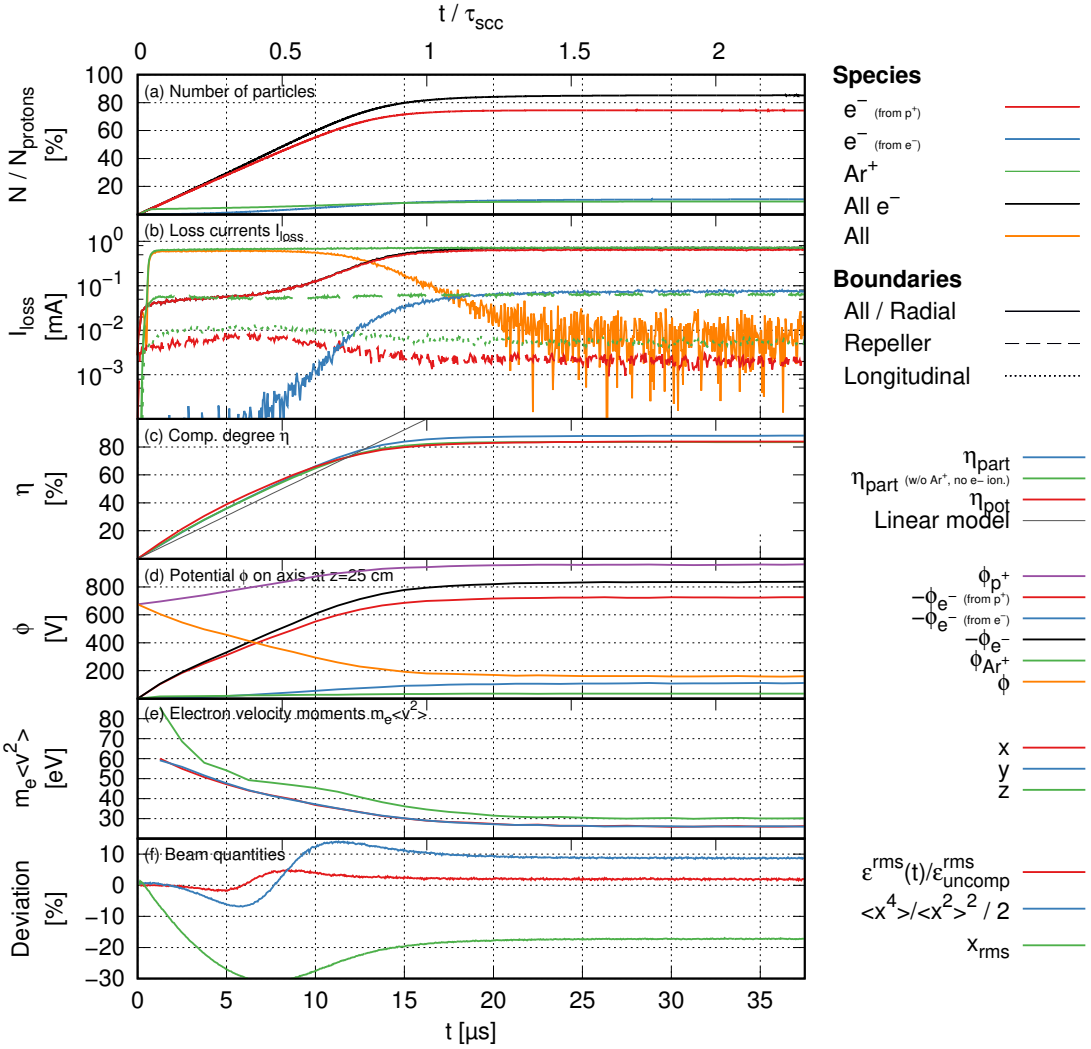

Figure 4.10.: Time dependence of various parameters of the drift simulation. (a) Number of particles in the simulation in comparison to the number of protons. (b) Currents of secondary particles lost on the negatively biased repeller electrodes, longitudinally on the axis and radially. (c) Compensation degrees as defined by (4.1) and (4.2) averaged over the inner 30 cm of the system i.e. outside the field of the repeller electrodes. (d) Potential at the center of the system, $r = 0\,\mathrm{m}$ and $z = 25\,\mathrm{cm}$. (e) Second moments in velocity for the compensation electrons. (f) Deviation of various beam parameters after transport, such as emittance, kurtosis and rms size.

Figure 4.10 shows various parameters of the simulation over time. The build-up of the compensation can be separated in three periods depending on the electron losses: a period of nearly loss-free accumulation of electrons until approximately $0.4\tau_{\mathrm{scc}}$, a relaxation period where the beam potential is reduced far enough for more electrons to escape the system and a steady-state starting at approximately τ_{scc} in which electron production and losses are balanced and in which the beam transport remains stable.

At the start of the build-up phase, electrons are only produced by proton impact ionization and the number of particles in the simulation increases linearly with the production rate predicted by equation (4.5). The average compensation degree outside the influence of the repellers rises faster than predicted by the linear model. This is a result from electrons accelerated out of the repeller region. In the first 10 µs, the number of electrons from electron impact ionization rises quadratically.

Initially, the number of residual gas ions increases with the electron production rate. Starting after the shortest initial ion arrival time predicted by (4.6) for ions created at the beam edge at the center of the system, $T(6\,\mathrm{mm}, 20\,\mathrm{mm}) \approx 0.4\,\mu\mathrm{s}$, the current increases within 0.6 µs to P_{p^+}. 1 µs is approximately the time required for ions from the axis to reach the beam pipe. The average charge density inside the beam at this point is $0.29\,\mathrm{nC\,m^{-1}}$ (1.5 % of the beam's line charge density). Including the compensation degree of 11 %, the result of (4.8) is $0.27\,\mathrm{nC\,m^{-1}}$. This indicates that at this level of the compensation build-up, the assumption used in the derivation of (4.8) holds quite well.

After approximately $0.5\tau_{\mathrm{scc}}$, the potential becomes low enough for an increasing number of electrons to escape the system and the curve for the number of particles in the system differs from linear behaviour. Around this time, significant deviations in the beam parameters can be observed. The decrease in x_{rms} is a result of the beam matching. As the space charge forces decrease, the focus point of the beam initially moves backwards as protons are deflected outwards radially later and later. This shows up as a decrease in beam radius after 50 cm. At some point, more particles are able to cross over the axis and the focus moves inwards again, leading to an increase in x_{rms} at the end of the system. The same behaviour is present in calculations, where the compensation is treated by a constant compensation factor, with a minimum in x_{rms} at around 50 % compensation.

Regardless of the high repeller voltage, a tiny fraction of the electrons is still able to escape the system longitudinally. Those are formed within the repeller with a sufficiently high initial velocity pointing out of the system. Their number, also shown in Figure 4.10b, initially increases until $0.5\tau_{\mathrm{scc}}$ and then decreases. The reason for this behaviour is the movement of the focus. When the beam radius at the end of the system is smaller, the beam potential is larger, compensating the repeller voltage, which allows more electrons to escape.

The beam initially becomes hollow (kurtosis smaller than 2) and the beam emittance decreases by approximately 2 %. This effect can be explained by the non-linear field appearing due to the nonproportional distribution of the electrons and will be discussed in Section 4.4.

After τ_{scc}, the compensation degree η_{pot} already has 96.7 % of its equilibrium value $\eta_{\mathrm{pot}}^{\mathrm{eq}} = 83.9\,\%$. From there, the difference of η_{pot} to the last simulated value falls exponentially with a (fitted) time constant of 3.6 µs.

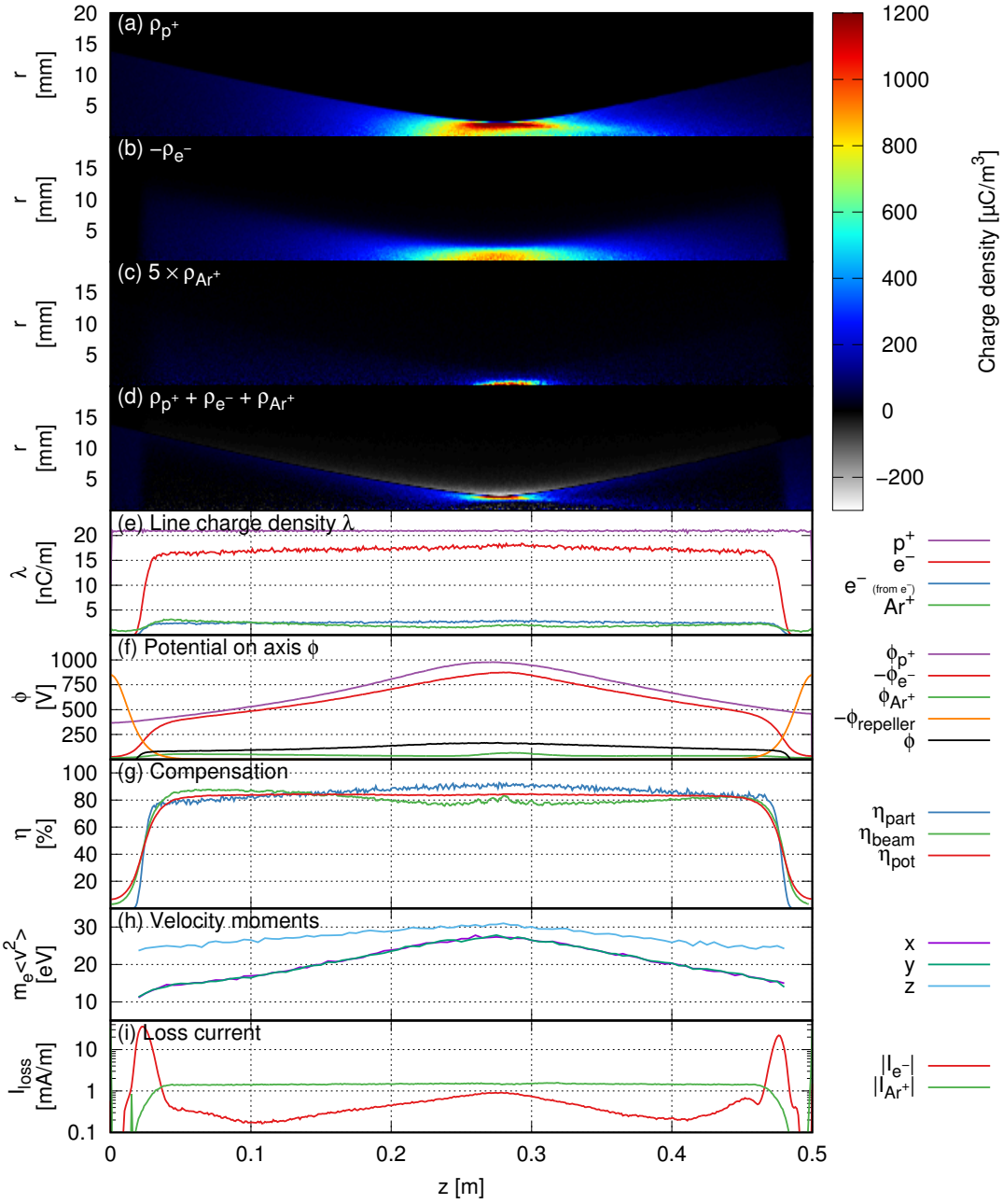

Figure 4.11.: Spatial dependence of various quantities in the drift simulation in the steady state, $t = 37.5\,\mu s$. (a)-(d) Charge density $\rho(r, z)$ for the beam, compensation electrons, residual gas ions and the total charge density. (e) Line charge density. (f) Total potential and potential $\varphi(r = 0)$ for all simulation species and the repeller electrodes on the axis. (g) Compensation degree as defined by (4.1) and (4.2). (h) Second-order velocity moments of the electrons. (i) Loss current of compensation electrons and residual gas ions.

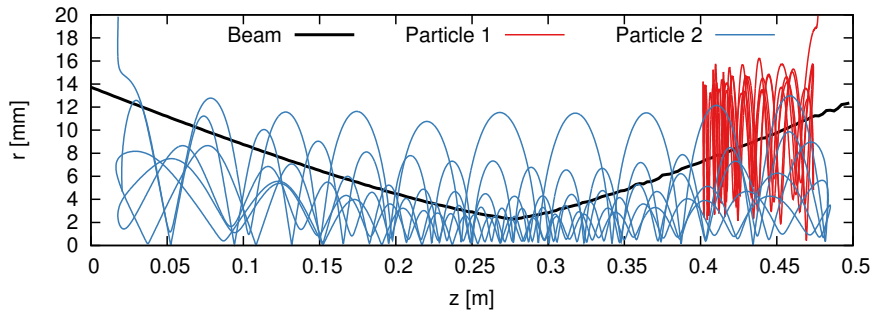

Figure 4.12.: Two electron tracks from the compensation simulation of the 50 cm drift.

4.3.2. Steady state

Figure 4.11 shows the charge density of the simulated species as well as the remaining charge density in the steady state. The reduction of the potential on the axis η_{pot} is nearly constant outside of the repeller's range, varying by 0.6 %. η_{beam} achieves a maximum of 87 % at $z = 7.5$ cm but decreases to 77 % in front of the focus point (24 cm). In the focus point, there is a small local maximum of 81 %. At the end of the system outside of the repeller's reach, $\eta_{\text{beam}} = 83\,\%$.

The beam, homogeneously distributed initially, clearly becomes hollow around the focus and then relaxes again to a more homogeneous distribution. The increase in density at the beam edge in the focus is not well compensated by the electrons and thus also shows up in the plot of the net charge density in Figure 4.11d.

Instead of remaining confined to the beam volume, some electrons are present at the edge of the beam. The negative charge density in the simulation sometimes takes on values of about 25 % of the beam's charge density at the edge. The compensation electrons oscillate through the beam radially as well as longitudinally. Figure 4.13 shows some exemplary particle tracks. Longitudinally, most electrons move between the electric fields of the two repellers at almost constant velocity, where they get reflected sharply. Sometimes, these slow down somewhat at a location close to the beam's focus. For the few particle tracks that were exported from the simulation, oscillation times from 0.15 µs to 0.4 µs were found. Some of the electrons do not have sufficient energy to cross between the two sides, oscillating between repeller and focus. There are also some particles switching between these two behaviours.

The transverse oscillations have a much higher frequency, exemplary values range from 3 ns to 15 ns per oscillation. Since the charge density remaining near the axis is low, so are the electric fields, i.e. most electrons move through the center at constant velocities and only experience a force near the beam edges, reversing their motion somewhere outside of its radius.

The argon ions form a low background of about 10 %. Near the axis at the beam's focus, an accumulation of ions with a charge density of up to 100 µC m^{-3} (63 % of the beam's density) can be found. This is surprising since one would assume the highest radial electric fields to be present at this location. The effect only starts to occur at about

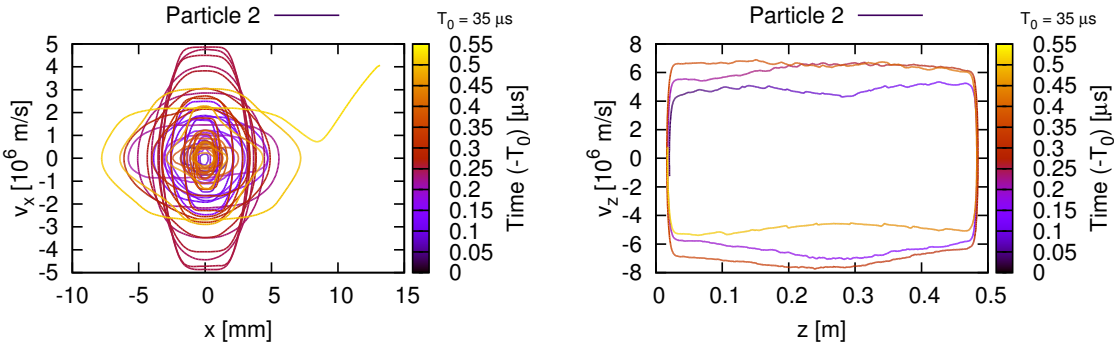

(a) $x - v_x$. (b) $z - v_z$.

Figure 4.13.: Two projections of phase space for the second electron from Figure 4.12.

$0.6\tau_{scc}$, when the residual gas ion to electron ratio starts to decrease at the focus while remaining approximately constant over time in the areas surrounding it. The source of these effects will be explained in Section 4.4.2.

In the final state, the loss currents of electrons and residual gas ions are equal. Apart from $P_{p^+} = 1.28\,\mathrm{mA\,m^{-1}}$, ionization by electron impact contributes another $0.2\,\mathrm{mA\,m^{-1}}$. Figure 4.11i contains the radial loss profile of the electrons and the residual gas ions. Over the largest part of the system, the loss rate for residual gas ions matches the production rate exactly, since the ions are lost at the same longitudinal positions at which they are formed. Only in the region affected by the repellers, the rate deviates. Some ions are able to reach the first repeller, but most of the particles are extracted from the system longitudinally.

A large number of the compensation electrons escape the system around $z = 2.5\,\mathrm{cm}$ and $z = 47.5\,\mathrm{cm}$. Responsible are the electric fields pointing from the grounded beam pipe towards the negatively biased repellers. Electrons reaching the maximum of their radial oscillation in the area of these fields get accelerated towards the beam pipe. Transversely, the electron losses show a clear influence of the rectangular boundary conditions imposed by the Poisson solver: electrons are more likely to be lost on the diagonal than on the axes. This dependence disappeared when the rz solver was used.

When a bigger beam pipe radius is used—values up to 40 mm were simulated—the transverse fields close to the beam decrease and the maxima shift more towards the center of the beam. For these simulations, the applied voltage was scaled so that the potential on the beam axis inside the repeller remained constant. While increasing the beam pipe radius increases both η_{part} and η_{pot}, η_{beam} remains almost constant in shape. At larger radii, the only visible effect is a small increase of compensation at both ends of the system and a small decrease in the length of the electron column. Another difference can be found in the electron velocity distributions—the curves Figure 4.11h shift to lower values by about 0.5 eV per 5 mm larger beam pipe. Furthermore, for 25 mm pipe radius and higher, the electron loss rate in the focus point reaches the ion loss current but does not exceed it.

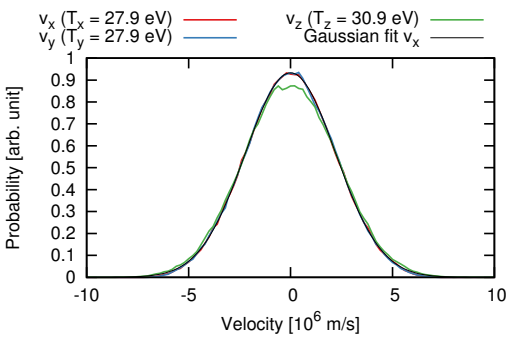

(a) Velocity distribution in each direction. The distributions are well fitted by Gaussian distributions. An example is given for the horizontal direction.

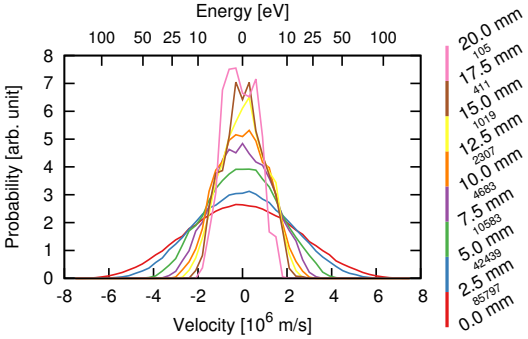

(b) Horizontal velocity distribution for particles at different radii. The y-axis was normalized separately for each ring. The number of macroparticles in each ring is given in the legend.

Figure 4.14.: Distribution of electron velocities in a slice of 4 cm length in the center of the system.

4.3.3. Electron velocity distributions

Figure 4.14 shows the distribution of the electron velocities in a slice of 4 cm length in the center of the system. In the full slice, the distribution can be fitted well by a Gaussian, $f(v) \propto \exp\left(-m_\mathrm{e}v^2/(2k_\mathrm{b}T)\right)$, where $k_\mathrm{b}T \approx 27.9\,\mathrm{eV}$ for the present simulation. For Gaussian distributions, $k_\mathrm{b}T = m_\mathrm{e}\overline{v^2}$, where $\overline{v^2}$ is the second-order velocity moment. Due to the axial symmetry, the "temperatures" T in the transverse directions are equal everywhere. These differ from the longitudinal values.

A similar distribution can be found at every position along the beam outside the range of the repeller electrodes. However, the value of T changes longitudinally, as shown in Figure 4.11h. The maximum of T can be found at the focus of the beam. Towards the front and the back of the system, its value decreases. The effect is more pronounced in the transverse planes, where $T_\mathrm{x,y}$ decreases by 56 %, than in the longitudinal plane, where the decrease is only 27 %.

For the first 10 µs, during the build-up of the compensation, the velocity distributions are more peaked around zero. As can be seen in Figure 4.10e, during this time, the second-order velocity moments approximately decrease by half and then stay constant in the steady-state.

Looking at electrons at different radii, we find deviations from a Gaussian distribution at larger radii. Figure 4.14b shows an example for the same group of particles also found in Figure 4.14a. Due to the large variation in the number of particles in each ring, the displayed distributions are normalized independently. The second-order velocity moment decreases from about 34 eV near the axis to only 3 eV near the beam pipe. One possible reason for this behaviour might be particle losses: since the potential decreases with radius, the kinetic energy for electrons required to escape the system is lower at larger

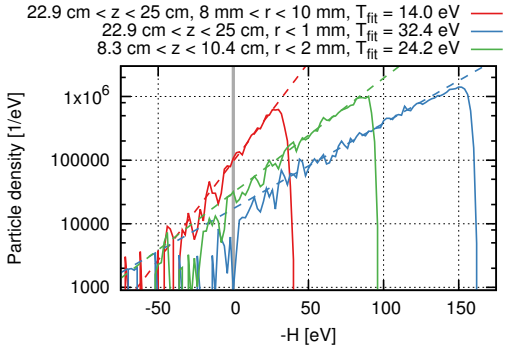

(a) Solid lines give the distribution of the electron energies (kinetic and potential), the dashed lines are exponential fits. The exponential decay is consistent with a Boltzmann distribution.

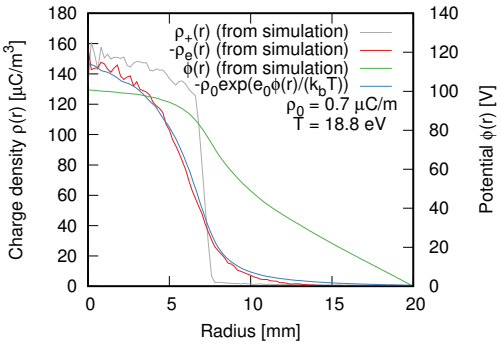

(b) Radial electron density from the simulation (red) as well as a distribution calculated under the assumption of a Boltzmann distribution with a radially constant temperature T (blue) calculated from the simulated potential (green).

Figure 4.15.: The compensation electrons follow a Boltzmann distribution locally, examples are given in (a) at different points. This makes it possible to predict the charge distribution, when temperature and charge normalization factor are known. An example is given in (b).

radii.

In thermal equilibrium, one would expect the electrons to follow a Boltzmann distribution,

$$f(\mathbf{r},\mathbf{p}) = f_0 \exp\left(-\frac{H(\mathbf{r},\mathbf{p})}{k_\mathrm{b}T}\right) = f_0 \exp\left(-\frac{\mathbf{p}^2}{2mk_\mathrm{b}T} + \frac{e\varphi(\mathbf{r})}{k_\mathrm{b}T}\right). \tag{4.21}$$

Integrated over momentum, the density is $n(r) = f_0\sqrt{2\pi m k_\mathrm{b}T}\exp(e\varphi(\mathbf{r})/(k_\mathrm{b}T))$.

Figure 4.15a shows the distribution of electron energies $-H$ found in arbitrarily chosen locations in the *bender* simulation along with exponential fits to these distributions. Similar distributions are found everywhere in the system outside the repeller region. The sizes of the regions were chosen to be large enough for sufficient statistics, but small enough so that the change in temperature over the region is still negligible. The agreement for total energies below 0 eV is quite good. Electron energies above zero are populated less than predicted by (4.21), a likely result of particle losses, since the system reduces its energy when these particles leave the system.

The distribution in a full slice of particles shows exponential behaviour only for particles with lower total energy. However, taking the temperature calculated from the second-order moment of all particles in a slice is sufficient to approximately predict the spatial distribution. The blue curve in Figure 4.15b was calculated using the potential at some longitudinal position within the system as well as the $k_\mathrm{b}T = m\overline{v^2}$ calculated from all particles located in a slice around this location. The result matches the electron density taken from the simulation, verifying the behaviour predicted by (4.21).

The double layers observed in Figure 4.11 along the edge of the beam, also found in Figure 4.15b, are a result of the energy distribution. Since the beam's potential does not immediately decrease to 0 V outside the beam, there are always some electrons with enough energy to temporarily escape its volume.

When the temperature (or temperature distribution) as well as the line charge density along the beam line is known, the Poisson-Boltzmann equation—already used in Section 3.4.1 to generate self-consistent distributions to test *bender*—can be used to calculate the density of the electrons without explicit simulation of the compensation process. The investigation of the influence of the two model parameters on electron distribution and the beam transport, as well as a comparison to the present simulation can be found in Section 4.4.

In [45, p. 162], an upper limit for the electron temperature of at most 0.7 eV is given for a 10 keV, 1.52 mA He^{1+} beam ($K = 1.96 \times 10^{-3}$). Holmes [8, Fig. 12] gives values around 20 eV for a 17.6 mA, 20 keV helium beam ($K = 8.05 \times 10^{-3}$). In order of magnitude, the values from the simulation, where $K = 1.56 \times 10^{-3}$, are similar to the result from Holmes. However, considering the different beam species, background gases and their pressure as well as geometries, it is impossible to draw any further conclusions.

4.3.4. Origin of the electron velocity distributions

Since the thermalization of the electrons is responsible for their distribution and thus the influence on the beam, the question which effect is responsible for the formation of the equilibrium is important.

In an experiment, instead of calculating the energies in a proton impact collision from the cross section, a fixed value E_0 was assumed and electron impact ionization disabled in the simulation. Even when newly introduced electrons were all given $E_0 = 0$ eV kinetic energy initially, energy distributions similar to those shown in Figure 4.15a were found.

When the initial energy E_0 is increased to fixed values from 25 eV to 100 eV, the curves in plots such as Figure 4.15a start to drop off earlier and more towards the low energy end, i.e. lower energy states are less populated than predicted by the Boltzmann distribution. Additionally, the final temperatures increase from 25.3 eV ($E_0 = 0$ eV) to 50.3 eV ($E_0 = 100$ eV) at the center of the system. Thus, the initial electron energies have a significant influence on the temperature, but are not responsible for the appearance of the Boltzmann distribution.

In the steady-state, the densities of the different species and thus the potential is constant on average. In such a situation, one would assume that the total energy of every single particle is also a constant. Figure 4.16 shows that this is not the case. Instead, the energies of the shown particles rapidly fluctuate. On average, the tracks show an increase more often than a decrease over the lifetime of the electron. For some particles, the energy increases over more than 100 eV, a range in the order of the total remaining potential, over a time of 5 µs. Again, we observe that particles with $H > 0$ are not confined and are lost at the boundaries.

The hypothesis was formed, that the stochastic heating described in Section 3.4.1 is responsible for the observed equilibrium. In this case, the average energy of an electron

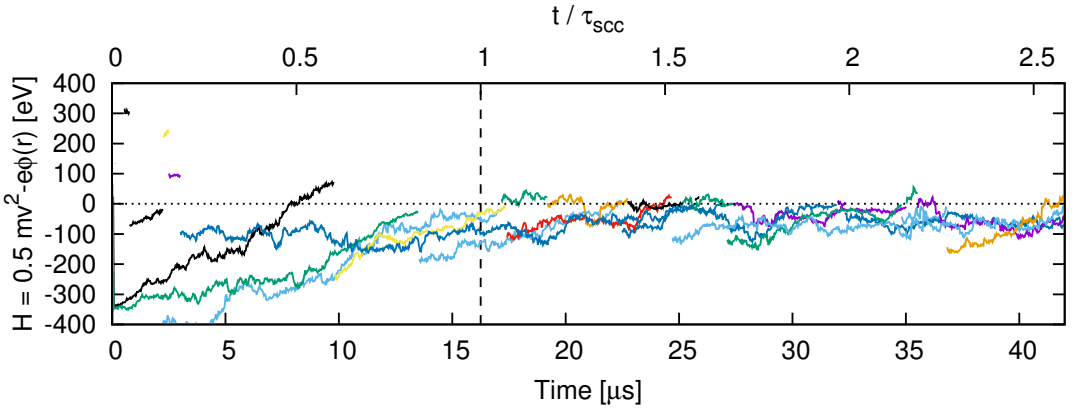

Figure 4.16.: Time dependence of the total particle energy for some exported tracks. After about τ_{scc}, globally, the potential does not change much anymore.

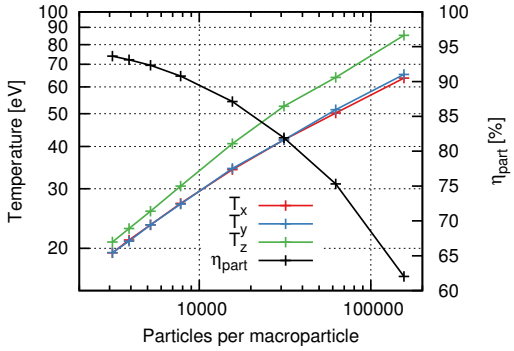

(a) Dependence of the electron temperature on the number of macroparticles in the simulation.

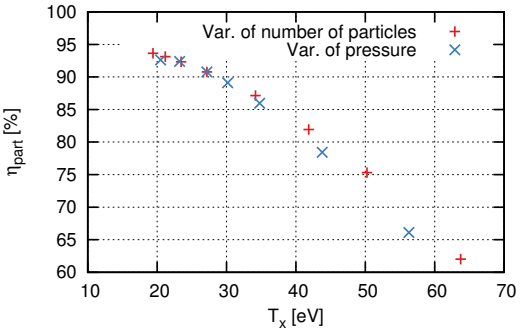

(b) Relation between temperature T_x at the center of the system and the degree of compensation.

Figure 4.17.: Dependence of the compensation degree on the temperature.

increases over time until it can escape the system due to the random error in the electric field. If this is the case, one would assume the results to be dependent on some of the parameters of the PIC simulation, especially the number of macroparticles.

Figure 4.17a shows the dependence of the observed electron temperature (calculated over a slice of particles at the system center) on the amount of charge per macroparticle used in the simulation. When more particles are used to represent the system, the temperatures in all planes are lower and, correspondingly, the average compensation degree of the system changes significantly. If the mechanism responsible would not be of numerical origin, a convergence to some "correct" value for the given geometry and ionization rate should be observed as the system becomes better resolved. This is not the case.

Compared to the number of macroparticles used to represent the beam, the number

of macroparticles used for the electrons only has a minor influence on the temperature. When multiple macro-electrons per proton impact are created instead of one (with the charge divided among them), the observed temperatures only deviate by values below 1.5 % between simulations with up to 5 times as many macro-electrons. When the beam is treated as a static potential and fixed after the steady-state has been reached, the electron temperatures decrease to 11.8 eV. A further decrease to 8.3 eV was observed, when residual gas ions were not included in the simulation.

In the case where residual gas ions were included and the beam potential fixed, the compensation degree does not reach a constant. Instead, electrons and residual gas ions start to accumulate indefinitely at the same location. After 50 µs, when the simulation was aborted, the ratio between electrons and ions had reached values close to 1 at some points in the volume and was still increasing in other parts. This indicates that, if the hypothesis is correct, the fluctuating forces also significantly influence the residual gas ions, driving these from the approximately field free region near the beam axis. At lower temperatures, transversely, the areas of low electric field inside the beam increase. This further amplifies the accumulation.

When the electric field of the beam is replaced by that of a homogeneously charged cylinder and electrons inserted accordingly, the transverse velocities remain Gaussian distributed in the steady state. Varying the total number of macro-electrons inserted per step (proportionally decreasing the charge per particle) from 5 (3×10^5 particles in the steady state) to 150 (9.5×10^6), the temperatures range between 2.65 eV to 1.85 eV. Longitudinally however, the larger the number of macro-electrons, the more the velocity distribution becomes approximately triangular. The second-order moments range from 4.7 eV to 11.3 eV, increasing with the number of particles.

The hypothesis also provides an idea about the origin of the observed Gaussian velocity distributions. It was observed that the remaining electric field around the beam axis becomes relatively low and, correspondingly, that particles move through the beam core in straight lines, see Figure 4.13a. They are then smoothly reflected at some point around the beam edge. If random fluctuations in the field are present, this will lead to a diffusion of the velocities. The energy curves shown in Figure 4.16 could then be interpreted as the result of a random walk due to the fluctuating electric field.

To illustrate this, following the calculation by Einstein [63, §4] for Brownian motion, if the velocity of each particle changes by a random δv in a small step Δt, where the δv are distributed with a function $\phi(\delta v)$, then

$$\begin{aligned} f(v, t+\Delta t) &= \int_{-\infty}^{\infty} f(v+\delta v, t)\, \phi(\delta v)\, \mathrm{d}\delta v \\ &= \int_{-\infty}^{\infty} \left[f(v,t) + \delta v \frac{\partial f(v,t)}{\partial v} + \frac{1}{2}\delta v^2 \frac{\partial^2 f(v,t)}{\partial v^2} + \mathcal{O}\big(\delta v^3\big) \right] \phi(\delta v)\, \mathrm{d}\delta v \\ &\approx f(v,t) + 0 + D\Delta t \frac{\partial^2 f(v,t)}{\partial v^2}. \end{aligned}$$

The first integral over $\phi(\delta v)$ is 1 due to conservation of the numbers of particles, the second 0 if $\phi(\delta v)$ is assumed to be symmetric and the third is defined as the diffusion

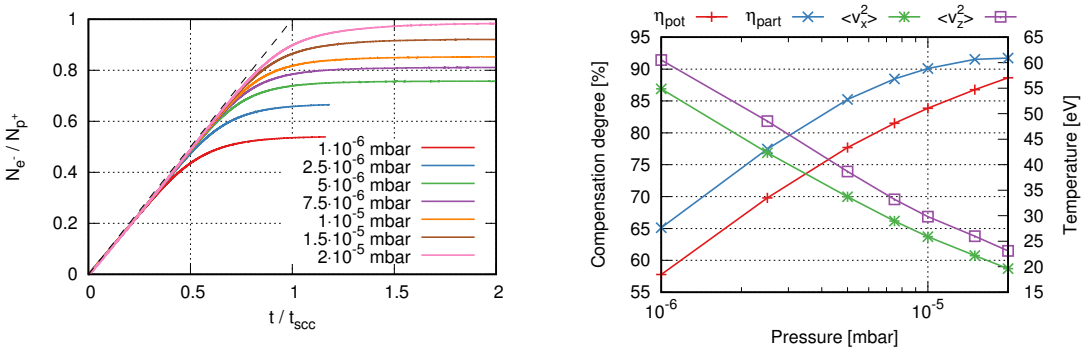

(a) Time dependence for various pressure values.

(b) Compensation degree and temperature for various pressure values.

Figure 4.18.: Results from simulations using an argon background gas at various pressure values in the range of 1×10^{-6} mbar to 2×10^{-5} mbar.

coefficient times the time step $D\Delta t$. Dividing by $\Delta t \to 0$, we get

$$\frac{\partial f(v,t)}{\partial t} = D \frac{\partial^2 f(v,t)}{\partial v^2}.$$

The solution with the initial condition $f(v,0) = n\delta(v)$ is

$$f(v,t) = n \exp\left(-v^2/\left(4Dt\right)\right) / \sqrt{4\pi Dt},$$

i.e. a Gaussian of increasing width. The hypothesis is, that at the point where as many particles diffuse to energies high enough to escape the system as are introduced by ionization, an equilibrium with a stable, approximately Gaussian velocity distribution forms.

Further experiments are needed to understand the formation of the equilibrium as well as its dependence on the number of macroparticles. To do so, a one dimensional model in r could be implemented, where sufficient particle statistics can be achieved more easily. Another possible experiment is using grids with different resolutions for the beam and the electrons—a coarse one for the beam to keep fluctuations to a minimum and a grid fine enough to resolve the Debye length for the electrons. If stochastic heating is in fact the source, use of a higher-order PIC scheme or filtering of the charge distribution could also help reduce the effect.

Physically, a process that drives the velocity distribution towards Maxwellian distributions are particle collisions. For a system of charged particles, these are Coulomb collisions. For these, starting from the Boltzmann equation, [14, p.15ff, p.33ff] derives an equation of Focker-Planck type and shows that for isotropic distributions, the velocity profiles relax towards a Maxwellian. Since the particle-in-cell algorithm solves Vlasov's equation, ideally, these collisions should not be present in the simulations. However, models exist to introduce them into PIC models [64].

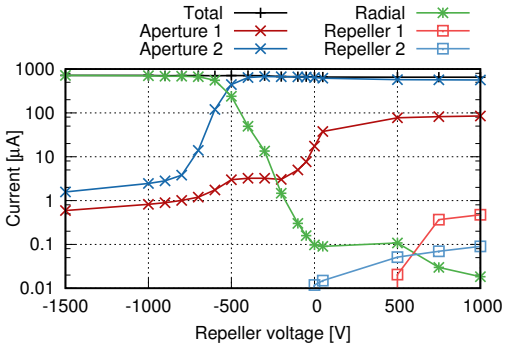

(a) Electron loss current on various elements of the system.

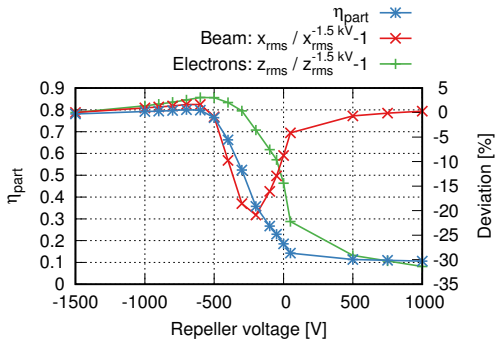

(b) Compensation degree, longitudinal rms size z_{rms} of the electron column and rms beam size for various repeller voltages.

Figure 4.19.: Variation of the repeller voltage.

For collisions between beam particles and electrons, Dölling [45, p. 19] gives an average heating rate per electron for a beam with particle mass m_{b} and charge q_{b}, density n_{b} at velocity v_{b} passing through a thermal electron background with thermal velocity $v_t = \sqrt{2k_{\mathrm{b}}T/m_{\mathrm{e}}}$,

$$P = \frac{e^2}{4\pi\epsilon_0^2 m_{\mathrm{e}}} \frac{n_{\mathrm{b}} q_{\mathrm{b}}^2}{v_{\mathrm{b}}} \ln(\Lambda) \left[\operatorname{erf}\left(\frac{v_{\mathrm{b}}}{v_{\mathrm{t}}}\right) - \frac{2}{\sqrt{\pi}} \left(1 + \frac{m_{\mathrm{e}}}{m_{\mathrm{b}}}\right) \frac{v_{\mathrm{b}}}{v_{\mathrm{t}}} \exp\left(-\left(\frac{v_{\mathrm{b}}}{v_{\mathrm{t}}}\right)^2\right)\right]. \tag{4.22}$$

For the given system, $P = 19.5\,\mathrm{keV\,s^{-1}}$, increasing slightly for colder electron temperatures and towards lower beam energies. The magnitude of this rate is roughly equal to those that were observed in the test system in Section 3.4.1 at parameters in the same order of magnitude. Therefore, the numerical influence needs to be better understood before processes such as Coulomb collisions are implemented.

4.3.5. Variation of parameters

Simulations at different background gas pressures in the range from $1 \times 10^{-6}\,\mathrm{mbar}$ to $2 \times 10^{-5}\,\mathrm{mbar}$ were made. Figure 4.18 shows the development of the electron to proton ratio over time as well as some parameters in the steady state. Changing the pressure proportionally changes the production rate of electrons. Initially, in all cases their number increases linearly with the production rate. At lower gas pressures, the curves start to deviate from this behaviour earlier.

The simulations show a significant dependence of the compensation degree as well as the velocity distribution of the electrons on the gas pressure. It could be speculated that the dependence of the temperature is of numerical origin as a result of the lower number of simulation particles. If this were the case, the values of T should be similar at equal number of macroparticles. However, this is not the case, since the influence of the electrons on the final temperature was found to be small. For $p = 5 \times 10^{-6}\,\mathrm{mbar}$, this was checked

again by producing multiple macroelectrons per ionizing collision. At double the number of macroelectrons (i.e. more than for $p = 1 \times 10^{-5}$ mbar), the reduction in temperature (0.6 eV) is much smaller than the difference between the results for 5×10^{-6} mbar and 1×10^{-5} mbar in Figure 4.18b.

The results from the pressure variation hint at a connection between the temperature and the loss rate, which in steady-state has to be equal to the electron production rate. The system finds a state, in which enough particles are transported into the tail of the Boltzmann distribution and are lost. The relation between temperature and the amount of charge in simulations with different gas pressures as well as different number of macroparticles in Figure 4.17b is quite similar. There appears to be some commonality between the effects of an increased level of numerical fluctuation and an increased number of new, potentially low-energetic electrons being created.

Figure 4.19a shows the currents of electrons flowing onto various parts of the system when the repeller voltage U_{rep} is reduced. Particles escaping the system longitudinally through the apertures at the system entrance (denoted by "1") and exit ("2") are considered as lost. Experimentally, such a situation would need to be created, for example by two electric dipole fields to make sure electrons do not return through the aperture. At high negative voltages, only electrons formed inside the electrodes with sufficient energy and correct initial direction can escape. Except for this tiny fraction, all other electrons hit the beam pipe.

When the repeller voltage is decreased from −1.5 kV to −600 V, the compensated area of the beam as well as the amount of negative charge in the system increases slightly. In the simulations at repeller voltages between −800 V to −500 V, the electron current flowing through the second aperture increases nearly by an order of magnitude per 100 V increase. Initially, the electrons only escape the system on the axis, where the potential is highest. At −500 V, longitudinal losses start to dominate the radial losses. At this point the compensation starts to decrease significantly as can be seen in Figure 4.19b. Once this occurs, there is an additional influence from the beam focus moving towards the second repeller, which additionally weakens the confinement by an increase of beam potential due to its smaller size. The movement of the focus and the resulting asymmetry is also responsible for the current through aperture 1 remaining constant in the range between −500 V to −200 V.

Simulations with positive "repeller" voltages were made. Even at high positive values, the system is never completely decompensated. At $U_{\mathrm{rep}} = 500$ V, a charge density of 200 µC m^{-3}, about a fifth of the value at −1500 kV, was found to be confined within the potential well of the focus. The currents onto the repeller remain quite low, even when their potential is larger than the beam potential. Most of the electrons are accelerated through the aperture by the electric field.

4.4. Simulation using the Poisson-Boltzmann equation

In Section 4.3.3, it was found that the electron energies in the *bender* simulation are approximately Boltzmann distributed. This made it possible to predict their distribution

using the total charge contained in a slice of particles, their temperature and the potential extracted from the *bender* simulation. Given the two parameters temperature T and compensation charge density ρ_{comp}, the potential can also be found directly. Inserting the expression for the electron density into Poisson's equation, we have

$$\nabla^2\varphi(\mathbf{r}) = -\frac{1}{\epsilon_0}\left(\rho_{\mathrm{beam}}(\mathbf{r}) + \rho_{\mathrm{comp}}\exp\left(\frac{e\varphi(\mathbf{r})}{k_{\mathrm{b}}T}\right)\right). \tag{4.23}$$

In Section 3.4.1, a method to solve the Poisson-Boltzmann equation (4.23) was explained. The following section will focus on its application on space charge compensation of proton beams. Similar calculations where already made for example in [65].

To calculate the influence of the electron distribution on the beam, the solution of Poisson's equation in a code such as *tralitrala* can be replaced by the solution of (4.23). Given the longitudinal distribution of the temperatures and the compensation degree from the PIC simulation, this makes it possible to compare the results to those of the much simpler model.

4.4.1. Profiles

Figure 4.20 shows the solutions to (4.23) for a homogeneous beam of 1 cm radius for a compensation degree η_{part} of 50 % and 95 %. The figure gives both the dimensionless scaled quantities as well as the potential and the electric field for a beam with the same parameters as were used in the *bender* simulations. For beams of, for example, lower current, these quantities will have the same distribution if the given temperatures are also decreased by the same fraction.

Figure 4.21 shows the emittance growth of a homogeneous and a Gaussian beam, both initially parallel, transported over 50 cm including the compensation electrons at different temperatures and compensation degrees η_{part}.

For Debye lengths small in comparison to the size of the confining beam, the electron density follows that of the beam closely and drops off rapidly at the edge. This behaviour leads to a constant potential and zero electric field in the beam core. If the compensation degree is high, the influence of the space charge is mostly removed. If η_{part} is significantly smaller than 1, a part of the beam outside some radius remains largely uncompensated. This leads to an approximately linear increase of the electric field at the beam edge. Therefore, the beam density at lower radii will remain unchanged. However, particles at the edge will be pushed outwards, leading to a decrease in density.

Even a small amount of "cold" electrons lead to an emittance increase of a few percent: at $kT = 2\,\mathrm{eV}$ and $\eta_{\mathrm{part}} = 6\,\%$, $\Delta\epsilon_{\mathrm{rms}}/\epsilon_{\mathrm{rms}} = 2\,\%$. From Figure 4.21a, we find that values of η_{part} around 35 % for cold electrons lead to the highest emittance growth: $\Delta\epsilon_{\mathrm{rms}}/\epsilon_{\mathrm{rms}} = 14\,\%$ for $kT = 2\,\mathrm{eV}$. This last case—cold electrons but a low compensation degree—only occurred in the *bender* simulations when the potential on the repellers was reduced to values in the order of the remaining potential or even set to positive values, i.e. electrons were allowed or even forced to escape the system.

At higher temperatures, more electrons have enough energy to move to areas at lower

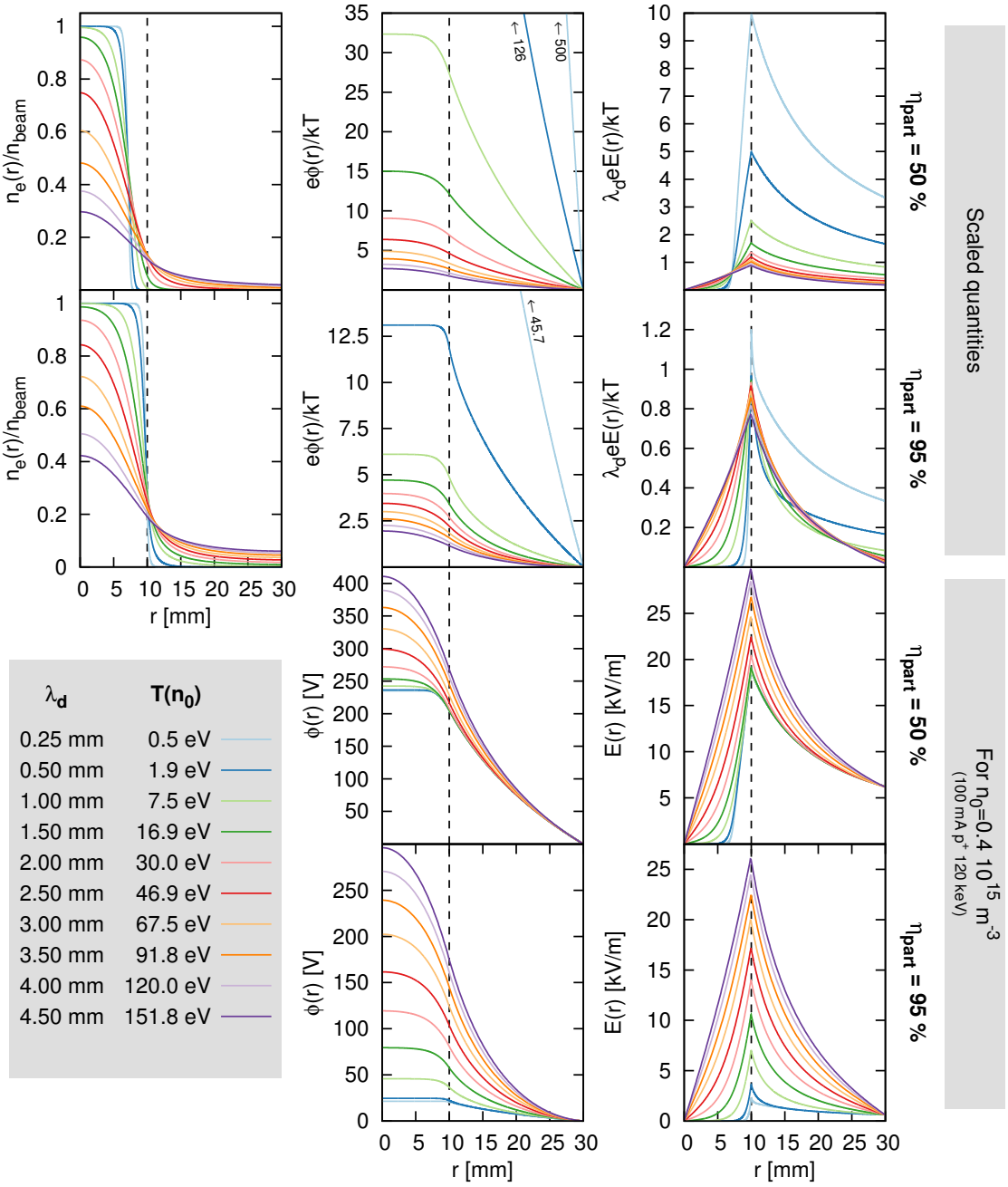

Figure 4.20.: Solution of the Poisson-Boltzmann equation for a homogeneous beam of 1 cm radius compensated by $\eta_{\mathrm{part}} = 50\,\%$ or $\eta_{\mathrm{part}} = 95\,\%$. The upper row of figures shows the dimensionless scaled quantities for various Debye lengths λ_d, the lower row the potential and electric field for a 100 mA, 120 keV proton beam at the electron temperatures given in the caption.

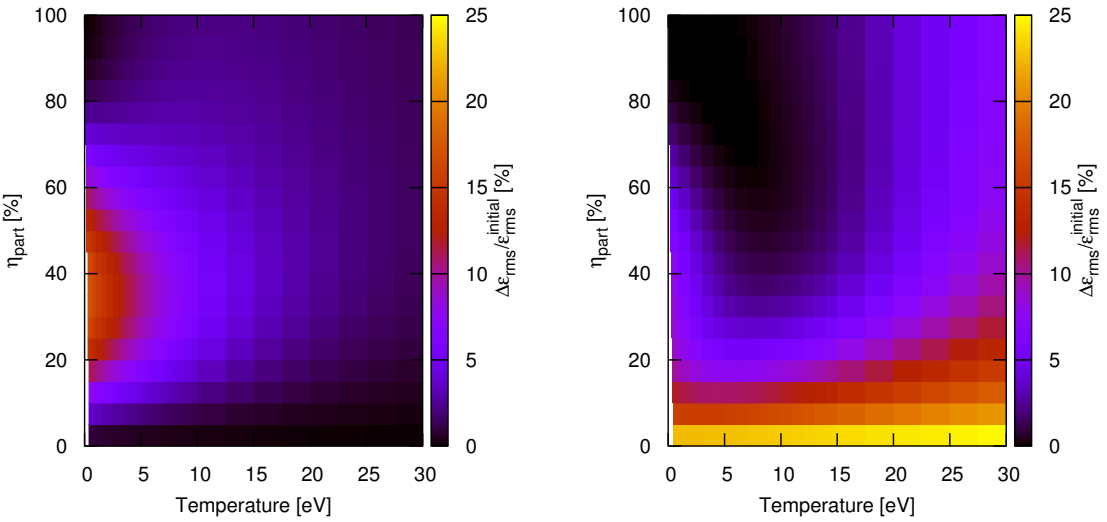

(a) KV distribution.

(b) Gaussian distribution (cut-off at 3σ).

Figure 4.21.: Emittance growth of a parallel beam ($I = 50\,\mathrm{mA}$, $\epsilon_{\mathrm{rms}} = 25\,\mathrm{mm\,mrad}$, $\alpha = 0$, $\beta = 1\,\mathrm{m}$) after 50 cm transport including thermally distributed compensation electrons. In the remaining white areas the solver diverged.

potential and thus the electron distribution extends to higher radii. This leads to a non-linear field over wide areas of the beam, which in turn causes an emittance growth. While at intermediate values of the compensation degree, the effect of these non-linearities is not as pronounced as the effect of the sharp increase at the edge, for $\eta_{\mathrm{part}} \approx 1$, their result can be seen in the increasing emittance at higher electron temperatures.

Towards high electron temperatures, the emittance growth decreases again in all cases. There, the electron distribution becomes very spread out, tending towards a homogeneous distribution reaching up to the aperture. Such a homogeneous background, while not very effective at compensation, does not produce any non-linearities in the electric field and thus doesn't lead to emittance growth. In such a configuration however, the radial electron loss current would become very large and would need to be compensated by a large rate of electron production. In the *bender* simulations, such a state was not found.

The observed growth also depends on the beam parameters. If the beam is matched in the same way as in the *bender* simulations, i.e. with a focus in the center of the system, the simulations predict a large emittance growth at higher electron temperatures for intermediate values of η_{part} as well.

In addition to a homogeneous beam, an rms equivalent beam following a Gaussian distribution was transported in the same way. The emittance growth, shown in Figure 4.21b, differs significantly from the homogeneous case. The highest growth is observed for the uncompensated beam. This is caused by the relaxation of the non-linear field

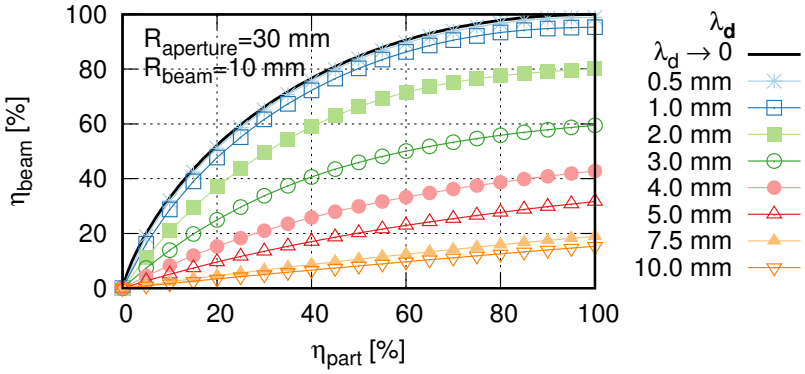

Figure 4.22.: Relation between the two definitions of space charge compensation degree in (4.1) and (4.2).

energy contained in the Gaussian distribution [16, p. 426]. The simulations show a reduction in emittance growth from 27 % to below 10 % going from no compensation to low compensation values above 15 %, nearly independent on electron temperature. Another difference in the plots of Figure 4.21 is the low emittance growth observed in the simulation of the Gaussian beam around $T = 8\,\mathrm{eV}$, $\eta_{\mathrm{part}} = 60\,\%$. In this case the confined electrons distribute in such a way that the total electric field becomes linear over wide parts of the beam.

The assumption of a thermal electron distribution also makes it possible to link the two definitions of the space charge compensation degree as defined per reduction of line charge density in (4.1) and per reduction of the potential difference between beam edge and center in (4.2). The relation is shown in Figure 4.22.

For Debye lengths long in comparison to the beam radius, the behaviour is close to linear, however with slopes much less than one. For low values of λ_d, initially, the potential on the axis reduces faster than η_{part}, since the electrons overproportionally populate the area around the axis. As the amount of the electron charge increases in the system, the increase in η_{beam} is reduced as more and more electrons have enough energy to distribute the area outside the beam. For vanishingly small Debye lengths, the charge density is that of a hollow beam. This allows us to find an analytical relation between η_{beam} and η_{part},

$$\eta_{\mathrm{beam}} = (1 - \log(\eta_{\mathrm{part}}))\,\eta_{\mathrm{part}},$$

which nicely fits the numerical result for $\lambda_{\mathrm{d}} \to 0$.

4.4.2. Comparison to the *bender* simulation

In Section 4.3, various features in the distribution of the beam and the secondary particles were identified. To investigate whether these effects can be explained by the presence of the thermalized electrons, the temperature distribution (Figure 4.11h) and fraction of charge η_{part} (Figure 4.11g) from the *bender* simulations were imported into *tralitrala* and the radial distribution of the electrons calculated from the Poisson-Boltzmann equation as in the preceding section. Such a simulation does not contain the influence of the residual

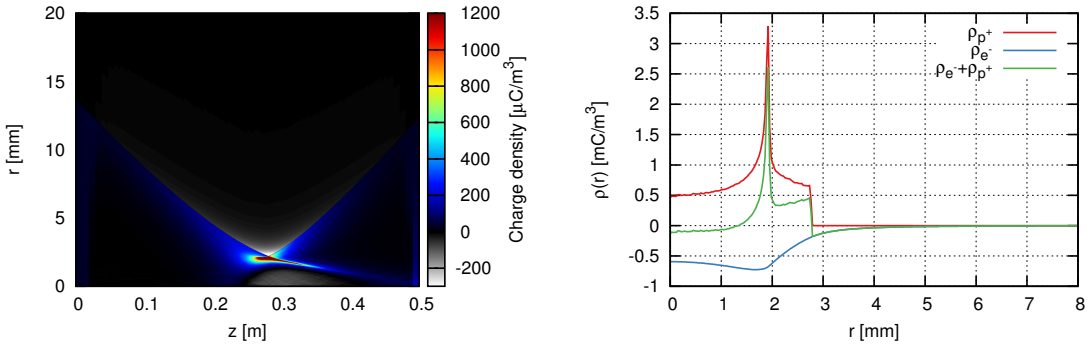

(a) Net charge density.

(b) Radial density distribution at $z = 0.3\,\mathrm{m}$.

Figure 4.23.: Simulation of the drift system using *tralitrala* with thermally distributed electrons. The longitudinal distribution of temperature and compensation degree was imported from the PIC simulation.

gas ions and any effects caused by the velocity distribution of the compensation electrons in longitudinal direction.

The resulting total charge density is shown in Figure 4.23a. The formation of the hollow beam clearly occurs in a similar way as in the 3d simulation. It is a result of the sharp increase of the electric field at the edge of the beam. There, these fields reduce the angles of the particles. In the xx' projection, areas of higher density form towards lower angles x' for negative horizontal offsets x and towards higher angles for positive x. These continue to form the large peak in density in the focus—Figure 4.23b shows a cut in radial direction at 30 cm—and continue on towards the axis. They are still visible in the final output distribution of the system shown in Figure 4.24 at the edges of the ellipse close to the axis.

The kurtosis of the beam distribution changes significantly during transport. It increases to 2.15 at $z = 22\,\mathrm{cm}$ in front of the focus, then drops to 1.75 6 cm later in its center, afterwards increasing to its final value of 2.26. During the build-up of compensation, this effect shows up in the final distribution of the beam as formation of a hollow beam after about 6 µs of simulation. As the beams focus shifts backwards, the areas of higher density appear at the edge of the beam in the final distribution, leading to a short drop in kurtosis.

The beam distributions from both simulations are shown in Figure 4.24. They have equal rms dimensions and orientation in phase space. The emittance growth is larger in the simulation using the Poisson-Boltzmann model. This could be a result of the much larger grid resolution. Peaks in the distribution, such as present in Figure 4.23b, could not be resolved by the 0.4 mm grid in the *bender* simulation.

In Figure 4.23 a negative net density is predicted around the beam axis in the focus, as a result of the increased potential well of the sharp peak at the edge of the beam. In the model simulations, this leads to a negative electric field near the axis. This is only possible when the residual gas are excluded. These would become trapped due to

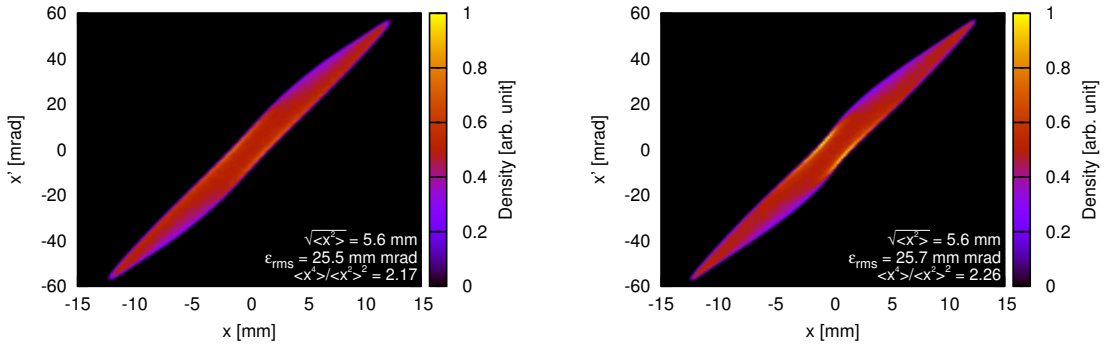

(a) *bender*. (b) *tralitrala*.

Figure 4.24.: Beam distribution from *bender* compared to the simulation with thermally distributed electrons.

the negative electric field, filling up the potential well. This is the reason for the ion accumulation in the area of the focus observed in the *bender* simulations. Equally, a negative radial electric field near the axis was observed in the *bender* simulation, where the beam was treated as static and the residual gas ions ignored.

Compared to the PIC simulation, the used CPU time is reduced by about three orders of magnitude. Thus, if the inputs used for the 1d simulation—temperature and compensation degree distribution—could be predicted by some other means, the effects on the beam could be calculated at severely reduced cost.

5. Applications

5.1. Particle-in-cell simulations for the IOTA electron lens

In free space, the fields from magnetostatic as well as electrostatic lenses can be calculated from scalar potentials which have to satisfy the Laplace equation [66, p. 195]. For applications where fields are needed which do not fulfill this requirement but which satisfy Poisson's equation, use of an electron lens is a possible choice [67]. An important example are fields pointing mainly in radial direction. In an electron lens, a low-energy beam of electrons with high intensity is guided by strong magnetic fields, either alongside or superimposed on another beam.

Two electron lenses were used at the Tevatron at Fermi National Accelerator Laboratory (FNAL) [68] for experiments on hollow-beam collimation [69] and abort-gap cleaning [70]. At Brookhaven National Laboratory, two electron lenses are under operation to compensate the tune spread due to beam-beam effects [71], previously also investigated at FNAL [72]. For the LHC, an electron lens is being considered for halo control using hollow beams [73].

Figure 5.1 shows a schematic of one of the lenses used at the Tevatron [68]. A beam of up to 3 A is produced at the gun, which is biased to the wanted beam energy between 5 keV to 10 keV. It is located inside the magnetic field produced by the gun solenoid. From there, the beam is guided onto the axis of the circulating beam by magnetic fields produced by three additional coils. An increase in the magnetic field, from $B_{\text{gun}} = 0.3\,\text{T}$ to $B_{\text{main}} = 3.1\,\text{T}$ inside the superconducting main solenoid, compresses the beam to $c = \sqrt{B_{\text{gun}}/B_{\text{main}}} \approx 32\%$ of its radius at the gun. After interacting with the circulating beam, the electron beam is guided into a collector.

By shaping the electrodes of the electron gun, the current-density profile of the electron

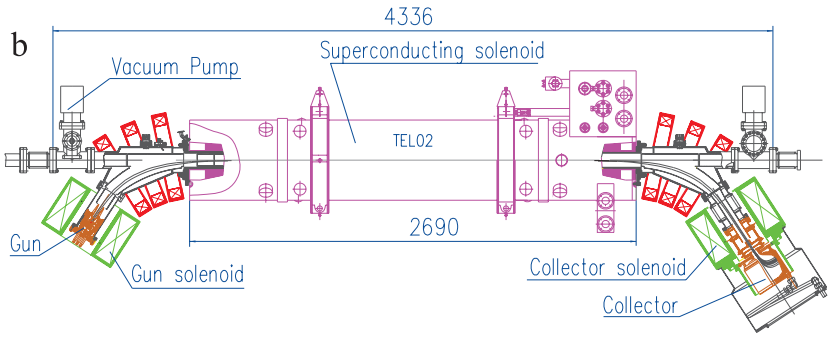

Figure 5.1.: Schematic drawing of the TEL2 lens at the now defunct Tevatron [68].

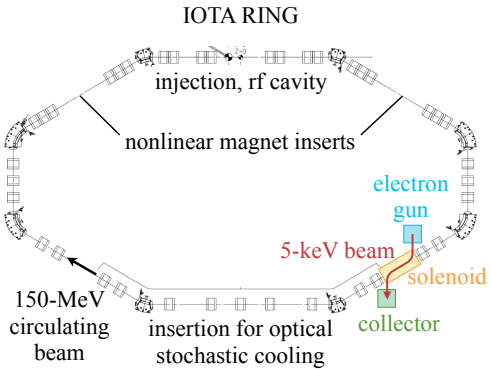

(a) Schematic of the IOTA ring including the electron lens [76].

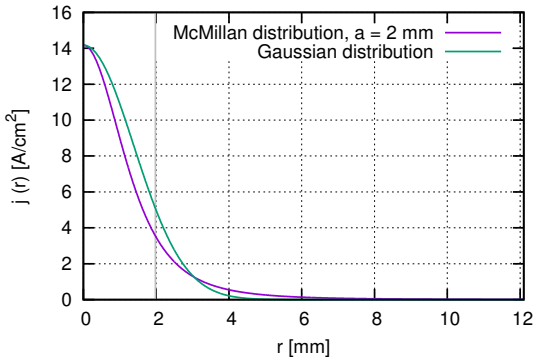

(b) McMillan distribution in comparison to a Gaussian with equal current and current density on axis.

Figure 5.2.: Schematic of the ring and the required current density distribution.

beam can be controlled. Ideally, this profile should be preserved during the transport. However, distortions in the magnetic field as well as effects from space charge can lead to changes in the distribution. *bender* was used to investigate the dynamics in a proposed new electron lens for the Integrable Optics Test Accelerator storage ring currently being built at FNAL. The contents of this section is also focus of [74].

5.1.1. IOTA at the Fermi National Accelerator Laboratory

In the ideal case, the beam dynamics of conventional circular accelerators is completely linear, i.e. the forces of all optical elements depend linearly on the particle's offset from the axis. In that case, all particles oscillate around the axis with the same frequency (or tune), independent on their amplitude. However, in such a system, errors in the external fields can drive resonances, which lead to emittance growth and beam loss. Additionally, sextupoles—with a force proportional to the square of the offset—are often added to an accelerator lattice to correct for effects due to the energy dependence of the focusing (chromaticity correction, [37, p. 439]). Another non-linear force comes from space charge. However, any non-linearity added decreases the region of phase space where the motion of particles is regular and non-chaotic (dynamic aperture).

A new approach will be investigated as an experiment at the Integrable Optics Test Accelerator (IOTA) at the Fermi National Accelerator Laboratory. The idea is to intentionally introduce a non-linearity in a way that particle motion remains integrable. The result should be a large tune spread, which is expected to provide improved stability properties [75]. IOTA is a storage ring with 40 m diameter that will provide space for several possible non-linear inserts. One of these inserts is an electron lens, which will be placed at the location shown in Figure 5.2a.

Two ways to achieve an integrable beam dynamic with a large tune spread will be

investigated at IOTA. The first option requires a current profile following

$$j(r) = \frac{I}{\pi}\left(1 + \frac{a^2}{R_\mathrm{b}^2}\right)\frac{a^2}{\left(a^2 + r^2\right)^2},$$

where I is the beam current, a an effective radius and R_b a cut-off radius (ideally $R_\mathrm{b} \to \infty$). The properties of a mapping with kicks produced by a current density such as this was studied first by McMillan in one dimension and extended to two dimensions in [77]. Reference [76] lists the requirements on the electron lens beam for this case: at $B = 0.33\,\mathrm{T}$ main solenoid field and 24 mm ring aperture, $a = 3.6\,\mathrm{mm}$ at the cathode and $a = 2\,\mathrm{mm}$ inside the main solenoid. For a beam energy of $E = 5\,\mathrm{keV}$ and copropagating beams, the current has to reach $I = 1.7\,\mathrm{A}$ to achieve a tune spread larger than 0.25. The required current density inside the main solenoid is displayed in Figure 5.2b.

The second option is to focus the circulating beam using the electron lens main solenoid. At a setting of $B = 2(B\rho)/\beta$ the beta functions in both directions are constant and any radially symmetric current distribution leads to an integrable dynamic for phase advances that are multiples of π in the rest of the ring.

5.1.2. Initial coil design

Figure 5.3 shows the magnetic fields as well as the coil design for the injection part of the electron lens to be investigated. The design was found using a Python script written specifically for this purpose, which includes a Biot-Savart solver for cylindrical coils and an algorithm for tracking the magnetic field lines.

The length of the normal conducting main solenoid was chosen to be 1 m. The current IOTA lattice design then only leaves 30 cm on each side between the main solenoid and the adjacent quadrupole magnets. This necessitates an increase of the angle of injection from 57° for TEL2 (where about 80 cm were available) to 70°. The design reuses the electron gun and collector magnets from TEL2. These can reach fields up to 0.4 T, but only 0.1 T are required for the desired compression when the main solenoid is operating at its nominal value 0.33 T.

Solenoid	R_i [cm]	R_o [cm]	B [mT]	j [A/mm^2]	Θ [°]	Center [m]
Gun	12.5	23.7	100	1.11	70	(0.517, 0.828)
Transfer	3.5	7.5	100	2.27	70	$r_\mathrm{trans} = (0.2114, 0.717)$
Bend 1	9.65	13.65	53.9	6.28	43	$r_\mathrm{bend,1} = (0.02692, 0.682)$
Bend 2	6.33	10.33	74.9	6.28	33.5	$r_\mathrm{bend,2} = (0.0118, 0.615)$
Bend 3	4.17	8.17	100	6.28	24	$r_\mathrm{bend,3} = (0.0, 0.5555)$
Main	2.5	10	330	3.53		(0.0, 0.0)

Table 5.1.: Dimensions and magnetic field settings of the initial bend design under investigation. R_i and R_o are the inner and outer diameters of the coils and θ the angle between their axis and the direction of the propagating beam.

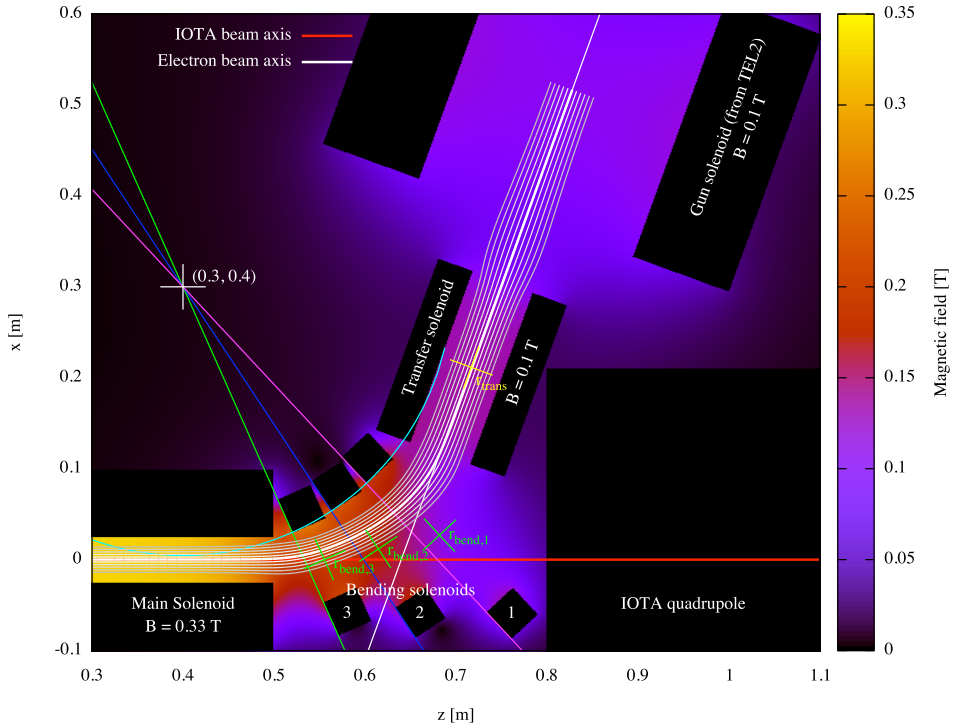

Figure 5.3.: Initial bend design for the IOTA electron lens. The dimensions as well as the current settings of the solenoids can be found in Table 5.1.

As in TEL2, three smaller coils generate the magnetic field to guide the beam from the source into the main solenoid. Their inner, frontal edges were placed on a circle. The radius of 295.6 mm and the center of the circle were found trying to increase the field homogeneity in the bending region. For the geometry investigated here, the three solenoids operate at equal current. This makes operation with one power supply possible. Due to the different sizes, the bending solenoid closest to the gun only produces 54 % of the magnetic field of the last solenoid on its axis, the second one only 75 %. At the chosen dimensions, the solenoids can be operated at up to 159 mT (in the first solenoid) to stay below the value given as "good" in [78, p. 113] for water-cooled coils.

Due to the increased distance between gun and bending solenoids, an additional "transfer" magnet had to be included.

Figure 5.4a shows two field lines with an offset of ±25 mm projected to the field line starting at the center of the gun solenoid for different currents through the bending solenoids. In the figure, the magnetic field strength produced by the third and last bending solenoid is given. Compared to the case where the currents through the bending solenoids are chosen so that all produce a field of 100 mT (dashed line), the beam in the current design has a larger size, especially in the first bending solenoid.

Towards the center of bending solenoid 1, the magnetic field decreases. This leads to the asymmetry between the positive and negative horizontal direction, clearly visible in

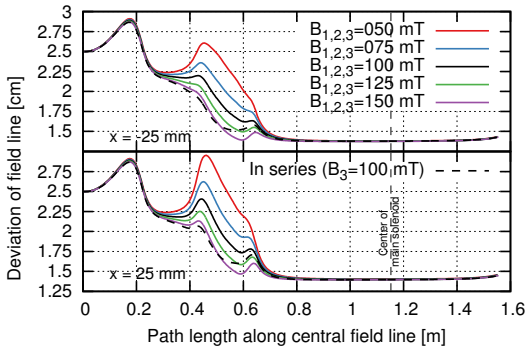

(a) Deviation from the central field line for two lines starting inside the gun with an offset of ±25 mm.

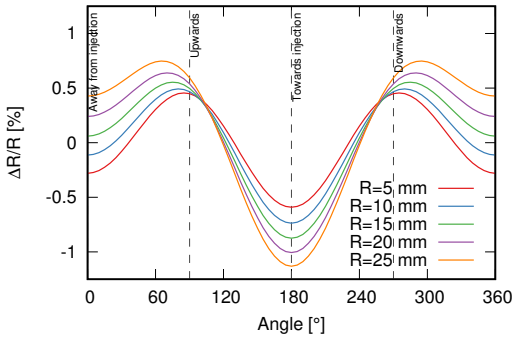

(b) Deformation of field lines starting at different radii at the source, measured at the center of the main solenoid.

Figure 5.4.: Deformation of the field lines.

Figure 5.4a, which can be as high as 3 mm. The short increase in beam size in front of the main solenoid is a result of the field drop between bending solenoid 3 and the main solenoid.

In a system symmetric around the axis, field lines starting on a circle with radius R at a field of B_1 should be compressed by a factor of $\sqrt{B_1/B_2}$. Figure 5.4b shows the deviation for the field configuration in Figure 5.3 inside the main solenoid. Due to stray fields from the bending section, the compression ratio is slightly higher than from the field values produced by the magnets alone: 55.7 % ($B_{\text{gun}} = 102.9\,\text{mT}, B_{\text{main}} = 331.3\,\text{mT}$) instead of 55 % ($B_{\text{gun}} = 0.1\,\text{T}, B_{\text{main}} = 0.33\,\text{T}$).

At lower radii, the deformation is mainly quadrupolar i.e. the compression is slightly higher on the horizontal axis than it is in vertical direction. With increasing radius, the influence of the asymmetry in the injection in horizontal direction becomes visible. Field lines with negative offset, i.e. those starting with offset towards the injection, end up at lower radii than those starting away from the injection. The shift of the maxima in both downwards and upwards direction is a result of the field lines being slightly shifted in horizontal direction. In total, the deformation of a circle starting at the gun at $R = 25\,\text{mm}$ is as large as 0.26 mm.

For the placement of vacuum equipment, some space not covered by a coil is needed. This space can be provided between the gun and the transfer solenoid. Figure 5.5a shows the deformation of the field lines for various distances between the magnets. As long as the aperture is designed wide enough, increasing the distance from its current value of 12.5 cm should not pose a problem.

Due to the long range of the magnetic field of the coils, the magnetic field on the surface of the cathode does not perfectly point in the geometric direction of injection but at a slightly increased angle $\varphi' = 70.027°$. The angle of the magnetic field also depends on the horizontal offset by $-94\,\mu\text{rad}\,\text{mm}^{-1}$ and on the vertical offset by $280\,\mu\text{rad}\,\text{mm}^{-1}$.

A similar configuration of magnets, with the gun replaced by a beam dump, is placed on the opposite side of the lens to guide the electron beam out of the path of the circulating

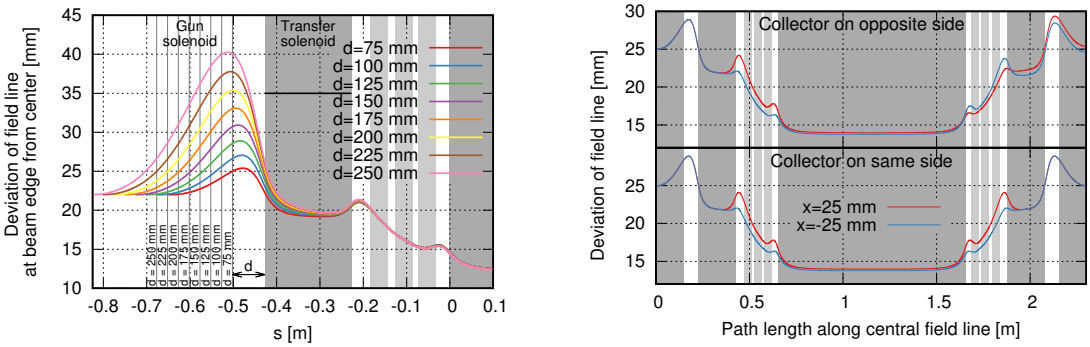

(a) Field lines for various distances between gun and transfer solenoid.

(b) Comparison of field lines between the configuration with the collector on the same side as the injection as well as on the opposite side.

Figure 5.5.: Field line tracking for various design choices.

beam. The configuration can either be mirrored at the central plane, guiding out the beam towards the same side of the ring it was injected from, or can be inverted to guide out the beam towards the other side. The two options differ in the disturbance on the circulating beam.

In the bends, there is a kick in vertical direction due to the horizontal component of the guiding fields. For the present design, on the axis of the lens, the kick on 150 MeV electrons is 31 mrad in each bend. These kicks cancel for the former option due to the different direction of the horizontal magnetic fields in the two bends. If the electron beam is guided out towards the other side of the ring, the kicks accumulate. The downside of the mirrored configuration is the accumulation of the horizontal kicks from the electric field of the lens beam on the circulating beam. Compared to the kick from the magnetic field, these are small: 5.6 µrad per bend on the axis for a 1.7 A McMillan beam calculated from the simulation in Section 5.1.4.

When the collector is placed on the opposite side of the electron gun, the magnetic field lines are not symmetric. This can be observed in Figure 5.5b, which shows the outer field lines for both options. With the collector on the opposite side, field lines starting at ±25 mm at the cathode end with an offset of 25.4 mm and 24.6 mm from the geometric collector center.

The design presented here as well as in [74] uses the configuration with gun and collector on opposite sides. However, the layout was recently changed back to the "classical" mirrored configuration. The impact of this choice on the coil configuration in Table 5.1 and on the the considerations in this section are minor.

5.1.3. Single particle dynamics

Particles do not follow the field lines exactly. Their trajectories will always exhibit some drift. In TEL-1, the curvature of the trajectories resulted in several millimeters of

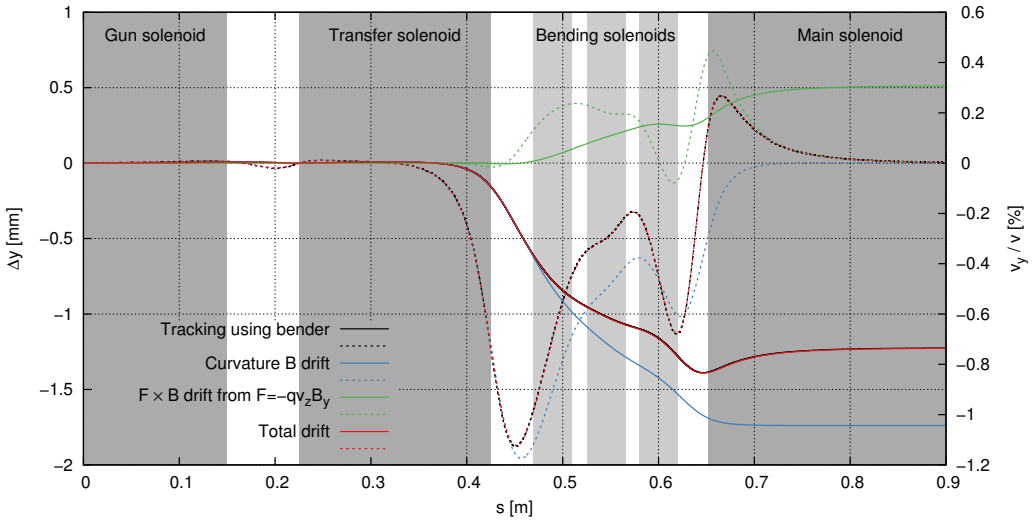

Figure 5.6.: Drift of a particle starting at the center of the cathode. Particle tracking using *bender* and the integration of (5.2) produce the same results. The green and blue curves were calculated by separately integrating the two terms in (5.2). Dashed lines are the velocities, solid lines the offsets.

downward drift [68]. Due to the inhomogeneities in the field, particle drifts could result in significant distortions and were therefore investigated.

The guiding center of a particle can be followed by integrating

$$\frac{\mathrm{d}\mathbf{r}}{\mathrm{d}s} = \pm\frac{1}{B}\left\{\mathbf{B} + \frac{m}{qv_0}\frac{1}{B^2}\left(v_{||}^2 + \frac{1}{2}v_{\perp}^2\right)(\mathbf{B}\times\nabla B)\right\}, \tag{5.1}$$

where v_0 is the absolute particle velocity and $v_{||}$ and $v_{\perp}$ are the components parallel and perpendicular to the magnetic field. Since particles at the cathode start with negligible transverse velocity $v_{\perp}$ and thus magnetic moment, the corresponding gradient B drift can be ignored. The remaining term proportional to $v_{||}^2$ is the drift due to a curvature in the field lines.

Equation (5.1) can be integrated and rewritten using the local radius of curvature $R(s)$,

$$\Delta y(s) = \int_0^s \left\{\frac{2U}{v_0}\frac{q}{|q|}\frac{1}{R(s')\,B(s')} + \frac{B_\mathrm{y}(s')}{B_\mathrm{z}(s')}\right\}\mathrm{d}s'\,. \tag{5.2}$$

Since the drift has a dependence on the sign of $R(s)$, when the collector is placed on the opposite side of the gun, most of the curvature B drift will cancel.

Particles were also tracked using *bender*. Time steps of 5 ps ($\omega_\mathrm{c}\Delta t \approx 0.09$) were found to be sufficiently small. The magnetic field was calculated from a grid of field values with a resolution of 0.5 mm. Care had to be taken not to truncate the fields in the region of the beam to avoid visible effects on the particle motion.

Figure 5.6 shows the drift of a particle starting at the center of the cathode. The

resulting downward drift predicted by integrating only the curvature B drift is $-1.7\,\mathrm{mm}$, but results from particle tracking just predict a drift by $-1.2\,\mathrm{mm}$. This reduction is caused by the guiding effect of the magnetic field (the second term in (5.2)), which counters the drift once the particle has reached some offset from the axis.

The drift velocity in Figure 5.6 shows two maxima: between the transfer solenoid and the first bending solenoid and in front of the main solenoid. Both a lower curvature as well as a lower absolute magnetic field are responsible for the much stronger drift in the first of these two segments.

The downward drift differs by about $5\,\mu\mathrm{m\,mm^{-1}}\Delta x$ for particles with an horizontal offset Δx due to the inhomogenous magnetic field in the bending region. This tilts the final distribution slightly. For particles with larger positive offset $\Delta x > 10\,\mathrm{mm}$, i.e. those on the trajectories closer to the center of the bending solenoids, the change in drift deviates from linear behaviour and becomes as large as $134\,\mu\mathrm{m}$ for a particle with $\Delta x = 25\,\mathrm{mm}$.

5.1.4. Dynamics including space charge

Main focus of the investigation of the electron lens was to better understand the dynamics under space charge and any aberration in the beam distribution that might occur. For this purpose, PIC simulations of the IOTA electron lens were made using *bender*.

The electron gun was not included in the simulation. Instead, the potential on the boundary of the computational volume was fixed to that of an infinitely long beam. This should be a valid approximation, since the beam size does not change much inside the gun solenoid. The three-dimensional Poisson solver described in Section 3.2.2 was used. A beam pipe geometry was included as boundary condition. The radius of the pipe was set to the inner diameter of the solenoids, ignoring wall thickness. Any effects occurring due to this should be investigated once a final design of the lens is found. Using CAD software, a beam pipe with constant curvature and 6 cm inner diameter was included in the bending region.

Simulations with two levels of resolution were made: a "low resolution" version using 100 particles inserted per step (about 430000 in total), 1 mm mesh resolution (3.6 million degrees of freedom) on 16 processors and a "high resolution" version using 2500 particles per step (10 million in total), 0.5 mm mesh resolution (21.3 million dof) on 192 processors. On the Fermilab Wilson cluster [79], the low resolution runs[1] took about 20 h and the high resolution runs[2] approximately 9 h.

Motion

For a homogeneous distribution, including space charge, the particle dynamics in electron lenses is given by the behaviour described in Section 2.2 for zero angular velocity $\omega_\mathrm{r} = 0$. Particles are accelerated outwards by the electric field until the magnetic force due to

[1] on the amd32 partition: AMD Opteron 6134 2.3 GHz
[2] on the intel12 partition: Intel Xeon X5650 2.67 GHz

their increasing velocity is able to balance the push of the electric field. This motion will modulate the envelope of the beam.

During the motion, the angular component of the Lorentz force results in a rotation of the particle around the axis. On average, the velocity of this rotation will be the E×B velocity

$$\omega_{\mathrm{E\times B}} = \frac{v_\varphi}{r} = \frac{1}{q}\frac{q\left(\mathbf{E}\times\mathbf{B}\right)_\varphi}{B^2} = \frac{1}{2\pi\epsilon_0}\frac{I}{v_\mathrm{b}}\frac{1}{R_\mathrm{b}^2}\frac{1}{B}.$$

As long as the velocity v_b does not change significantly, the rotation frequency is constant during a compression, since $R_\mathrm{b}(s) = \sqrt{B_0/B(s)}R_0$ and thus

$$\omega_{\mathrm{E\times B}} = \frac{1}{2\pi\epsilon_0}\frac{I}{v}\frac{1}{R_0^2}\frac{B(s)}{B_0}\frac{1}{B(s)} = \frac{1}{2\pi\epsilon_0}\frac{I}{v}\frac{1}{R_0^2}\frac{1}{B_0}.$$

For an electron beam with $I = 2\,\mathrm{A}$, $R_\mathrm{b} = 2\,\mathrm{cm}$ and $W = 5\,\mathrm{keV}$, the beam will rotate with $\omega_{\mathrm{E\times B}} = 3.4\,\mathrm{MHz}$. This amounts to a rotation of 33° from the gun to the center of the main solenoid.

In Section 2.2, an expression for the maximum excursion of a particle was found,

$$r_\mathrm{max} - r_0 \approx \frac{1}{\epsilon_0}\frac{m}{e}\frac{I}{v_\mathrm{b}}\frac{1}{\pi R_\mathrm{b}^2}\frac{1}{B^2}r_0 = \frac{I}{2I_\mathrm{brillouin}}r_0. \tag{5.3}$$

For the given parameters, particles only deviate by 0.24 % from their initial offset, e.g. for the particles at the edge of the beam $r = 49\,\mu\mathrm{m}$.

For the McMillan distribution, the rotation velocity depends on the radius due to the radial dependence of the electric field,

$$\omega_{\mathrm{E\times B}} = \frac{1}{2\pi\epsilon_0}\frac{I}{v_\mathrm{b}}\frac{1}{B}\left(1+\frac{a^2}{R_\mathrm{b}^2}\right)\frac{1}{r^2+a^2}.$$

The revolution frequencies differ by an order of magnitude depending on the radius: for I=1.7 A, a=3.6 mm and $R_\mathrm{b} = 22\,\mathrm{mm}$, particles in the core oscillate with 92 MHz, those at the beam edge with 2.4 MHz.

Near the axis, the electric field of a McMillan distributed beam is linear in the radius r. Compared to a homogeneously distributed beam of radius R_b however, the field is higher by a factor $1 + R_\mathrm{b}^2/a^2$ (≈ 38.3 for the considered parameters). Since the field in the core is linear, it can be expected that the motion of the particles is similar, at least initially. The excursion predicted in this case by (5.3) for a particle at $r_0 = 1\,\mathrm{mm}$ is 200 µm or 20 % of the initial offset. At these large deviations, the electric field and thus the distribution is likely to change during transport.

Current limits

To be able to estimate when deformations in the distribution are likely to appear, it is important to know whether a given beam current can be considered “high” or “low”. Thus, the question how much beam current in total can be transported becomes interesting.

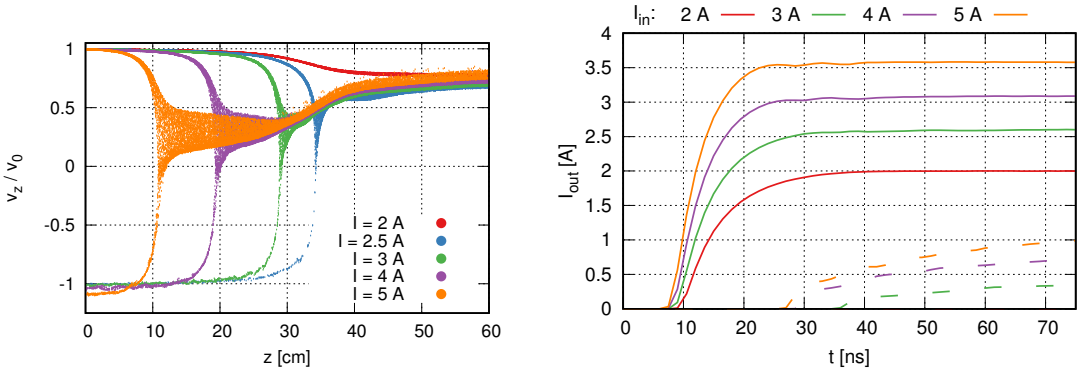

(a) Longitudinal velocity over particle position.

(b) Transmitted current. Dashed curves are the reflected current.

Figure 5.7.: Results from the simulation of a model system, compressing a 15 mm, 5 keV electron beam to 3 mm ($c = 0.2$).

One current limit is given by the Brillouin flow limit (2.6). Below $I_{\text{brillouin}}$, the magnetic force is able to counteract the force from the electric self-field. For the given case, at the cathode,

$$I < I_{\text{brillouin}} = \frac{1}{2}\frac{e}{m}\pi\epsilon_0 v_\text{b} R_\text{b}^2 B^2 \approx 410\,\text{A}.$$

Due to its high value, the Brillouin current limit is not very binding. It becomes even less relevant at higher magnetic fields, since the beam radius only scales with $\sqrt{B_1/B_2}$ and therefore $I_{\text{brillouin}} \propto B_2/B_1$.

The beam potential for the required parameters is easily in the same order of magnitude as the accelerating voltage in the cathode (Homogeneous beam, $I = 2\,\text{A}$, $R_\text{b} = 2\,\text{cm}$ and $W = 5\,\text{keV}$: beam potential -940 V). If, during compression, the potential increases by a value higher than the accelerating voltage of the beam, particles will get reflected under their own space charge influence. This limit is an equivalent of Child-Langmuir's law.

The expression for the potential of an arbitrarily distributed beam with some radius R_b always contains terms that scale with $v_\text{b}^{-1}\ln(R_\text{b}/R_\text{p})$, where v_b is the particle velocity, R_b the beam size and R_p the size of the beam pipe. Since the logarithmic term only increases slowly, one would suspect that the limit can not be easily reached. Yet, as the potential decreases, the electrons become slower and the density increase leads to an even lower potential, which exacerbates the effect.

Figure 5.7 shows results from the simulation of a model system for a range of injected beam currents from 2 A to 5 A. In this example, a 5 keV electron beam is compressed from 15 mm to 3 mm radius by an increase of magnetic field from 100 mT to 2.5 T generated by two solenoids. At 2 A, all particles are transmitted but the beam is slowed down by about 2 keV. At higher currents, electrons return to the gun at increasingly earlier positions. The limit is not a hard one: increasing the current still results in some increase in the output, but not to the same degree, as can be seen in Figure 5.7b.

For currents close to the limit, it takes a long time for particles to be reflected. At

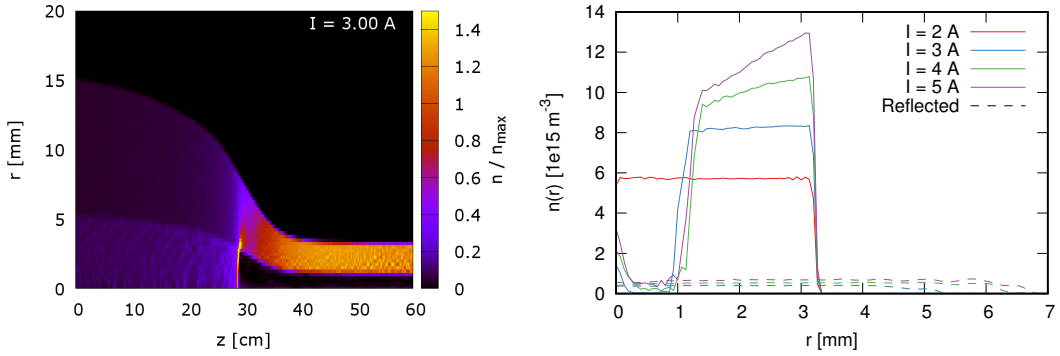

(a) Beam density.

(b) Transmitted current.

Figure 5.8.: Density profiles over the current limit for the compression of a 5 keV homogeneous electron beam from 15 mm to 3 mm.

2.2 A current, the transport is already stable after 60 µs. For 2.4 A, particles start to move backwards at about 72.5 µs. At 2.3 A however, the effect only occurred after 150 µs of simulation.

If particles would have been able to gain sufficient magnetic moment, the magnetic mirror effect could also have been responsible. However, in the simulation, the reflected particles completely convert their kinetic energy into potential energy before reversing their direction of travel. Furthermore, the potential rise compared to the potential at the cathode peaks above the beam energy at the inflection point.

Figure 5.8 shows the beam density along with the current profile of the transmitted and the reflected current. The core of the beam is almost completely reflected at a thin region of high charge density, while particles at larger radius are able to pass. This forms a hollow beam. At higher currents the current profile additionally becomes more and more inhomogeneous.

An upper current limit can be found by assuming that the beam does not slow down under its own space charge, i.e. that the initial velocity v_1 is equal to the final velocity v_2. This assumption is questionable, since Figure 5.8a shows a significant deceleration of the beam. In that case, energy conservation for the central particle at the reflection point is

$$\frac{1}{2}mv_1^2 - \frac{e}{2\pi\epsilon_0}\frac{I_{\text{limit}}}{v_1}g(R_\text{b}, R_{\text{p},1}) = -\frac{e}{2\pi\epsilon_0}\frac{I_{\text{limit}}}{v_1}g(cR_\text{b}, R_{\text{p},2})\,,$$

where $R_{\text{p},1}$ and $R_{\text{p},2}$ are the radii of the beam pipe at the two points of investigation. Then,

$$I_{\text{limit}} = \pi\epsilon_0\sqrt{8\frac{e}{m}}\left(g(R_\text{b}, R_{\text{p},1}) - g(cR_\text{b}, R_{\text{p},2})\right)^{-1}U^{3/2}. \tag{5.4}$$

U is the acceleration voltage of the beam and g a distribution-dependent function containing the terms in the potential not dependent on the radius r. Those are given in Table 5.2.

Homogeneous distribution	$g(R_\mathrm{b}, R_\mathrm{p}) = \ln\left(\frac{R_\mathrm{b}}{R_\mathrm{p}}\right) - \frac{1}{2}$
McMillan distribution	$g(R_\mathrm{b}, R_\mathrm{p}) = \ln\left(\frac{R_\mathrm{b}}{R_\mathrm{p}}\right) - \frac{1}{2}\left(1 + \frac{a^2}{R_\mathrm{b}^2}\right)\ln\left(1 + \frac{R_\mathrm{b}^2}{a^2}\right)$
Gaussian distribution	$g(R_\mathrm{b}, R_\mathrm{p}) = \ln\left(\frac{R_\mathrm{b}}{R_\mathrm{p}}\right) + \frac{1}{2}\gamma - \ln\left(\frac{\sqrt{2}\sigma}{R_\mathrm{b}}\right)$

Table 5.2.: Geometric functions for homogeneous, McMillan and Gaussian beam distribution. $\gamma \approx 0.577$ is the Euler-Mascheroni constant.

Assuming that the beam distribution remains fixed transversely during transport, a lower current limit can be found from energy conservation for the central particle. Looking for roots in

$$\begin{aligned} 0 = H_2 - H_1 &= \frac{1}{2}mv_2^2 - E_1 + e\left(\varphi(R_\mathrm{b}) - \varphi(cR_\mathrm{b})\right) \\ \longrightarrow v_2^3 &+ \left[\frac{eI}{m\pi\epsilon_0}g(R_\mathrm{b}, R_{\mathrm{p},1})\frac{1}{v_1} - \frac{2E_1}{m}\right]v_2 - \frac{eI}{m\pi\epsilon_0}g(cR_\mathrm{b}, R_{\mathrm{p},2}) = 0, \end{aligned}$$

results in the condition that

$$4\left(\frac{2E_1}{m} - \frac{eI}{\pi\epsilon_0}\frac{1}{\sqrt{2mE_1}}g(R_\mathrm{b}, R_{\mathrm{p},1})\right)^3 - 27\left(\frac{eI}{m\pi\epsilon_0}g(cR_\mathrm{b}, R_{\mathrm{p},2})\right)^2 > 0. \tag{5.5}$$

The derivation assumes that all particles possess the same longitudinal velocity, which due to the radial dependence of the potential is not correct. However, for realistic values of the beam radius and beam pipe sizes, the velocity spread inside the beam is relatively small. Equation (5.5) can be solved approximately by ignoring the I^3-term,

$$I < 4\pi\epsilon_0\frac{1}{e}\sqrt{\frac{2}{m}}E_1^{3/2}\left(\frac{g_1 - \sqrt{3g_2^2 - g_1^2/3}}{4g_1^2 - 9g_2^2}\right) = 4\pi\epsilon_0\sqrt{\frac{2e}{m}}U^{3/2}\left(\frac{g_1 - \sqrt{3g_2^2 - g_1^2/3}}{4g_1^2 - 9g_2^2}\right), \tag{5.6}$$

where $g_1 = g(R_\mathrm{b}, R_{\mathrm{p},1})$ and $g_2 = g(cR_\mathrm{b}, R_{\mathrm{p},2})$.

Figure 5.9 shows the current limits calculated from both estimations for a homogeneous distribution as well as for a McMillan distributed beam in comparison to the PIC simulations of the previously described model system. In general, the estimation predicts the current limit found in the *bender* simulations. These were obtained by simulation of various beam currents. The error bars indicate both the highest current, where no particles are reflected, as well as the current of the simulation where reflection was observed first. Furthermore, the energy scaling with $U^{3/2}$ could be reproduced in simulations with $c = 0.2$ for $E = 2.5\,\mathrm{keV}$, $E = 5\,\mathrm{keV}$, $E = 7.5\,\mathrm{keV}$ and $E = 10\,\mathrm{keV}$.

Equation (5.6) is a good approximation for lower values of c. It only starts to deviate from the full solution at weak compression, where the current limit is relatively high.

Both expressions predict no current limit when $R_{\mathrm{p},2} < cR_{\mathrm{p},1}$. In that case, the potential on the axis will be larger than at the source and the electrons will gain energy. The same

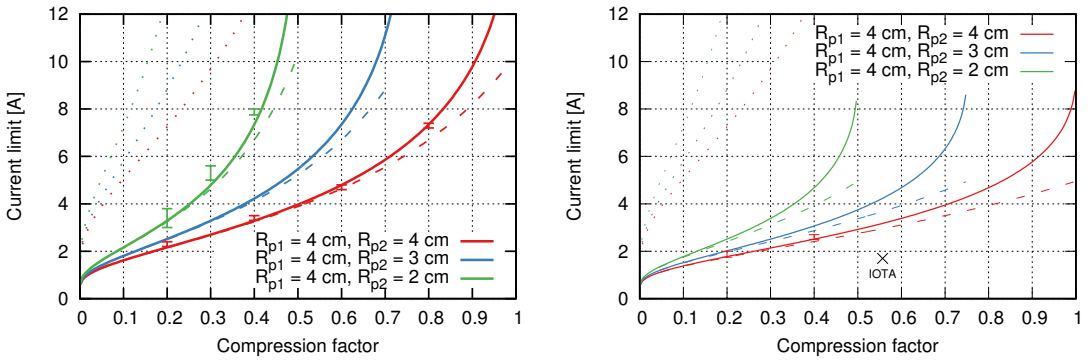

(a) Homogeneous distribution ($R_\mathrm{b} = 15\,\mathrm{mm}$). (b) McMillan distribution ($a = 3.6\,\mathrm{mm}$).

Figure 5.9.: Current limits for a homogeneous distribution and the McMillan distribution at $E = 5\,\mathrm{keV}$. Solid lines are the current limits calculated numerically from (5.5), dashed lines are a result of the approximation using equation (5.6), dotted curves from (5.4). The discrete points are current limits found by simulating a model system using *bender*. The upper and lower limits of the error bars indicate the currents at which reflection of particles was observed or not observed respectively.

result can be found from simulation of the model system. For example, for $c = 0.6$ and a beam pipe ratio of 0.5 , simulations up to 20 A beam current could be made—however, with some aberration in the beam distribution. To avoid the current limit as well as any additional effects due to changes in particle velocities, it would be ideal to follow the envelope of the electron beam with the beam pipe.

For a McMillan distributed beam, for the parameters used, the current limit predicted by the estimation is between 5 % and 50 % lower than the value for the homogeneous beam. A comparison with *bender* simulations proved difficult due to aberration in the profile as well as a curious self-modulation of the beam. Only for $c = 0.2$ and $c = 0.4$ the results of (5.6) could be confirmed.

For the parameters of the IOTA electron lens, $c = 0.55$, $R_{\mathrm{p1}} = 4\,\mathrm{cm}$ and $R_{\mathrm{p2}} = 2.5\,\mathrm{cm}$, equation (5.6) predicts a current limit of 7.9 A (9.2 A from the numerical solution) for a homogeneously distributed beam with $R_\mathrm{b} = 2\,\mathrm{cm}$. This is matched by the full *bender* simulation. While there is no reflected charge for 7.5 A, at 10 A current, a charge build-up in the transfer solenoid occurs. For the McMillan distributed beam with $a = 3.6\,\mathrm{mm}$, the current limit is predicted to be 4.3 A (numerical: 5.5 A).

Profiles

Figure 5.10 shows the current profiles extracted from the simulation of the full electron lens. The distribution of the homogeneous beam remains constant. There is a small dependence of the final beam radius on the current. Since this deviation is lower in size than the grid spacing used for calculation of the electric field, it is difficult to draw a

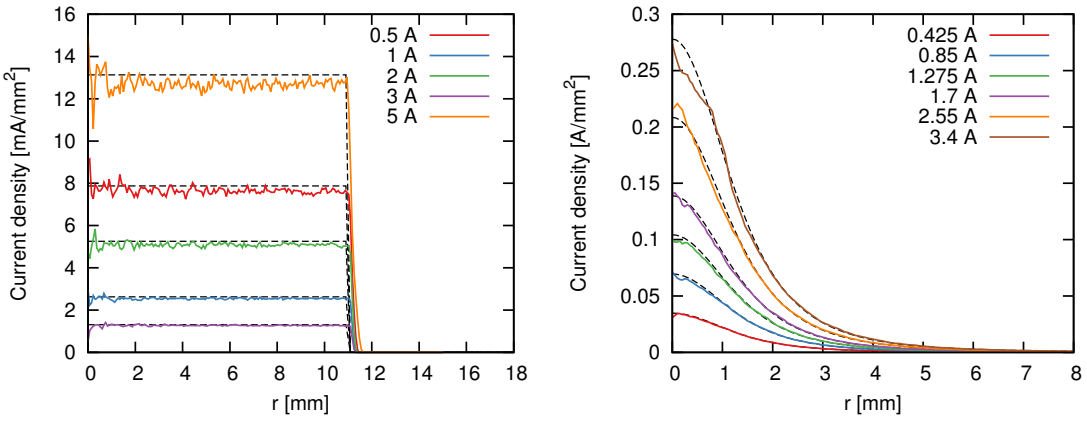

(a) Homogeneous distribution ($R_\mathrm{b} = 15\,\mathrm{mm}$). (b) McMillan distribution ($a = 3.6\,\mathrm{mm}$).

Figure 5.10.: Current profiles from the simulation of the IOTA lens. The offset due to the drifts were subtracted before calculation of the profile.

conclusion from this observation.

For higher currents, the profile in the simulation of the McMillan distributed beam shows a clear deviation from the expected current profile. The origin of these becomes more apparent in the transverse profiles shown in Figure 5.11. They show some filamentation in the form of "spiral arms" of higher density.

Since the *bender* calculations did not have enough resolution to accurately resolve the filamentation, a small 2d particle-in-cell code using similar algorithms as those described in Section 3.2.1 and Section 3.2.2 was implemented. It calculates the time evolution of a beam with a given profile in a purely longitudinal magnetic field and includes the beam pipe as boundary in the potential calculation. Beyond the envelope oscillations described earlier, just as in the full 3d case, the homogeneous distribution was found to be stable over very long times. Even after 25 m, a 5 keV, 5 A electron beam with 22 mm beam radius in a 100 mT magnetic field did not show any aberration.

For the McMillan distribution, results are shown in Figure 5.12. Here, the aberrations do not form spirals but show up as rings. Their number increases over time as they become more peaked and thinner. The initial behaviour does not depend on the grid resolution. The rings form at the same positions. However, the simulations start to deviate when these are not sufficiently resolved by the grid. Therefore, it is very likely that the 3d simulation did not have enough resolution to correctly calculate the evolution of the distribution. Another possible reason for the different observed structures could either be longitudinal space charge forces or the bending.

One possible source for the formation of the rings might be the different strength of radial oscillation. For example at 3 A and 0.1 T, the rms size of the whole beam initially oscillates by 1 %, which decreases to below 0.2 % after 30 cm. Meanwhile, over the first meter of transport, the density at the origin continues to oscillate by 20 % with a frequency

[3] Calculated as $\sum_{\mathbf{r}_i < R_\mathrm{b}} \left(E_r^\mathrm{sim}(\mathbf{r}_i)\,/E_r(\mathbf{r}_i) - 1\right)$.

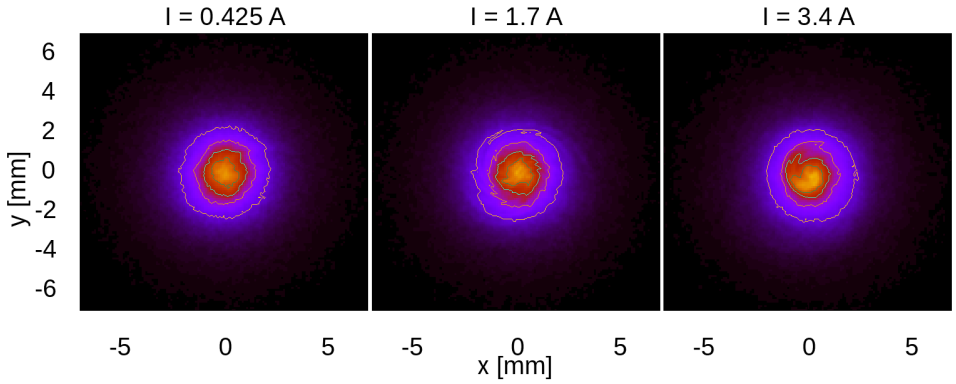

Figure 5.11.: Transverse current profile for McMillan distributed beams at various currents from the *bender* simulation of the IOTA electron lens.

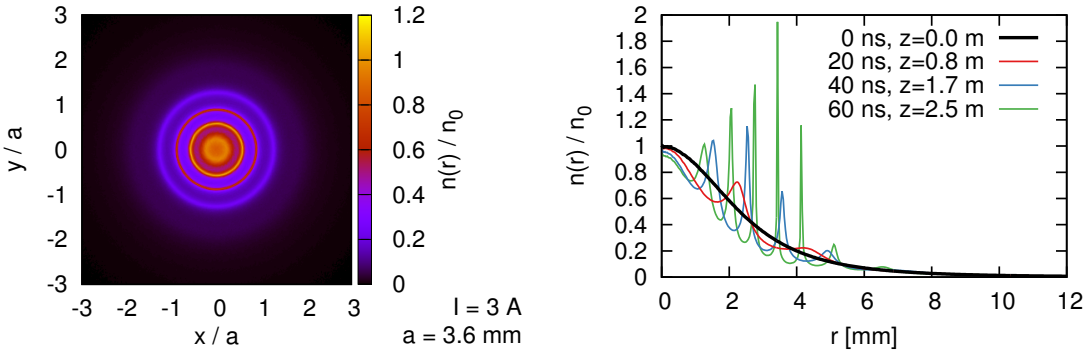

(a) Transverse current profile after 1.5 m. (b) Radial current profile at various positions.

Figure 5.12.: Two-dimensional simulation of the electron beam transport with 66 µm grid resolution and 1×10^8 macroparticles: Evolution of a McMillan distribution ($a = 3.6\,\mathrm{mm}$, $R_\mathrm{b} = 2.5\,\mathrm{cm}$, $I = 3\,\mathrm{A}$, $B = 0.1\,\mathrm{T}$) with the beam pipe at 5 cm.

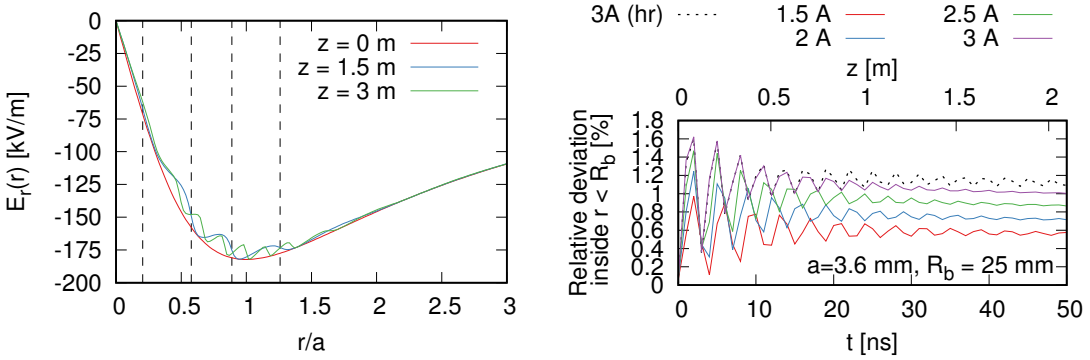

(a) Electric field. (b) Deviation from the initial electric field[3].

Figure 5.13.: Electric field from the simulation of the transport of a McMillan distributed beam. Simulation parameters for (a) and the dashed curve in (b) are the same as in Figure 5.12, 250 µm grid resolution and 4×10^6 macroparticles otherwise.

close to the cyclotron frequency. For the homogeneous distribution, the amount of energy converted between kinetic and potential energy in each radial oscillation stayed constant over 25 m of simulated transport. This was not the case in the simulation of the McMillan distribution. There, the amount of energy exchanged drops below 8 % in the first 50 cm.

The electric field produced by the current distribution in Figure 5.12a is displayed in Figure 5.13a. The rings lead to areas, where the electric field is lower than initially. The error in the electric field is largest during the initial expansion and then oscillates around the final value with decreasing amplitude. Even though more and more rings form and thus the error in the density increases permanently, the error in the electric field approaches a constant value. The development of the deviation over time is shown in Figure 5.13b. Due to a limitation of the exported data, these curves do not contain enough points to resolve the radial oscillation. This however allows a visual comparison of the two displayed simulations at different grid resolution. These show an identical behaviour until the time at which the coarser simulation lattice is not able to resolve the peaks.

From the *bender* simulations, kick maps were calculated. These can be used as input for a calculation of the ring dynamics to study the influence of the imperfections on the circulating beam. The procedure and exemplary data can be found in [74, 80].

5.2. Simulations of beam transport for the FRANZ facility

At the Frankfurt neutron source facility, a driver linac capable of transporting up to 140 mA will provide a 2 MeV proton beam for experiments. Beyond measurements of neutron capture cross sections of interest for the understanding of nucleosynthesis, the facility is a test bench for novel accelerator components. An overview over the project can be found in [5].

A schematic of the facility under construction is displayed in Figure 5.14. The beam will be provided by a filament-driven ion source at an energy of up to 120 keV. The low-energy beam transport section is divided in two sections consisting of two solenoid magnets each. The first matches the beam through a chopper system. The chopper system used for FRANZ utilizes a new concept that combines the benefits of magnetic and electric deflection. It can be used to chop the proton beam into 50 ns long pulses at a repetition rate of up to 250 kHz. *bender* was used to investigate the pulse shaping including space charge forces and the complicated field geometry of the system. In Section 5.2.2, a short overview over the performed simulations is given. The design of the system and detailed analysis of the simulation results can be found in [11].

After the chopper system, the third and fourth solenoid provide the focusing required for injection of the beam into an RFQ (radio frequency quadrupole). *tralitrala* can be used for the simulation and an example from those performed in [81] is presented in the next section.

The RFQ, operated at 175 MHz, will then accelerate the protons to an energy of 700 keV. It is coupled to an IH-type (interdigital H-mode) cavity, which provides acceleration to the final beam energy of 2.03 MeV. Downstream, a CH-type structure (crossbar H-mode)

is used to longitudinally focus the beam and to vary its energy by ±200 keV.

Depending on the experiment, the beam will then either be transported directly to a target or additionally compressed by a bunch compressor. The design shown in Figure 5.14 consists of a kicker system, that deflects nine successive bunches from the rf accelerator onto paths of different lengths created by four dipole magnets. In simulations, the system was able to produce 1 ns long pulses [82] at a neutron production target.

5.2.1. Low-energy beam transport

In [81], the beam transport through the FRANZ Low-Energy Beam Transport section was studied for various geometries using, among others, *tralitrala*. The graphics card version of the latter made it possible to perform calculations of a wide range of settings for the two solenoids of each section. An example is shown in Figure 5.15. These maps contain results from 82368 simulations runs, calculated in 2.5 days[4].

These use the same simulated beam distribution for all three ion species extracted from the ion source. Its emittance is $\epsilon^{x}_{\mathrm{rms,norm}} = 0.029\,\mathrm{mm\,mrad}$. At a proton current of 50 mA, 5 mA H_2^+ and 5 mA H_3^+ are assumed to be present. Until the start of the chopper, a space charge compensation of 95 % is assumed—calculated by scaling of the electric field. Within the chopper system itself, compensation will be low due to the presence of external electric fields. This is also the case for the pulse in the second half of the LEBT since the pulse length is much shorter than the compensation built-up time τ_{scc}.

The transmission of the proton beam in Figure 5.15a shows two areas of high transmission in the parameter space. The area towards lower solenoid strengths corresponds to a situation, where the beam is approximately parallel to the beam axis between the first two magnets and is then focused to fit between the chopper plates by the second. When the magnetic field in the first solenoid B_1 is increased from this setting, the beam focus shifts towards the position of the second solenoid. The band of low transmission around $B_1 \approx 400\,\mathrm{mT}$ is caused by the focus of the beam being located within the second solenoid, which is then unable to provide any focusing. Towards even higher values of B_1, the

[4] On a Nvidia Geforce GTX 770.

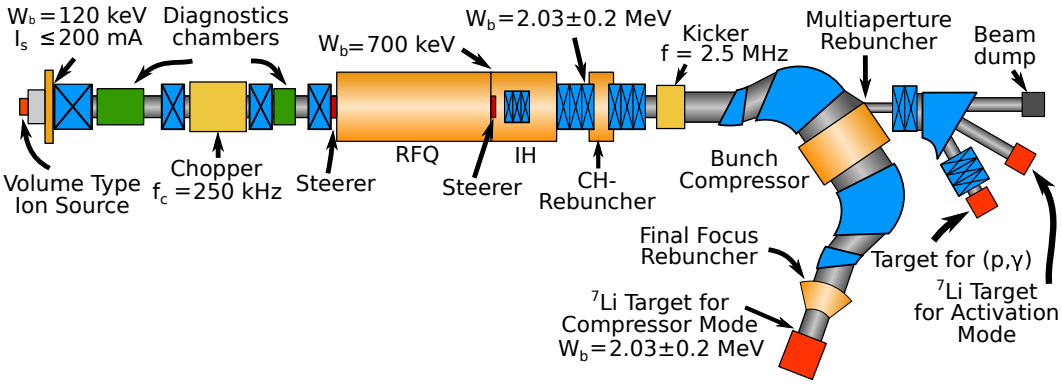

Figure 5.14.: Schematic of the future Frankfurt neutron source FRANZ.

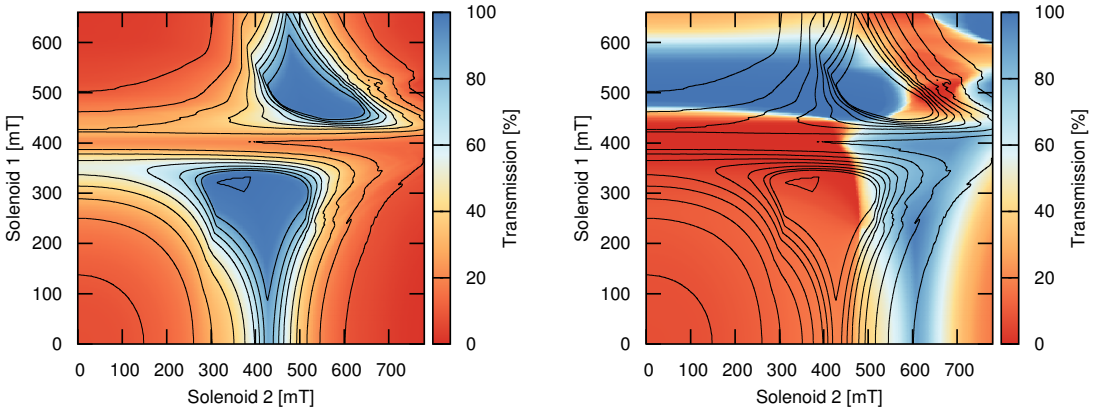

(a) 50 mA proton fraction. (b) 5 mA H_2^+ fraction.

Figure 5.15.: Transmission of two of the three beam species in simulations of the first section of the FRANZ LEBT. Contour lines at 10 % transmission steps.

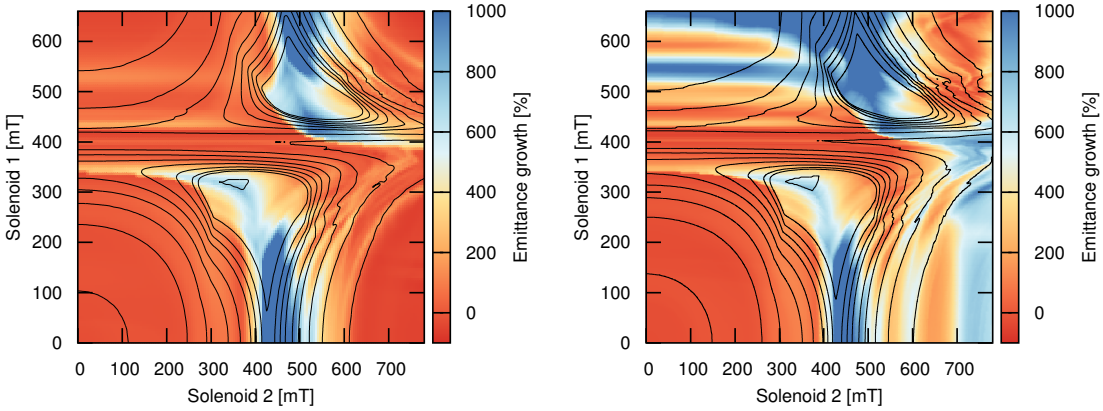

(a) Only proton beam. (b) Including H_2^+ and H_3^+.

Figure 5.16.: Emittance growth in the first section of the FRANZ LEBT. The contour lines in (b) were taken from Figure 5.15, those in (a) from a similar calculation without the additional species.

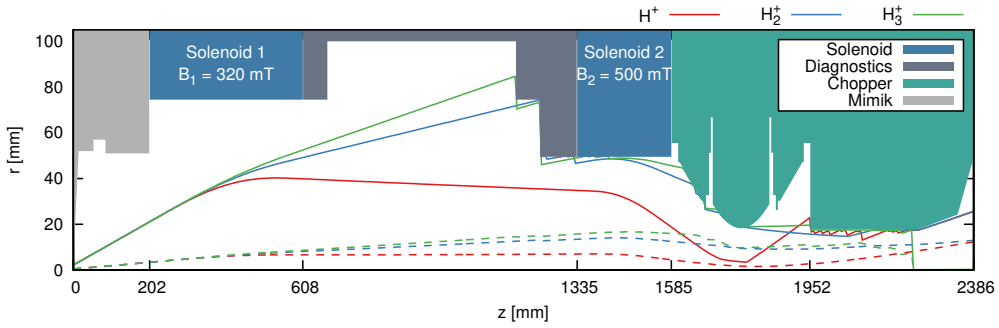

Figure 5.17.: Beam envelope for the optimal case identified in [81]. Solid lines are the particles at the beam edge, dashed lines are the rms envelopes.

beam radius increases again at the position of the second solenoid and, also assuming a higher field strength B_2, the transmission increases again, which leads to the second high transmission area in Figure 5.15a. This setting corresponds to the "crossover" matching of the proton beam in Section 4.3.

When only one of the two magnets is operating, the beam transmission is relatively low except when the focus is placed between the chopper plates, which is the case around $B_1 \approx 350\,\mathrm{mT}$, B_2 small and $B_2 \approx 430\,\mathrm{mT}$, B_1 small.

The emittance of the proton beam, shown in Figure 5.16b, varies over a wide range of values. Due to particle losses, the emittance also decreases in some areas. Particle losses of the outlying particles are also responsible for the variation of the emittance growth over several 100 % in the areas of high transmission. In [81], the "crossover" matching at higher solenoid strengths and the regular matching were found to lead to similar values of emittance growth at low beam currents. This is no longer the case at 50 mA for the given realistic beam distribution. There, the strong electric field in the crossover point leads to a redistribution and to emittance growth.

Figure 5.16b shows two bands of very high emittance growth, around $B_2 \approx 450\,\mathrm{mT}$ for low field strengths in the first solenoid and around $B_2 \approx 500\,\mathrm{mT}$ for large values of B_1. These are also present in effectively zero current simulations [81, Abbildung 3.3, p. 25], albeit only amounting to an emittance growth of 100 %. At these settings, the proton beam enters the second solenoid with a large size and is then focused strongly to fit through the chopper section. Since the focusing strength of a solenoid increases radially towards its aperture, the distribution in $x - x'$ becomes S-shaped. These changes in turn lead to strong non-linear field in the uncompensated chopper section, resulting in an emittance growth above 2500 %.

While the proton beam transmission is not significantly changed by the presence of the additional beam fractions, the H_2^+ and H_3^+ ions significantly contribute to the emittance growth at settings where these are not filtered in front of the uncompensated chopper section. For example, this is the case in the area of high transmission with a focus between the first and second solenoid. An interesting effect can be identified by comparing the two plots in Figure 5.16 for settings at which only the first solenoid is operating. Towards high B_1, the emittance growth alternates between high and low values. The maxima in the emittance growth are located at solenoid strengths, where the focus point of the H_2^+ and later the H_3^+ ions are located within the chopper section. The electric field produced by these ions affects the remaining protons, leading to the formation of a hollow beam.

Figure 5.17 shows the beam envelope for the optimal setting identified in [81] as a trade-off between a large transmission—97.1 % in this case—and a low emittance, which is $\epsilon^x_{\mathrm{rms,norm}} = 0.061\,\mathrm{mm\,mrad}$, a 209 % increase.

5.2.2. Beam shaping simulations

Figure 5.18a depicts the technical design of the E × B chopper system located between the second and third solenoid of the FRANZ LEBT. The system consists of two parts—a deflection section and a separation system. In the first section, a dipole magnet deflects the beam by approximately 10°. In the second stage, the deflected beam is separated from

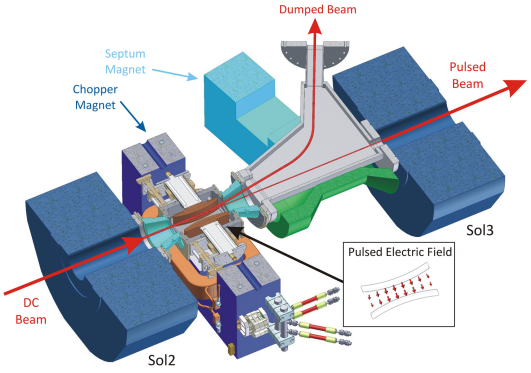

(a) Cross-sectional view of the E×B chopper [11, Fig. 4.2] located between two solenoids of the FRANZ LEBT.

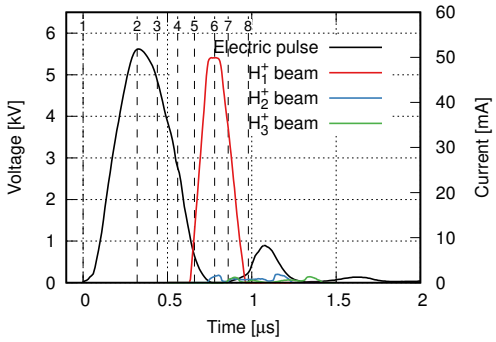

(b) Pulse shape applied to the chopper plates and the transmitted beam at the RFQ entrance. Dashed lines mark images in Figure 5.19.

Figure 5.18.: E×B chopper.

the axis of the transmitted beam and dumped. To produce a beam pulse, the magnetic deflection in the first section is compensated by an electric field applied to the deflector plates. The length of the pulse is then defined by the length of the voltage pulse and the size of an aperture located in front of the third solenoid. This configuration has the benefit, that the high voltage needs to be applied only for a short period of time, minimizing the probability of electric breakdowns. Furthermore, the beam can be safely dumped outside of the beam line.

In [11, p. 53-63], the system was optimized to minimize the impact of the complicated field geometry on the beam. *bender* was used to investigate the beam transport for several variations of the geometry. Without space charge, the rms emittance was found to remain approximately constant at the input value of $\epsilon_{\mathrm{rms,norm}} = 0.053\,\mathrm{mm\,mrad}$.

Two important questions are whether the beam quality also remains unchanged during transport through the time-dependent fields in the chopper system for a space charge dominated beam, and if the system is able to filter the unwanted H_2^+ and H_3^+ fractions present in the beam before injection into the RFQ.

To answer these questions, simulations using *bender* were performed. The magnetic field of the chopper dipole magnet and the solenoid magnets as well as the electric field produced by the deflection plates were calculated using CST EM Studio [83] and included in the simulation. The strength of the latter is varied over time. The voltage pulse, which was taken from a measurement of the pulse generator, is shown in Figure 5.18b.

Due to their vicinity, solenoids 2 & 3 and the chopper dipole magnet influence each other. For example, some flux is drawn from the solenoids into the yoke of the dipole magnet. To be able to change the strength of each magnet independently without having to calculate the full fields, three fieldmaps for this combination of magnets were generated. In each of these fieldmaps, only one magnet is activated. In *bender*, these fieldmaps are then overlapped and added. Since all three magnets are operated far away from saturation of the magnetic materials, this superposition should be valid.

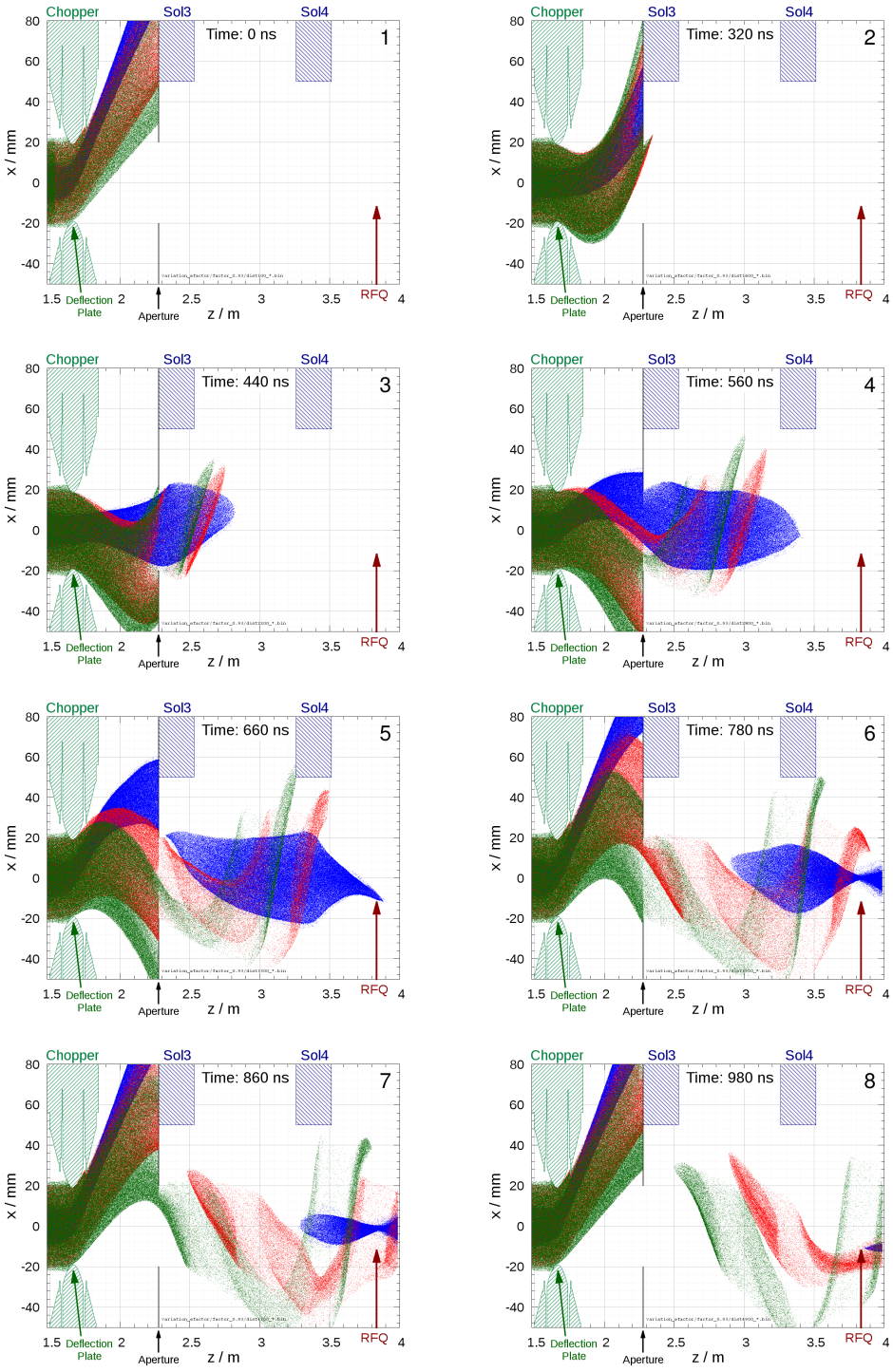

Figure 5.19.: Beam distributions of the protons (blue), H_2^+ ions (red) and H_3^+ ions (green) in a simulation of the pulse shaping at different times during the voltage pulse. Taken from [11, p. 86].

An input distribution was taken from simulations similar to those presented in the previous section. A current of 50 mA was used. 1000 proton macroparticles and 100 macroparticles carrying a current of 5 mA for both H_2^+ and H_3^+ are inserted in every step. To remove any switch-on effects from the forming beam, each simulation was started including the distribution of an already-formed beam taken from a previous simulation. Such a distribution is shown for $t = 0$ ns in Figure 5.19.

The finite difference solver (Section 3.2.2) was used at a grid resolution of 2.5 mm in each direction. The full geometry of the vacuum vessels and the chopper plates was included. This reduces the total number of freedom that have to be solved for by the Poisson solver from 6.7 million to 2.1 million and includes effects from image charges on the wall. Longitudinally, Neumann boundary conditions are used. On 10 processors on the FUCHS cluster [62], each run takes typically about 9 h.

Figure 5.19 shows the particle distributions during several stages of the simulation. At 0 ns, it corresponds to the distribution without electric deflection. All three particle species possess the same beam energy, $W = 120$ keV. They have the same electric rigidity $(E\rho) = 2W/q$ and are deflected equally by the electric field, but differ in magnetic rigidity $(B\rho) = p/q$ due to the difference in mass. Therefore, the H_2^+ and H_3^+ ions are deflected less at $t = 0$ ns in Figure 5.19.

Then, the voltage pulse is applied. The first ions transmitted through the aperture are H_2^+ and H_3^+ ions at about 320 ns. Since the electric deflection force was matched to compensate the (larger) magnetic deflection for protons, the heavier ions are overdeflected, producing two separate pulses while sweeping over the aperture. Due to the larger velocity of the protons, these heavier and slower species are overtaken and arrive at the RFQ behind the proton pulse.

Between 320 ns and 660 ns, the proton beam pulse forms. Notice, that due to the time of flight difference between the chopper plates and the aperture (≈ 143 ns for 120 keV protons), at this time, the voltage at the chopper plates is already decreasing.

The pulse has a rise time of 120 ns, followed by a 50 ns plateau with less than ± 1.6 mrad deviation from the axis and a 160 ns tail. The asymmetry between head and tail is already present in the voltage pulse. The final current pulses for the matched case in front of the RFQ are also shown in Figure 5.18b.

Both the head and the tail of the pulse have significant offsets and angles. In between the pictures at 440 ns and 560 ns in Figure 5.19, these seem to disappear for the head of the pulse only to be present again at 660 ns. Furthermore, the offset is shifted from positive x (and positive deflection angle) towards negative x. This is a result of the rotation induced by the fringe fields of the solenoid magnets [84, p. 144]. At 560 ns, most of the offset of the head of the proton pulse is found in vertical direction.

The unwanted ion species are insufficiently focused and have either high position offsets or angles, up to 3 cm and ± 80 mrad respectively for H_2^+ and 4 cm and ± 50 mrad for H_3^+. Most of these ions will therefore not be injected into the RFQ, which has an aperture of only ± 3 mm [11, p.88].

Parameter studies for different pulse shapes, different apertures after the chopper and various types of mismatch were performed. It was found, that the E × B chopper system is able to provide the beam parameters required by the FRANZ project.

6. Summary and Conclusion

Compensation of space charge forces by particles of opposite charge is an important effect for the transport of high-intensity, low-energy ion beams, potentially reducing the required focusing forces and the rate of emittance growth due to a redistribution of the beam. In this thesis, space charge compensation of a proton beam by electrons in a drift section was investigated. In the approach taken, the secondary particles—both electrons and residual gas ions—were included self-consistently in a simulation.

For this purpose, a new electrostatic particle-in-cell code (PIC code) named *bender* was developed. In Chapter 3, PIC was introduced as a solution method for the Vlasov-Poisson system by the use of simulation particles. *bender* uses the Velocity Verlet algorithm for the integration of motion. The implementation was tested on several test systems and its correctness as well as its long-term conservation of energy demonstrated. For calculation of space charge forces in three dimensions, two solvers were implemented: a solver utilizing Fourier transforms on Cartesian, cubic lattices using the FFTW library [32] and one solving a finite difference approximation of Poisson's equation using the PetSc library [29]. The latter supports Dirichlet boundary conditions on arbitrary geometric objects and can be used for systems with complex geometries. A two-dimensional rz solver was implemented using finite differences as well. All three solvers support parallel computation of the fields in some way, either by distributing the grid longitudinally or by distributing the grid in arbitrarily located grid boxes. These were then tested against the analytically calculated field of either a Gaussian distributed beam or sphere.

After these components were found to be working correctly when used separately, the code was tested against two known self-consistent solutions of Vlasov's equation. As an example of a system including a beam, a KV distributed beam was matched through a quadrupole channel and several cells were simulated using *bender*. For large numbers of particles and high grid resolution, the simulated phase advance converges to the correct value. As a test from non-neutral plasma physics, a particle distribution of thermally distributed electrons confined in an external potential was generated and loaded into a simulation. For this purpose, an algorithm to solve the Poisson-Boltzmann equation was implemented. For high numbers of macroparticles, the resulting distribution remained stable. However, in all simulations, an energy growth dependent on the number of macroparticles and to a lesser degree on the grid resolution was found. This effect was identified as the stochastic heating known to be present in PIC simulations [21, p. 316].

In addition to *bender*, a simpler PIC code named *tralitrala* was written for fast simulation of Low-Energy Beam Transport systems. It includes various typical beam optical elements such as drifts and solenoids either by field integration or by using transport matrices and runs both on CPUs and graphic processors. Speed-ups of up to factor 100 compared to the CPU version were demonstrated when using the latter.

Particle collisions with the residual gas were included into *bender* using the Null-collision method. The code includes model cross sections for both proton impact and electron impact ionization. Both calculate differential cross sections and therefore reproduce the correct energy distribution of the secondary electrons. The undetermined quantities are calculated from a classical collision model to guarantee energy and momentum conservation.

Using *bender*, compensation in a model system of a converging, homogeneous 120 keV, 100 mA proton beam was simulated. The build-up of the compensation in the simulation fits the expected behavior: initially the charge in the system increases linearly with the ionization rate until losses occur and an equilibrium forms. The compensation in the presented simulation reached values around 80 %, varying longitudinally by several percent. In the calculated charge densities, various features not explained by a homogeneous reduction of the electric field were identified. These are the formation of a hollow beam around the beam focus, an accumulation of residual gas ions in the center of the system as well as an area of negative charge density at the edge of the beam. Furthermore, Gaussian velocity distributions are present at all locations in the simulation.

From the assumption of Boltzmann distributed electrons, the spatial distribution of electrons in an external potential was calculated. To understand the influence on beam transport, the Poisson solver in *tralitrala* was replaced by a one-dimensional radial solver for the Poisson-Boltzmann equation. At low temperatures, the electron charge density is equal to the beam's charge density until some radius and then decreases. This leads to a non-linear electric field, especially at the beam edge. The emittance growth due to these fields was studied in various systems. The *tralitrala* simulation of the model system including a thermal electron distribution qualitatively reproduces all previously mentioned features of the steady-state charge distributions. The formation of the hollow beam was found to be a result of the non-linear radial electric field due to the inhomogeneous compensation. The accumulation of residual gas ions is a result of a local overcompensation due to the density maximum at the beam edge in the focus.

The origin of the Gaussian velocity distributions was studied. The electron temperatures as well as the compensation degree were found to vary strongly with the particle per macroparticle ratio i.e. the number of macroparticles used to represent the system. A potential explanation of the numerical influence could be the stochastic heating observed during the code tests. The hypothesis was formed that the additional energy introduced by the numerical heating is compensated by the system by increased particle losses, leading to a compensation well below 100 %. This needs to be further investigated, for example by identifying the influencing parameters for the statistical heating in the test simulation for comparison with the compensation system. Since the observed rates can be larger in magnitude than physical heating processes, before these can be implemented, the understanding of the numerical effects needs to be improved. Optionally, a different approach to solving the Poisson-Vlasov system, such as direct methods, could be pursued.

The presented simulations provide a starting point for future investigations of the dynamics of charged many-particle systems. The simulated equilibrium was observed to be determined by particle production as well as loss mechanisms, which are themselves influenced by heating (and possibly present cooling) processes. Another system governed

by similar laws are Gabor lenses, which are under investigation at IAP [13]. To improve predictions for the observed steady-state and the behavior of these systems, it is important to improve the understanding of the involved processes as well as their interaction.

Particle-in-cell simulations can also provide valuable input for the design of accelerator components. Two applications for *bender* and *tralitrala* were described in this thesis: the Low-Energy Beam Transport section of the Frankfurt neutron source FRANZ with the novel E×B chopper system and the electron lens for the IOTA project at Fermi National Laboratory.

A wide range of possible parameter settings for the solenoids of the FRANZ LEBT were explored using *tralitrala* in [81], which is possible due to the short calculation times of the graphics card version. This makes it possible to easily find optimal settings of the beam line. Using distributions generated from these settings, the pulse shaping in the E×B chopper was studied in [11] using *bender*. The system was found to fulfill the requirements in regard to pulse length and beam quality.

For the IOTA electron lens, a coil layout satisfying the geometric requirements was found. Compared to the second electron lens used in the Tevatron, it features an increased angle of injection and an additional transfer solenoid. The distortion of the beam due to asymmetry in the field lines and due to particle drifts was studied.

The current that can be transported was found to be mainly limited by the influence of the longitudinal electric field resulting from the radial compression of the beam. The current limit also depends strongly on the beam pipe geometry. An expression for the limit was found and checked using simulations of a model system for a homogeneous distribution and for the McMillan distribution of interest for IOTA.

When the beam's electric field becomes non-negligible, particle motion shows a slow angular drift and a fast radial oscillation. Under this type of motion, a homogeneous beam distribution remains stable. However, for the McMillan distribution, the formation of rings of increased density was observed in two-dimensional PIC simulations. These were also found in calculations for the full electron lens in the form of spirals. Since the stability of the current density is important for the application of the electron lens, these results demand further investigation.

A. Derivation of the macroparticle equation of motion

Under the assumption of a phase-space density $f(t,x,v) = \sum_i N_i S(x - x_i(t))\,\delta(v - v_i(t))$, where the particle shape function $S(x)$ fulfills the requirements given in Section 3.1, the equation of motions for $x_i(t)$ and $v_i(t)$ can be found from the Vlasov equation

$$0 = \frac{\mathrm{d}f}{\mathrm{d}t} = \frac{\partial f}{\partial t} + v\frac{\partial f}{\partial x} + \frac{q}{m}E(x)\,\frac{\partial f}{\partial v}. \tag{A.1}$$

Due to the symmetry and the normalization of $S(x)$,

$$\int_{-\infty}^{\infty} xS(x - x_i(t))\,\mathrm{d}x = \int_{-\infty}^{\infty} (x + x_i(t))\,S(x)\,\mathrm{d}x = x_i(t)\,. \tag{A.2}$$

The following identity for the δ-distribution will be useful [66, p. 26]

$$\int_{-\infty}^{\infty} \left.\frac{\mathrm{d}\delta(x')}{\mathrm{d}x'}\right|_x f(x)\,\mathrm{d}x = -\left.\frac{\mathrm{d}f}{\mathrm{d}x}\right|_{x=0}. \tag{A.3}$$

For the first moment of the Vlasov equation in x,

$$\begin{aligned}
0 = \int x\frac{\mathrm{d}f}{\mathrm{d}t}\mathrm{d}x\mathrm{d}v &= \int x\left\{\frac{\partial f}{\partial t} + v\frac{\partial f}{\partial x} + \frac{q}{m}E(x)\,\frac{\partial f}{\partial v}\right\}\mathrm{d}x\mathrm{d}v \\
&= \sum_i N_i\Bigg\{ \underbrace{\int \delta(v - v_i(t))\,\mathrm{d}v}_{=1}\frac{\partial}{\partial t}\underbrace{\int xS(x - x_i(t))\,\mathrm{d}x}_{=x_i(t),\,(\mathrm{A}.2)} \\
&\quad + \underbrace{\int \frac{\partial\delta(v - v_i(t))}{\partial t}\mathrm{d}v}_{=\frac{\partial}{\partial t}\int\delta(v - v_i(t))\mathrm{d}v = 0}\int xS(x - x_i(t))\,\mathrm{d}x \\
&\quad + \underbrace{\int x\frac{\partial S(x - x_i(t))}{\partial x}\mathrm{d}x}_{=-1,\text{ partial integration}}\underbrace{\int v\delta(v - v_i(t))\,\mathrm{d}v}_{v_i(t)} \\
&\quad + \frac{q}{m}\int xE(x)\,S(x - x_i(t))\,\mathrm{d}x\underbrace{\int \frac{\partial\delta(v - v_i(t))}{\partial v}\mathrm{d}v}_{=0,(\mathrm{A}.3)}\Bigg\} \\
&= \sum_i N_i\left\{\frac{\partial x_i(t)}{\partial t} - v_i(t)\right\}.
\end{aligned}$$

For the first moment of the Vlasov equation in v,

$$
\begin{aligned}
0 = \int v \frac{\mathrm{d}f}{\mathrm{d}t} \mathrm{d}x \mathrm{d}v &= \int v \left\{ \frac{\partial f}{\partial t} + v \frac{\partial f}{\partial x} + \frac{q}{m} E(x) \, \frac{\partial f}{\partial v} \right\} \mathrm{d}x \mathrm{d}v \\
&= \sum_i N_i \Bigg\{ \underbrace{\int S(x - x_i(t)) \, \mathrm{d}x}_{=1} \frac{\partial}{\partial t} \int v \delta(v - v_i(t)) \, \mathrm{d}v \\
&\quad + \int v \delta(v - v_i(t)) \, \mathrm{d}v \, \underbrace{\frac{\partial}{\partial t} \int S(x - x_i(t)) \, \mathrm{d}x}_{=0} \\
&\quad + \underbrace{\int \frac{\partial S(x - x_i(t))}{\partial x} \mathrm{d}x}_{[S(x - x_i(t))]_{-\infty}^{\infty} = 0} \int v^2 \delta(v - v_i(t)) \, \mathrm{d}v \\
&\quad + \frac{q}{m} \int E(x) \, S(x - x_i(t)) \, \mathrm{d}x \, \underbrace{\int v \frac{\partial \delta(v - v_i(t))}{\partial v} \mathrm{d}v}_{=-1, \text{(A.3)}} \Bigg\} \\
&= \sum_i N_i \left\{ \frac{\partial v_i(t)}{\partial t} - \frac{q}{m} \int E(x) \, S(x - x_i(t)) \, \mathrm{d}x \right\}.
\end{aligned}
$$

Bibliography

[1] O. Buneman. "Dissipation of Currents in Ionized Media". In: *Phys. Rev.* 115 (1959), pp. 503–517. DOI: 10.1103/PhysRev.115.503.

[2] R. W. Hockney. "Computer Experiment of Anomalous Diffusion". In: *Physics of Fluids* 9.9 (1966), pp. 1826–1835. DOI: 10.1063/1.1761939.

[3] M. Lindroos, M. Eshraqi, and D. McGinnis. "The European Spallation Source". In: *Proceedings of PAC2013, Pasadena, USA, FRYAA2*. 2013.

[4] S. Cousineau. "A Fifteen Year Perspective on the Design and Performance of the SNS Accelerator". In: *Proceedings of HB2016, Malmö, Sweden, MOAM4P40*. 2016.

[5] S. Alzubaidi et al. "The Frankfurt Neutron Source FRANZ". In: *The European Physical Journal Plus* 131.5 (2016), pp. 1–13. DOI: 10.1140/epjp/i2016-16124-5.

[6] R. Garoby et al. "Plans for the Upgrade of the LHC Injectors". In: *Proceedings of IPAC2011, San Sebastián, Spain, WEPS017*. 2011.

[7] J. Struckmeier, J. Klabunde, and M. Reiser. "On the Stability and Emittance Growth of Different Particle Phase-Space Distributions in a Long Magnetic Quadrupole Channel". In: *Particle Accelerators* 22 (1984), pp. 47–65.

[8] A. J. T. Holmes. "Theoretical and Experimental Study of Space Charge in Intense Ion Beams". In: *Phys. Rev. A* 19 (1979), pp. 389–407. DOI: 10.1103/PhysRevA.19.389.

[9] A. BenIsmail et al. "Space Charge Compensation Studies of Hydrogen Ion Beams in a Drift Section". In: *Phys. Rev. Accelerators and Beams* 10 (2007), p. 070101. DOI: 10.1103/PhysRevSTAB.10.070101.

[10] V. Shiltsev and M. Chung. *Space-charge compensation experiments at IOTA ring*. FERMILAB-CONF-14-324-APC. arXiv:1502.01736 [physics.acc-ph]. Fermi National Accelerator Laboratory, 2015.

[11] C. Wiesner. "Chopping and Transport of High-Intensity Ion Beams". PhD thesis. Goethe Universität Frankfurt am Main, 2014.

[12] J. P. Freidberg. *Plasma Physics and Fusion Energy*. Cambridge University Press, 2007. ISBN: 9780511755705. DOI: 10.1017/CBO9780511755705.

[13] K. Schulte. "Studies on the Focusing Performance of a Gabor Lens Depending on Nonneutral Plasma Properties". PhD thesis. Goethe Universität Frankfurt am Main, 2013.

[14] D. Montgomery and D. Tidman. *Plasma Kinetic Theory*. McGraw-Hill, 1964. ISBN: 1114112887.

[15] F. J. Sacherer. "RMS Envelope Equations with Space Charge". In: *IEEE Transactions on Nuclear Science* 18.3 (1971), pp. 1105–1107. DOI: 10.1109/TNS.1971.4326293.

[16] M. Reiser. *Theory and Design of Charged Particle Beams*. John Wiley & Sons, 2008. ISBN: 9783527407415.

[17] J. Struckmeier. *Ion Beam Optics*. Lecture slides. https://web-docs.gsi.de/~struck/hp/vorlesung/Lectures1_8.pdf. Last accessed on 23.3.2016. 2005.

[18] J. Struckmeier. Private communication.

[19] F. Filbet and E. Sonnendrücker. "Comparison of Eulerian Vlasov Solvers". In: *Computer Physics Communications* 150.3 (2003), pp. 247–266. DOI: 10.1016/S0010-4655(02)00694-X.

[20] G. Lapenta. *Particle in Cell Method*. Last accessed on 5.4.2016. URL: https://perswww.kuleuven.be/~u0052182/weather/pic.pdf.

[21] R. W. Hockney and J. W. Eastwood. *Computer Simulation Using Particles*. Taylor & Francis, Inc., 1988. ISBN: 0-85274-392-0.

[22] L. Verlet. "Computer "Experiments" on Classical Fluids. I. Thermodynamical Properties of Lennard-Jones Molecules". In: *Phys. Rev.* 159 (1967), pp. 98–103. DOI: 10.1103/PhysRev.159.98.

[23] E. Hairer, C. Lubich, and G. Wanner. "Geometric Numerical Integration Illustrated by the Störmer-Verlet Method". In: *Acta Numerica* 12 (2003), pp. 399–450. DOI: 10.1017/S0962492902000144.

[24] W. H. Press et al. *Numerical Recipes: The Art of Scientific Computing*. 3rd edition. Cambridge University Press, 2007. ISBN: 0521880688.

[25] G. Shortley and R. Weller. "The Numerical Solution of Laplace's Equation". In: *Journal of Applied Physics* 9.5 (1938), pp. 334–348. DOI: 10.1063/1.1710426.

[26] U. Trottenberg, C. Oosterlee, and A. Schüller. *Multigrid*. Academic Press, 2001. ISBN: 978-0127010700.

[27] V. Simoncini and D. B. Szyld. "Recent Computational Developments in Krylov Subspace Methods for Linear Systems". In: *Numerical Linear Algebra with Applications* 14.1 (2007), pp. 1–59. DOI: 10.1002/nla.499.

[28] Y. Saad and M. H. Schultz. "GMRES: A Generalized Minimal Residual Algorithm for Solving Nonsymmetric Linear Systems". In: *SIAM Journal on Scientific and Statistical Computing* 7.3 (1986), pp. 856–869. DOI: 10.1137/0907058.

[29] S. Balay et al. *PETSc Users Manual*. http://www.mcs.anl.gov/petsc/petsc-current/docs/manual.pdf. 2014.

[30] R. Tiede. "Simulationswerkzeuge für die Berechnung hochintensiver Ionenbeschleuniger". PhD thesis. Goethe Universität Frankfurt am Main, 2009.

[31] J. W. Cooley and J. W. Tukey. "An Algorithm for the Machine Calculation of Complex Fourier Series". In: *Mathematics of Computation* 19.90 (1965), pp. 297–301. DOI: 10.2307/2003354.

[32] *FFTW - Fastest Fourier Transform in the West 3.4.4*. http://www.fftw.org/. 2015.

[33] C. K. Birdsall and A. B. Langdon. *Plasma Physics via Computer Simulation*. CRC Press, 1991. ISBN: 978-0750310253.

[34] J. P. Verboncoeur. "Symmetric Spline Weighting for Charge and Current Density in Particle Simulation". In: *J. Comput. Phys.* 174.1 (2001), pp. 421–427. DOI: 10.1006/jcph.2001.6923.

[35] *Armadillo - C++ Linear Algebra Library*. http://arma.sourceforge.net/. 2015.

[36] *Boost.MPI*. http://www.boost.org/doc/libs/1_57_0/doc/html/mpi.html. 2015.

[37] H. Wiedemann. *Particle Accelerator Physics*. Springer, 2007. ISBN: 978-3540490432.

[38] E. Hairer, C. Lubich, and G. Wanner. *Geometric Numerical Integration*. Springer, 2000. ISBN: 3540306633.

[39] R. C. Davidson. *Physics of Nonneutral Plasmas*. 2nd edition. World Scientific Publishing Company, 2001. ISBN: 978-1860943034.

[40] R. G. Lefrancois et al. "Numerical Investigation of Three-Dimensional Single-Species Plasma Equilibria on Magnetic Surfaces". In: *Physics of Plasmas* 12.7, 072105 (2005). DOI: 10.1063/1.1928248.

[41] E. Anderson et al. *LAPACK Users' Guide*. 3rd edition. Society for Industrial and Applied Mathematics, 1999. ISBN: 0-89871-447-8.

[42] T. A. Davis. "Algorithm 832: UMFPACK v4.3 – An Unsymmetric-Pattern Multifrontal Method". In: *ACM Trans. Math. Softw.* 30.2 (2004), pp. 196–199. DOI: 10.1145/992200.992206.

[43] F. Kesting and G. Franchetti. "Propagation of numerical noise in particle-in-cell tracking". In: *Phys. Rev. ST Accel. Beams* 18 (2015), p. 114201. DOI: 10.1103/PhysRevSTAB.18.114201.

[44] H. Reichau. "Fundamentals for Routined Utilization of Tomography in Beam Diagnostics". PhD thesis. Goethe Universität Frankfurt am Main, 2012.

[45] R. Dölling. "Raumladungskompensation driftender intensiver Strahlen niederenergetischer Ionen und Techniken zu ihrer Vermessung". PhD thesis. Johann Wolfgang Goethe-Universität Frankfurt am Main, 1994.

[46] P. Groß. "Untersuchungen zum Emittanzwachstum intensiver Ionenstrahlen bei teilweiser Kompensation der Raumladung". PhD thesis. Johann Wolfgang Goethe-Universität Frankfurt am Main, 2000.

[47] R. Salemme et al. "Design Progress of the MYRRHA Low Energy Beam Line". In: *Proceedings of LINAC14, Geneva, Switzerland, MOPP137*. 2014.

[48] M. E. Rudd et al. "Electron Production in Proton Collisions With Atoms and Molecules: Energy Distributions". In: *Reviews of Modern Physics* 64.2 (1992), p. 441. DOI: 10.1103/RevModPhys.64.441.

[49] M. E. Rudd et al. “Electron Production in Proton Collisions With Atoms and Molecules: Total Cross Sections”. In: *Reviews of Modern Physics* 57.4 (1985), pp. 965–994. DOI: 10.1103/RevModPhys.57.965.

[50] M. Rudd, L. Toburen, and N. Stolterfoht. “Differential Cross Sections for Ejection of Electrons from Argon by Protons”. In: *Atomic Data and Nuclear Data Tables* 23.5 (1979), pp. 405–442. DOI: 10.1016/0092-640X(79)90026-3.

[51] M. B. Shah and H. B. Gilbody. “Ionisation of H_2 by Fast Protons and Multiply Charged Ions of He, Li, C, N and O”. In: *Journal of Physics B: Atomic and Molecular Physics* 15.19 (1982), p. 3441. DOI: 10.1088/0022-3700/15/19/013.

[52] Y.-K. Kim and M. E. Rudd. “Binary-Encounter-Dipole Model for Electron-Impact Ionization”. In: *Phys. Rev. A* 50 (1994), pp. 3954–3967. DOI: 10.1103/PhysRevA.50.3954.

[53] D. Rapp and P. Englander-Golden. “Total Cross Sections for Ionization and Attachment in Gases by Electron Impact. I. Positive Ionization”. In: *The Journal of Chemical Physics* 43.5 (1965), pp. 1464–1479. DOI: 10.1063/1.1696957.

[54] R. Rejoub, B. G. Lindsay, and R. F. Stebbings. “Determination of the Absolute Partial and Total Cross Sections for Electron-Impact Ionization of the Rare Gases”. In: *Phys. Rev. A* 65 (2002), p. 042713. DOI: 10.1103/PhysRevA.65.042713.

[55] C. B. Opal, E. C. Beaty, and W. K. Peterson. “Tables of Secondary-Electron-Production Cross Sections”. In: *Atomic Data and Nuclear Data Tables* 4 (1972), pp. 209–253. DOI: 10.1016/S0092-640X(72)80004-4.

[56] D. Hasselkamp et al. “Ion Induced Electron Emission from Metal Surfaces”. In: *Nuclear Instruments and Methods* 180.2 (1981), pp. 349–356. DOI: 10.1016/0029-554X(81)90076-8.

[57] M. A. Furman and M. T. F. Pivi. “Probabilistic Model for the Simulation of Secondary Electron Emission”. In: *Phys. Rev. Accelerators and Beams* 5.12 (2002). DOI: 10.1103/PhysRevSTAB.5.124404.

[58] A. Phelps and Z. L. Petrovic. “Cold-Cathode Discharges and Breakdown in Argon: Surface and Gas Phase Production of Secondary Electrons”. In: *Plasma Sources Science and Technology* 8.3 (1999). DOI: 10.1088/0963-0252/8/3/201.

[59] V. Vahedi and M. Surendra. “A Monte Carlo Collision Model for the Particle-In-Cell Method: Applications to Argon and Oxygen Discharges”. In: *Computer Physics Communications* 87.1 (1995), pp. 179–198. DOI: 10.1016/0010-4655(94)00171-W.

[60] M. W. Gealy et al. “Energy and Angular Distributions of Electrons from Ion Impact on Atomic and Molecular Hydrogen. I. 20-114-keV H^++H_2”. In: *Phys. Rev. A* 51 (1995), pp. 2247–2255. DOI: 10.1103/PhysRevA.51.2247.

[61] R. D. DuBois and M. E. Rudd. “Absolute Doubly Differential Cross Sections for Ejection of Secondary Electrons from Gases by Electron Impact. II. 100-500-eV Electrons on Neon, Argon, Molecular Hydrogen, and Molecular Nitrogen”. In: *Phys. Rev. A* 17 (1978), pp. 843–848. DOI: 10.1103/PhysRevA.17.843.

[62] *Center of Scientific Computing*. 2014. URL: https://csc.uni-frankfurt.de/.

[63] A. Einstein. "Über die von der molekularkinetischen Theorie der Wärme geforderte Bewegung von in ruhenden Flüssigkeiten suspendierten Teilchen". In: *Ann. Phys. 322* (1905), pp. 549–560. DOI: 10.1002/andp.19053220806.

[64] T. Takizuka and H. Abe. "A binary collision model for plasma simulation with a particle code". In: *Journal of Computational Physics* 25.3 (1977), pp. 205–219. DOI: 10.1016/0021-9991(77)90099-7.

[65] T. Weis. "Untersuchungen zum Verhalten hochperveanter Ionenstrahlen bei Raumladungskompensation". Habilitation. Johann Wolfgang Goethe-Universität Frankfurt am Main, 1991.

[66] J. D. Jackson. *Classical Electrodynamics*. 3rd edition. John Wiley & Sons. ISBN: 978-0471309321.

[67] V. D. Shiltsev. *Electron Lenses for Super-Colliders*. 1st edition. Springer, 2016. ISBN: 978-1493933150.

[68] V. Shiltsev et al. "Tevatron Electron Lenses: Design and Operation". In: *Phys. Rev. Accelerators and Beams* 11 (2008), p. 103501. DOI: 10.1103/PhysRevSTAB.11.103501.

[69] G. Stancari et al. "Collimation with Hollow Electron Beams". In: *Phys. Rev. Lett.* 107 (2011), p. 084802. DOI: 10.1103/PhysRevLett.107.084802.

[70] X.-L. Zhang et al. "Generation and Diagnostics of Uncaptured Beam in the Fermilab Tevatron and Its Control by Electron Lenses". In: *Phys. Rev. Accelerators and Beams* 11 (2008), p. 051002. DOI: 10.1103/PhysRevSTAB.11.051002.

[71] W. Fischer et al. "Operational Head-on Beam-Beam Compensation with Electron Lenses in the Relativistic Heavy Ion Collider". In: *Phys. Rev. Lett.* 115 (2015), p. 264801. DOI: 10.1103/PhysRevLett.115.264801.

[72] V. Shiltsev et al. "Experimental Studies of Compensation of Beam-Beam Effects with Tevatron Electron Lenses". In: *New Journal of Physics* 10.4 (2008). DOI: 10.1088/1367-2630/10/4/043042.

[73] G. Stancari et al. *Conceptual Design of Hollow Electron Lenses for Beam Halo Control in the Large Hadron Collider*. FERMILAB-TM-2572-APC. arXiv:1405.2033 [physics.acc-ph]. Fermi National Accelerator Laboratory, 2014.

[74] D. Noll and G. Stancari. *Field Calculations, Single-Particle Tracking, and Beam Dynamics with Space Charge in the Electron Lens for the Fermilab Integrable Optics Test Accelerator*. FERMILAB-TM-2598-AD-APC. arXiv:1511.04507 [physics.acc-ph]. Fermi National Accelerator Laboratory, 2014.

[75] V. Danilov and S. Nagaitsev. "Nonlinear Accelerator Lattices with One and Two Analytic Invariants". In: *Phys. Rev. Accelerators and Beams* 13 (2010). DOI: 10.1103/PhysRevSTAB.13.084002.

[76] G. Stancari. "Applications of Electron Lenses: Scraping of High-Power Beams, Beam-Beam Compensation, and Nonlinear Optics". In: *Proceedings of the 16th Advanced Accelerator Concepts Workshop (AAC 2014) San Jose, California, US*. arXiv:1409.3615 [physics.acc-ph]. 2014.

[77] V. Danilov and E. A. Perevedentsev. "Two Examples of Integrable Systems with Round Colliding Beams". In: *Proceedings of the PAC97, Vancouver, Canada*. 1997, pp. 1759–1761.

[78] J. T. Tanabe. *Iron Dominated Magnets – Design, Fabrication, Assembly and Measurements*. World Scientific Publishing, 2005. ISBN: 981256327-X.

[79] *Accelerator Simulations Cluster Wilson*. 2014. URL: `http://tev.fnal.gov/`.

[80] G. Stancari. *Calculation of the Transverse Kicks Generated by the Bends of a Hollow Electron Lens*. FERMILAB-FN-0972-APC. arXiv:1403.6370 [physics.acc-ph]. Fermi National Accelerator Laboratory, 2014.

[81] P. Schneider. "Anpassung von Ionenstrahlen an die Akzeptanz eines RFQ". MA thesis. Goethe Universität Frankfurt am Main, 2014.

[82] L. P. Chau et al. "Bunch Compressor for Intense Proton Beams". In: *Proceedings of LINAC10, Tsukuba, Japan, TH203*. 2010.

[83] *CST – Computer Simulation Technology*. `https://www.cst.com/`.

[84] F. Hinterberger. *Physik der Teilchenbeschleuniger und Ionenoptik*. Zweite Ausgabe. Springer, 2008. ISBN: 978-3540612384.